Civil Engineering and Applied Solutions

Research Article

journal homepage: ceas.journals.umz.ac.ir

CEAS Civil Engineering and Applied Solutions

Experimental Study of Circular Concrete Column Confined with Hybrid FRP-Steel Tube Under Axial Load

Abolghasem Salari [a], Morteza Naghipour [a*]

[a] *Faculty of Civil Engineering, Babol Noshirvani University of Technology, Babol, Iran*

ARTICLE INFO

Keywords:
Concrete column
Confinement
Stress-strain curve
Steel
FRP
Steel-FRP composite tube

Article history:
Received 8 May 2025
Accepted 13 May 2025
Available online 01 July 2025

ABSTRACT

This study investigates the axial compressive behavior of circular concrete columns confined using three methods: steel tube confinement, FRP confinement, and hybrid FRP–steel tube confinement. Specimens were designed with similar confinement ratios to allow fair evaluation of their mechanical performance. Experimental results showed that while the type of confinement had little effect on initial stiffness, it significantly influenced the post-peak behavior. Steel confinement offered the highest strength and ductility, while FRP confinement increased ultimate strain but failed abruptly due to brittle rupture. The hybrid system exhibited a staged failure mechanism with improved confinement efficiency and a balance between strength and ductility. Stress–strain curves, volumetric strain trends, and tangent Poisson's ratio analyses highlighted the superior performance of hybrid systems. The findings suggest that hybrid FRP–steel confinement is a promising solution for enhancing both strength and deformation capacity in reinforced concrete columns, especially in seismic or high-performance structural applications.

1. Introduction

Concrete is one of the most widely used materials in structural engineering due to its high compressive strength, availability, and cost-effectiveness. However, its brittle nature and low tensile capacity make it vulnerable to axial loads, especially in seismic zones or heavily loaded structures. To overcome these limitations, various confinement techniques have been developed to enhance the mechanical performance of concrete elements, particularly columns. When an axial compressive force is applied to a concrete column, lateral expansion occurs due to the Poisson effect. Introducing a confining material restricts this expansion and induces lateral pressure on the core, transforming the stress state of the concrete from uniaxial to triaxial. As a result, confined concrete exhibits improved energy absorption and deformation capacity.

One of the earliest and most influential models in this field was proposed by Richartet al. [1] through experimental investigations on concrete cylinders under combined compressive stresses. Their study demonstrated that applying lateral confining pressure significantly increases the axial compressive strength of concrete. Building on this, Newman and Newman [2] proposed a more realistic basis for design, especially in situations involving moderate to high levels of active confinement. A significant advancement came with the work of Mander et al. [3], who proposed a widely used stress–strain model for steel-confined concrete that effectively captures strength and ductility improvements, especially in seismic applications. Han et al. [4] highlighted the significant influence of geometry and loading conditions on the confinement efficiency of steel tube-confined stub columns under localized axial loads. Liu et al. [5] confirmed that steel tubes provide effective lateral confinement, significantly enhancing the strength and ductility of CTRC columns. Qi et al. [6] emphasized the influence of geometry, showing that thicker tube walls and shorter column heights improve confinement by reducing buckling and increasing lateral restraint. Lin et al. [7] found that in circular concrete-filled steel tube columns, confinement effectiveness and compressive strength depend on the stress path at low confinement levels, but become path-independent as confinement increases. Xiamuxi et al. [8] investigated the effect of steel tube wall thickness on the axial

* Corresponding author.
E-mail addresses: m-naghi@nit.ac.ir (M. Naghipour).

https://doi.org/10.22080/ceas.2025.29200.1011
ISSN: 3092-7749/© 2025 The Author(s). Published by University of Mazandaran.
This article is an open access article distributed under the terms and conditions of the Creative Commons Attribution (CC-BY) license (https://creativecommons.org/licenses/by/4.0/deed.en)
How to cite this article: Salari ,A., Naghipour, M. Experimental study of circular concrete column confined with hybrid FRP-steel tube under axial load. Civil Engineering and Applied Solutions. 2025; 1(2): 1–13. doi:10.22080/ceas.2025.29200.1011.

compression behavior of square columns filled with reinforced and recycled aggregate concrete. They found that increasing wall thickness enhances confinement, improves load-bearing capacity, and delays failure, underscoring the importance of steel tube confinement in structural performance. Cao et al. [9] showed that steel tube confinement enhances concrete durability by reducing sulfate penetration and cracking.

While steel confinement offers reliable confinement capacity, FRP has emerged as a promising alternative. Kurt [10] found that PVC tubes offered minimal confinement due to low stiffness, while Harmon [11] showed that FRP tubes (CFRP and GFRP) provided effective confinement, with bilinear stress–strain behavior influenced by fiber volume ratio. Lam et al. [12] studied the axial behavior of FRP-confined concrete under cyclic and monotonic compression. Their results showed that cyclic loading had minimal effect on the stress–strain curve envelope but caused a slight increase in ultimate axial strain. Berthet et al. [13] developed a model for FRP-confined concrete, showing that confinement efficiency depends on hoop behavior, concrete strength, and stiffness. Li et al. [14] found that fiber orientation significantly affects confinement efficiency. Hoop-aligned fibers (90°) provided the best strength and ductility, while axial (0°) and angled (45°) orientations led to earlier or mixed-mode failures, highlighting the importance of hoop-direction reinforcement. Toutanji et al. [15] showed that the axial strength of FRP-confined concrete columns increases with FRP jacket thickness and tensile strength. Elsanadedy et al. [16] investigated size effects in FRP-confined concrete and found that larger column diameters reduced compressive strength in unconfined concrete, though the effect was less pronounced in confined specimens. Yang et al. [17] developed an ultrasonic method to monitor damage in FRP-confined concrete, effectively detecting stiffness loss and rupture zones. Zheng et al. [18] identified the Wei and Wu model as the most accurate for predicting ultimate axial strain in FRP-confined non-circular columns.

While FRP confinement can significantly enhance axial capacity, its brittle failure mode often leads to sudden loss of confinement and abrupt column collapse. In contrast, steel tube confinement provides more gradual failure due to its elastic–plastic behavior and sustained lateral pressure after yielding. However, steel systems are vulnerable to issues such as corrosion and increased weight, limiting their long-term durability. Xiao et al. [19] demonstrated that combining steel tubes with external FRP layers improves strength, ductility, and seismic performance in concrete-filled steel tubular (CFT) column systems, though a gap between layers can delay FRP activation—underscoring the need for careful interface detailing. Feng et al. [20] showed that combining steel tubes with FRP-confined cores improves confinement, ductility, and residual strength in composite columns. Ma et al. [21] used the XGBoost algorithm to accurately predict the axial strength of CFRP-confined CFT columns. Their model outperformed other machine learning methods, achieving high accuracy ($R^2 = 0.9850$) after optimization. Liu et al. [22] proposed a machine learning-based framework using synthetic data to predict and optimize the axial strength of FRP-reinforced CFT columns. The model, combined with genetic algorithm optimization, outperformed traditional design methods and supports the efficient design of FRP-confined CFT systems.

To overcome the limitations of single-material confinement systems, this study investigates a hybrid FRP–steel tube confinement approach combining an inner steel tube with an outer FRP wrap. The experimental program included four groups of cylindrical specimens: unconfined concrete, steel tube-confined, FRP-confined, and hybrid FRP–steel tube-confined. All specimens were cast from a single concrete batch and designed with comparable confinement ratios to enable fair comparisons. Axial compression tests were conducted using a 200-ton capacity machine, with strain gauges and LVDTs installed to measure lateral and axial deformation. The hybrid system was designed to exploit the ductility of steel and the strength and corrosion resistance of FRP. This configuration aims to enhance compressive strength, ductility, and post-peak behavior while delaying brittle failure. The results are compared to assess the hybrid system's efficiency relative to steel- and FRP-only confinement

2. Experimental phase

2.1. Specimens

Four types of specimens were prepared: 1. Unconfined concrete cylinders (Group R-control samples), 2. Steel tube-confined cylinders (Group S), 3. FRP-confined cylinders (Group F), and 4-Hybrid steel + FRP-confined cylinders (Group SF). Each group consisted of multiple identical specimens; all cast from a single concrete batch to ensure uniformity. Fig. 1 shows the geometric properties of specimens. Each cylinder had a core diameter of 55 mm and a height of 140–150 mm, producing height-to-diameter ratios from 2.3 to 2.7. This ensured minimal buckling and friction effects (Table 1).

2.2. Confinement thickness

The configurations were selected to ensure that the confinement Ratio C_r values across groups are similar, enabling fair comparisons of their effectiveness. The confinement ratio is a dimensionless parameter that quantifies the level of lateral confinement pressure applied to the concrete core, normalized by the concrete's unconfined strength. It is defined as:

$$C_r = \frac{f_l}{f_c'} \tag{1}$$

where f_l is lateral confining pressure (from steel, FRP, or hybrid system), and f_c' is the unconfined compressive strength of concrete. The lateral confining pressure f_l depends on the thickness and stiffness of the confining material. This pressure can be estimated using hoop equilibrium theory. The lateral confining pressure f_l for steel tubes, FRP jackets, and hybrid confinement (steel + FRP) are defined in Eqs. 7 to 9, respectively:

$$f_l = \frac{2t_s f_{ys}}{D} \quad (2)$$

$$f_l = \frac{2t_f f_{uf}}{D} \quad (3)$$

$$f_l = \frac{2t_s f_{ys} + 2t_f f_{uf}}{D} \quad (4)$$

where t_s and f_{ys} are the thickness and yield strength of the steel tube, t_f and f_{uf} are the thickness and ultimate tensile strength of the FRP, and D is the internal diameter of the concrete core. The steel tube thickness was 2.0 mm for specimens in Group S, while Group F specimens were wrapped with two layers of FRP, totaling 0.32 mm in thickness. For the hybrid Group SF, specimens were confined using a 0.9 mm thick steel tube combined with a 0.16 mm thick single-layer FRP wrap (Fig. 2).

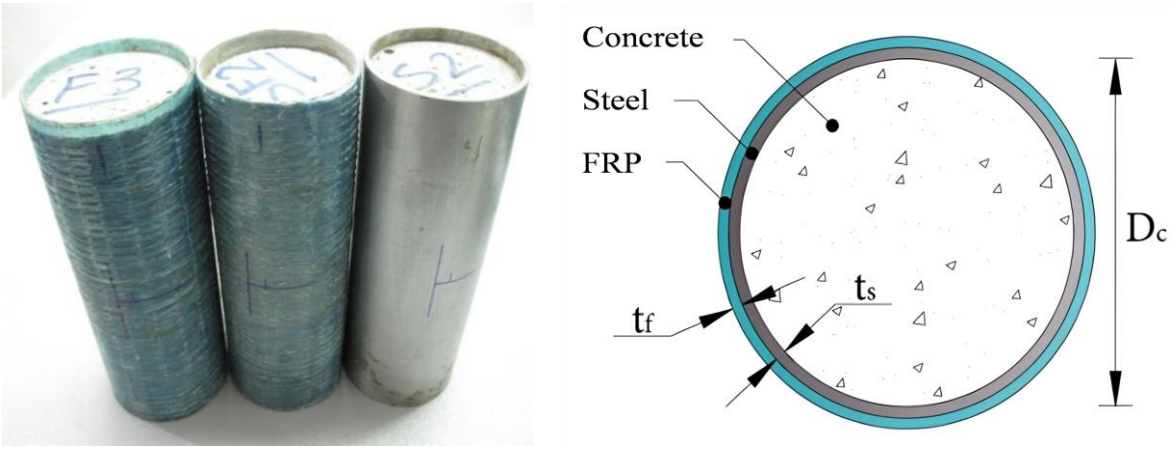

(a) (b)

Fig. 1. (a) Confined specimens, top view of a concrete column confined with a hybrid FRP–steel tube.

Table 1. Geometric Properties of Specimens.

Group	Core Diameter (mm)	Height (mm)	H/D Ratio	No. of Specimens
R (Control Samples)	55	150	2.7	6
S (Confined Specimens)	55	140	2.5	5
F (Confined Specimens)	60	140	2.3	5
SF (Confined Specimens)	55	140	2.5	5

Fig. 2. Hybrid steel–FRP tube before concrete casting.

2.3. Specimen preparation and curing conditions

Two days after casting, the control samples (Group R), which were not confined (Fig. 3(a)), were de-molded and placed in a water curing tank. These specimens remained fully submerged in water until the day of testing. Confined specimens, encased in steel tubes (Group S), FRP jackets (Group F), and hybrid steel–FRP tubes (Group SF), were not immersed in water after demolding. Because the lateral surfaces were covered with impermeable jackets and the top and bottom surfaces were sealed using steel end

plates, the risk of moisture loss was minimized (Fig. 3(b)). These specimens were stored at room temperature under sealed conditions until the day of testing.

Fig. 3. (a) Control specimens (Group R), (b) Confined specimens with steel tubes (Group S), FRP jackets (Group F), and hybrid steel–FRP tubes (Group SF).

To compare the unconfined compressive strength of the same concrete used in the confined specimens, on the test day, two specimens from each confined group were carefully cut and stripped of their steel or FRP jackets using a precision saw. The concrete core was then extracted and tested as a reference. These samples were labeled as unconfined specimens from jacketed groups (sometimes referred to as "stripped controls") and were used to directly measure the baseline strength of the confined groups' concrete without external confinement (Fig. 4).

Fig. 4. Concrete cores extracted from confined specimens.

2.4. Material properties

The materials used in this study included concrete, steel tubes, and fiber-reinforced polymer (FRP) jackets. The concrete was designed according to ACI 211 standards with a target compressive strength of 35 MPa. The steel used for confinement was tested and found to have a modulus of elasticity of 210 GPa and yield strength of 340 MPa. It also exhibited strain hardening, with an ultimate tensile strength of approximately 480 MPa. For external confinement, GFRP (Glass Fiber Reinforced Polymer) sheets were used. According to the manufacturer, the GFRP had a modulus of elasticity of 76 GPa and an ultimate tensile strength of 2300 MPa. The FRP jackets were manufactured using the wet lay-up process, and fibers were oriented in the hoop direction to provide effective lateral confinement.

2.5. Test setup and instrumentational

All specimens were tested using a 200-ton capacity ELE compression testing machine. For the control (unconfined) specimens, two MDF plates were placed at the top and bottom ends of the cylinders to reduce stress concentration and prevent premature cracking. The average compressive strength of the unconfined specimens was recorded and used as the reference strength f_c'. For the confined specimens (not acting as structural columns), the axial load was applied directly to the concrete core rather than through the confining shell. To ensure this, a steel rod with a diameter smaller than the inner diameter of the confining tube was used to apply load directly to the core. This ensured that no contact occurred between the loading platen and the inner surface of the confinement tube, preventing friction effects that could influence test results. The loading and instrumentation setup is shown in

Fig. 5.

Fig. 5. A steel-confined specimen with instrumentation for loading and deformation measurement.

To measure lateral strain, two horizontal strain gauges were symmetrically mounted on opposite sides of each specimen at mid-height on the external surface (as shown in Fig. 6(a)). The average reading from these gauges was taken as the lateral strain. Additionally, to evaluate the stress distribution and possible circumferential cracking in the tube, a vertical strain gauge was added to one of the horizontal gauges. To determine the axial strain of the concrete core, two LVDTs were placed symmetrically on opposite sides of each specimen. The average displacement recorded by these LVDTs was taken as the vertical deformation (see Fig. 6(b) for the test setup).

(a)

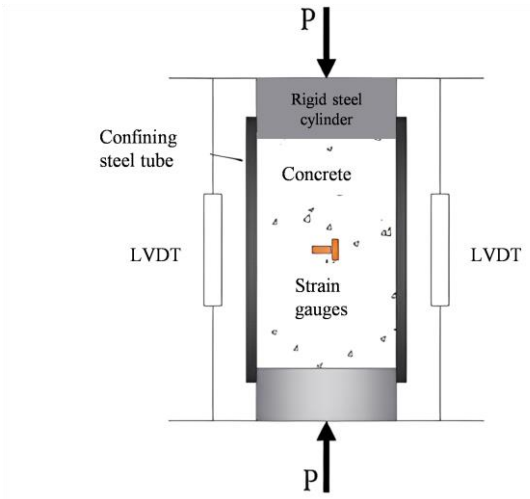

(b)

Fig. 6. (a) Strain gauge arrangement on confined specimens, (b) Loading setup for confined specimens.

3. Results and discussion

3.1. Failure mode

3.1.1.Unconfined concrete specimens (Group R)

Fig. 7 shows the failure pattern of control specimens cured in water. The observed failures correspond primarily to Type B and Type C modes in ASTMC39. These refer to conical shear failure and shear with splitting, respectively. The cracks observed in the specimens were relatively deep, and in some cases, the failure was accompanied by a distinctly loud sound, indicating brittle fracture through the aggregate particles. This confirms that the failure was not limited to the cement paste but involved the fracture of coarse aggregates, typical of well-cured, high-strength concrete.

Fig. 7. Failure patterns of reference concrete specimens.

Further, two specimens from each confined group were tested after removing their steel or FRP confinement on the day of testing. As shown in Fig. 8, the resulting failure was characterized by very fine surface cracks with no significant crack depth or audible fracture sound, indicating low-energy brittle failure. The cracks did not propagate through the coarse aggregates, suggesting that the failure occurred primarily along the weakened cement paste–aggregate interface. This brittle response confirms the limited integrity of the exposed concrete cores, likely due to micro-damage during confinement removal and the absence of external restraint.

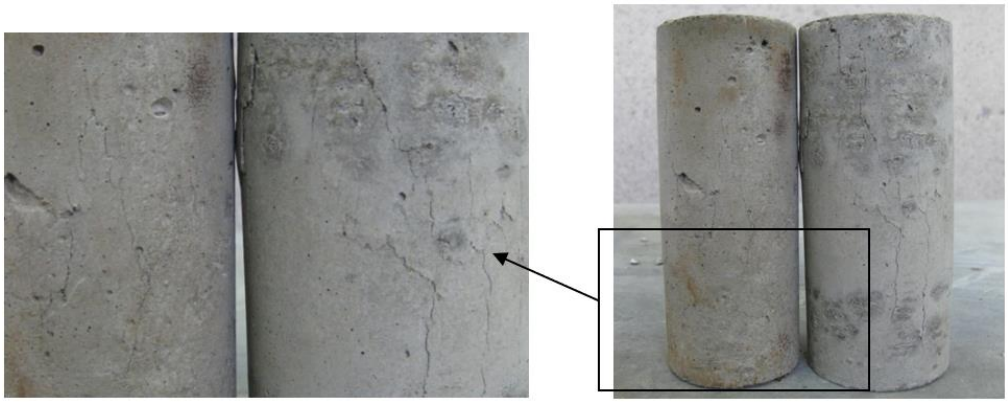

Fig. 8. Failure mode of unconfined concrete cores extracted from confined specimens on the test day.

3.1.2.Confined concrete specimens (Group F)

This section discusses the failure modes of various types of confinement, including FRP, steel, and hybrid FRP–steel systems. FRP-confined specimens (Group F) exhibited failure through rupture of the hoop fibers in the circumferential direction. This was triggered by significant lateral dilation of the core concrete, which generated high tensile stresses in the FRP jacket (Fig. 9(a)). The failure was typically sudden and brittle, characteristic of the limited ductility of FRP materials. Steel-confined specimens (Group S) failed due to radial bulging at mid-height without signs of local buckling. The steel tubes yielded under high circumferential tensile stress, with the most pronounced swelling occurring at the center of the specimen. This was attributed to the peak axial stress developing at mid-height and the friction between the specimen ends and the loading platens, which restrained lateral expansion near the ends (Fig. 9(b)). Hybrid FRP–steel confined specimens (Group SF) showed a sequential failure process. Initially, the FRP jacket ruptured in the hoop direction as a result of internal concrete expansion, reducing the confinement capacity. With continued axial loading, local buckling and eventual rupture of the steel tube followed, leading to a complete structural failure (Fig. 9(c)). This two-stage failure highlights the interaction and transitional behavior between brittle FRP and ductile steel confinement.

Table 1 summarizes the average compressive strength and ultimate axial strain for each group. Group F showed a ~2.3× strength increase and 10× higher strain than R'. Group S showed the highest strength, but Group SF achieved a better balance between strength and ductility. f_c' is unconfined compressive strength and f_{cc}' is confined compressive strength.

3.2. Stress-strain behavior

3.2.1.Axial stress–strain

The axial stress–strain curves of the specimens confined with steel tube (S), FRP (F), and hybrid FRP-steel tube (SF) demonstrated distinct behavioral differences, as shown in Fig. 10. Up to approximately the unconfined compressive strength ($f_c' \approx 24.7\ MPa$), all specimens exhibited a nearly identical response, indicating that lateral confinement does not activate significantly in the initial linear region of loading. Beyond this point, concrete begins to crack internally, generating lateral expansion that activates the confinement mechanism in each group. The stress–strain response then diverges based on the confinement system. The FRP-confined group (F) exhibited the steepest post-peak drop in stiffness, indicating more brittle failure, while the steel-confined

group (S) showed the most ductile behavior with a long post-peak plateau. The hybrid group (SF) showed intermediate behavior, benefiting from the stiffness of FRP and the ductility of steel.

(a) (b) (c)

Fig. 9. (a) Failure mode of an FRP-confined concrete specimen, (b) Failure mode of a steel tube-confined concrete specimen, and (c) Failure mode of a hybrid FRP–steel tube confined concrete specimen.

Table 1. Average Compressive Strength and Ultimate Axial Strain.

Group	f'_{cc} (MPa)	f'_{cc} / f'_c	Ultimate Axial Strain
R'	27.4	–	–
R	35.2	1.28	–
F	79.5	2.26	0.033
S	95.2	2.79	0.048
SF	89.7	2.61	0.026

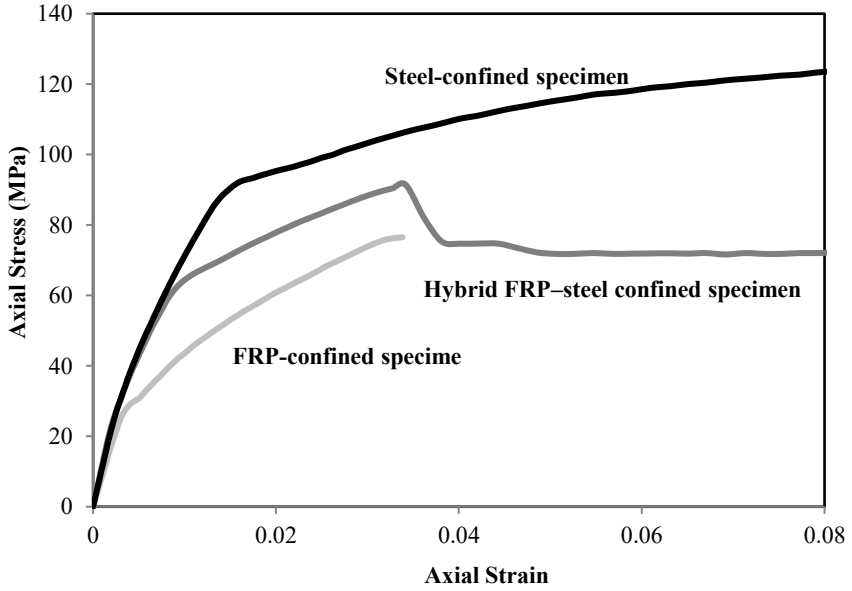

Fig. 10. Axial stress-strain curves of confined concrete specimens.

To further analyze this behavior, the lateral confining pressure f_l from elastic confinement can be calculated using the hoop stress relation:

$$f_\theta = E\varepsilon_\theta \quad \rightarrow \quad f_l = \frac{2tE\varepsilon_\theta}{D} = \left(\frac{2tE}{D}\right).\varepsilon_\theta \tag{5}$$

where E is the modulus of the confining material, ε_θ is the lateral strain, t is the thickness of the confining element, and D is the diameter of the concrete core. From Eq. 10, the equivalent lateral stiffness $\left(\frac{2tE}{D}\right)$ was calculated for each group to evaluate their contribution to lateral pressure resistance. For the FRP-confined group (F), the lateral stiffness was estimated at 0.8 GPa; for the steel-confined group (S), it was 7.2 GPa; and for the hybrid FRP–steel group (SF), the combined stiffness reached 15.1 GPa. These values confirm that the hybrid system offers the highest confinement effectiveness due to the parallel contribution of both FRP and

steel, while the FRP-alone system provides the lowest confinement stiffness, which explains its relatively more brittle behavior after peak stress.

To evaluate the initial stiffness of the confined specimens, the initial tangent modulus was calculated from the linear portion of the stress–strain curves. As illustrated in Fig. 11, the FRP-confined group (F) exhibited the lowest average elastic modulus, measured at 9699 MPa. In contrast, the steel-confined group (S) and hybrid group (SF) demonstrated higher initial stiffness values of 11,797 MPa and 11,655 MPa, respectively. This trend reflects the mechanical nature of the confining materials: while FRP primarily provides hoop confinement and does not significantly resist axial deformation, steel and hybrid tubes offer both axial and lateral stiffness. The slight difference between the S and SF groups suggests that the axial stiffness of the hybrid system is predominantly governed by the steel component. These findings confirm that FRP alone contributes less to axial stiffness, particularly during the early elastic stage, whereas steel and hybrid tubes enhance both the initial stiffness and the overall load-carrying behavior from the onset of loading.

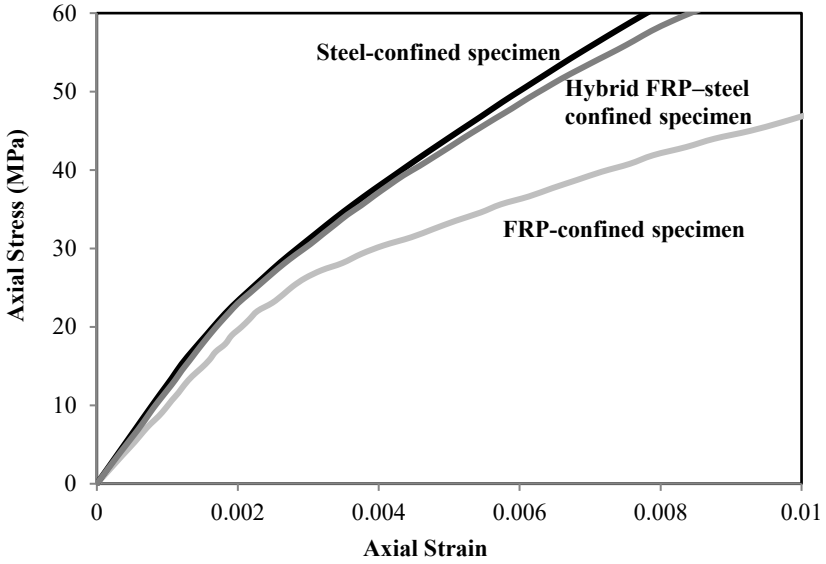

Fig. 11. Initial portion of axial stress-strain curves for confined concrete specimens.

3.2.2.FRP confinement

The stress–strain response of FRP-confined concrete specimens (Fig. 12) shows a distinct bilinear trend. In the initial phase, the behavior closely follows that of unconfined concrete, with the FRP jacket exerting minimal confinement. As the axial load increases, lateral expansion activates the FRP, which then begins to provide lateral pressure in a linear manner up to the rupture point. The slope of the second branch is primarily influenced by the hoop stiffness of the FRP and is only slightly affected by the compressive strength of the concrete. Increasing the number of FRP layers results in a higher confinement stiffness, thereby increasing the slope of the post-peak branch and raising the peak strength. Upon rupture of the FRP, the lateral confinement abruptly ceases, and since no further restraint is applied to resist lateral dilation, the core concrete fails suddenly. The failure is brittle and occurs at the moment of jacket rupture, highlighting the absence of post-rupture confinement.

3.2.3.Steel confinement

As shown in Fig. 13, steel-confined specimens behave differently. After the axial stress reaches the unconfined concrete strength, lateral expansion initiates hoop tension in the steel tube. Because of the high confinement stiffness of steel, there is only a minor drop in the curve's slope after the peak, and no significant post-peak softening is observed. The steel continues to apply nearly constant lateral pressure even after yielding, provided the steel demonstrates ideal elastic–plastic behavior. If the steel exhibits strain hardening, the lateral pressure increases post-yield, slightly raising the axial load capacity further. However, if the steel has low post-yield stiffness, the confinement effect declines more rapidly. In this study, the steel used showed noticeable strain hardening, contributing to improved ductility and a more stable post-peak response. The axial stress–strain curve remains smooth and transitions gradually into a softening branch.

3.2.4.Hybrid FRP–steel confinement

The hybrid specimens (Fig. 14) display a combined response. Initially, the confinement stiffness is high due to the contribution of both steel and FRP. At approximately 65 MPa axial stress, a sudden drop in slope occurs, which corresponds to the yielding of the steel tube. Although the steel's confinement contribution reduces after yielding, the FRP—still intact—continues to provide confinement and maintains the residual strength of the system. Once the FRP eventually ruptures, the lateral pressure from the hybrid shell decreases sharply. However, due to the ductility and strain capacity of the steel, the column maintains its integrity and prevents catastrophic failure. The steel tube absorbs deformation and preserves structural resistance over a wide strain range. This synergy between the brittle high-strength FRP and ductile steel results in a stable and staged failure mechanism, extending both the

strength and ductility of the system.

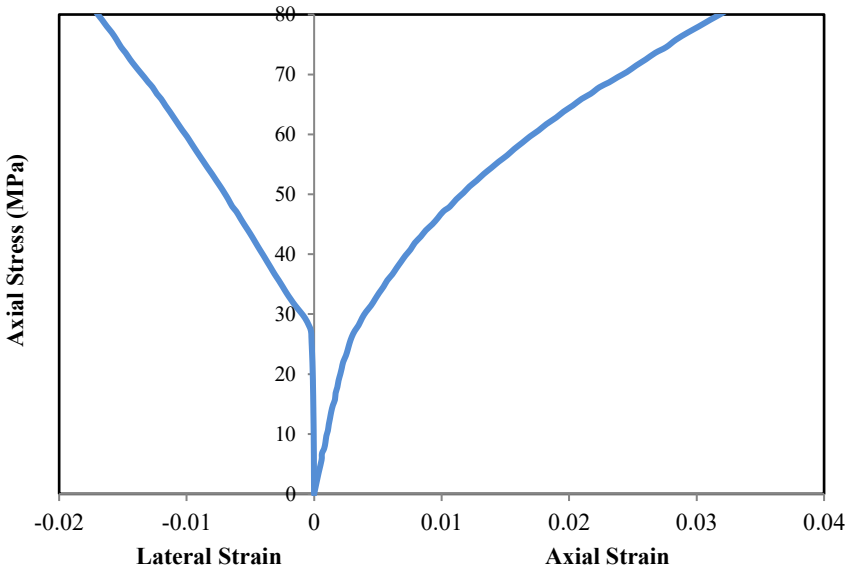

Fig. 12. Initial portion of axial stress-strain curves for confined concrete specimens.

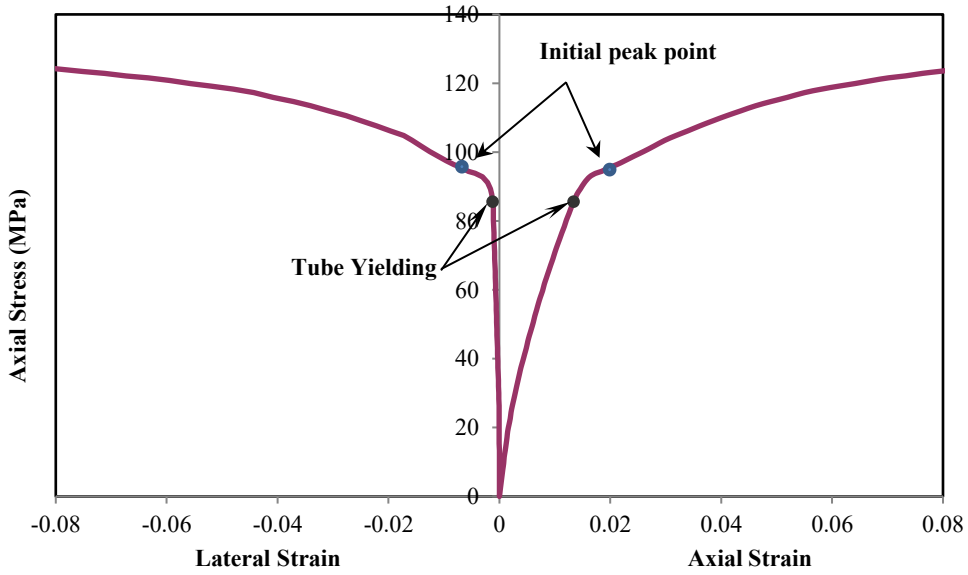

Fig. 13. Axial and lateral stress-strain curve of steel-confined concrete specimen, showing yielding and post-yield behavior.

3.3. Volumetric strain

Volumetric strain response was evaluated to gain a deeper understanding of the confinement effect in each group. The volumetric strain–axial stress curves are presented in Figs. 15 to 17 for the FRP, steel, and hybrid-confined specimens, respectively.

3.3.1.FRP-confined specimens

As shown in Fig. 15, the volumetric strain response of FRP-confined concrete begins with a positive slope, indicating a contraction behavior up to approximately the unconfined compressive strength f_c'. This phase corresponds to the compaction of internal voids and early crack closure. After reaching f_c', the slope turns negative, signifying a transition from contraction to dilation, as a result of increasing micro-cracking and internal damage. As the lateral strain increases, the internal pressure intensifies until it reaches the rupture limit of the FRP shell, causing a sudden drop in confinement. This rupture leads to a sharp and immediate increase in volumetric strain. Shortly after rupture, the curve exhibits a temporary rebound (i.e., a partial recovery of slope), reflecting the release of stored elastic energy in the FRP and concrete core. However, this recovery is short-lived, and the system soon transitions into a softening phase dominated by the rapid volumetric expansion of the now-unconfined concrete core.

3.3.2.Steel-confined specimens

The volumetric strain curve of the steel-confined specimen is illustrated in Fig. 16. Prior to the yielding of the steel tube, the behavior is predominantly contractive, and even after the axial stress reaches f_c', the core concrete remains well-confined. This is attributed to the high lateral stiffness of the steel tube, which effectively limits dilation. Once the steel yields, however, the rate of

lateral pressure increase slows down, and the volumetric strain curve shifts into the dilation region. Although strain hardening of the steel may delay this transition, it is not sufficient to entirely prevent it. As a result, post-yield volumetric expansion occurs, albeit less abruptly than in FRP-confined specimens.

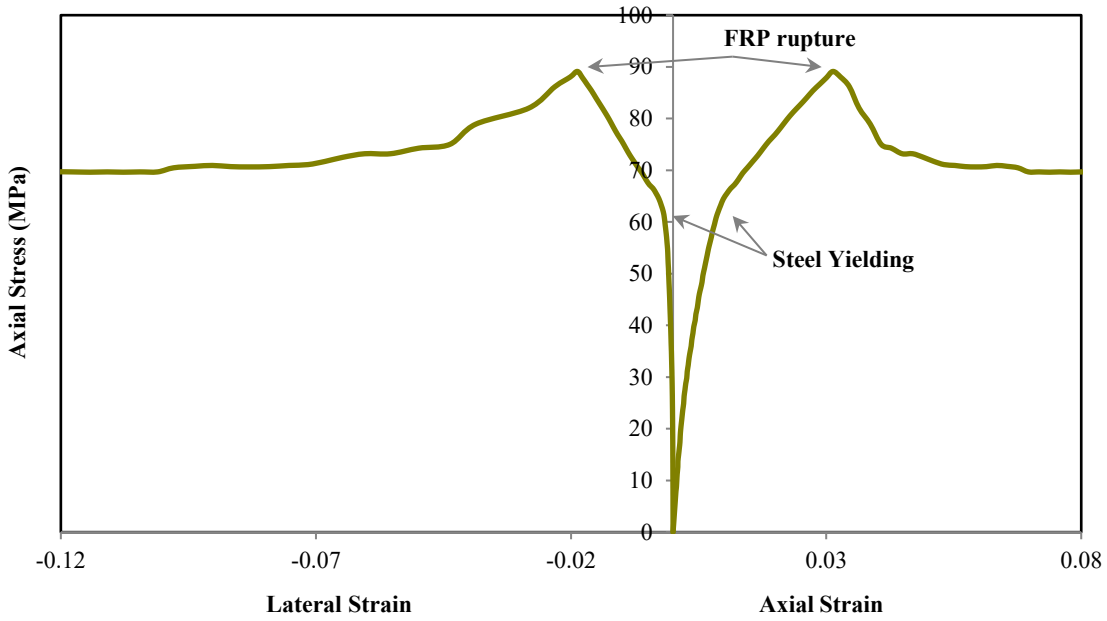

Fig. 14. Axial and lateral stress-strain response of a hybrid FRP–steel confined concrete specimen, indicating steel tube yielding followed by FRP rupture.

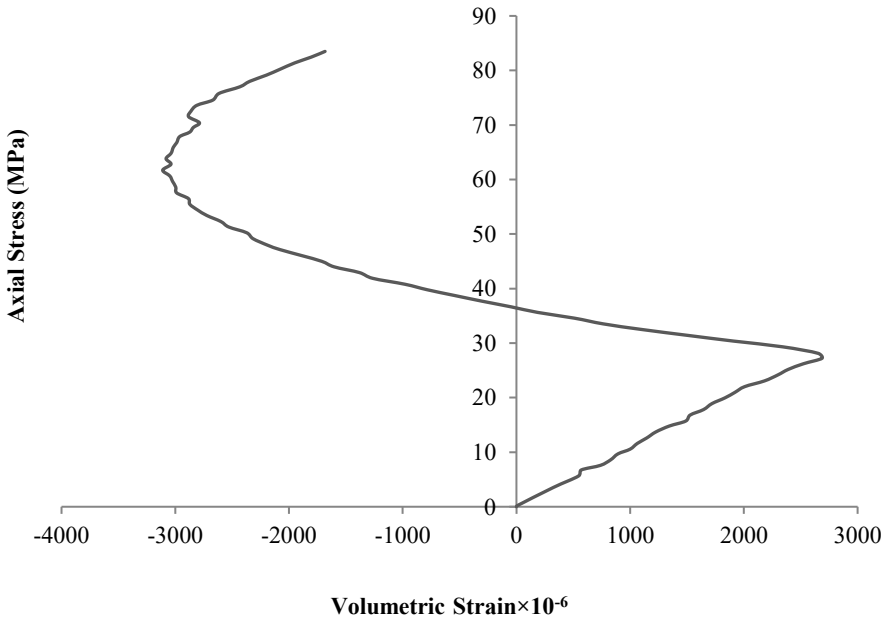

Fig. 15. Axial stress–volumetric strain curve of an FRP-confined concrete specimen.

3.3.3.Hybrid FRP–steel confined specimens

As shown in Fig. 17, prior to steel yielding, the hybrid-confined concrete exhibits a contractive volumetric behavior due to the high lateral stiffness of the combined FRP–steel tube. This confinement prevents noticeable internal cracking even at stress levels close to f_c'. Once the steel tube yields, the effective confinement stiffness drops significantly, resulting in a noticeable increase in volumetric strain and transition into the dilation phase. At this stage, microcracking and lateral deformation intensify. However, the rate of volumetric expansion is slower than in steel-only confined specimens because the FRP jacket remains intact and continues to apply lateral pressure. After the rupture of the FRP, the confinement capacity is significantly reduced, and the concrete core undergoes rapid lateral expansion. The post-rupture trend shows a steep increase in volumetric strain, confirming the loss of effective confinement and the onset of concrete softening under axial load.

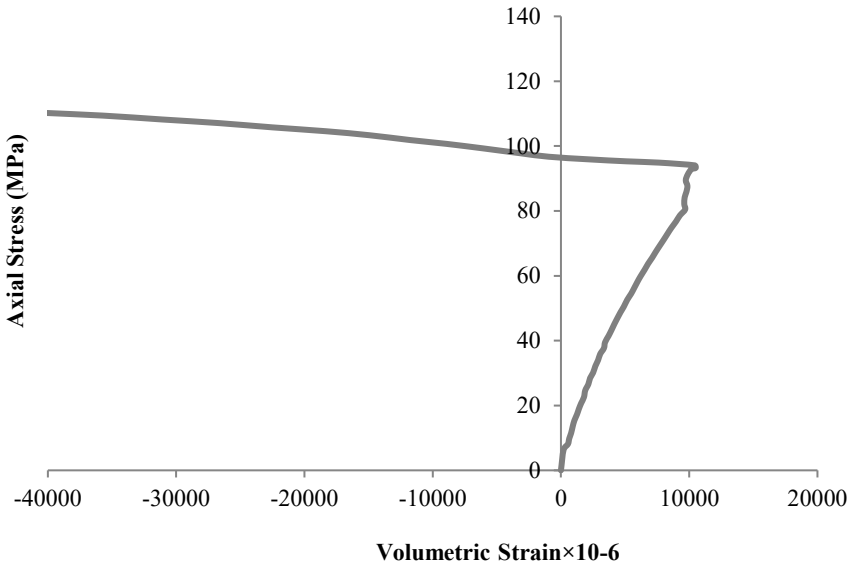

Fig. 16. Axial stress–volumetric strain curve of a steel-confined concrete specimen.

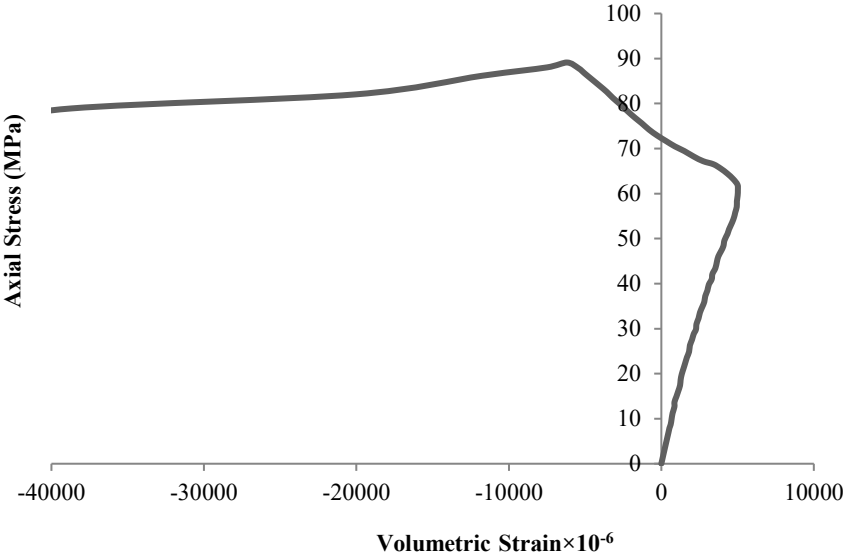

Fig. 17. Axial stress–volumetric strain curve of a hybrid FRP–steel confined concrete specimen.

4. Conclusion

This experimental study examined the axial behavior of concrete cylinders confined using steel tubes, FRP jackets, and hybrid FRP–steel tubes under identical confinement ratios. The comparison revealed distinct differences in failure mechanisms, stress–strain responses, and volumetric strain behavior across the confinement types.

In terms of failure mode, FRP-confined specimens failed suddenly due to brittle rupture of hoop fibers, while steel-confined specimens showed ductile bulging at mid-height. The hybrid specimens exhibited a staged failure sequence—initial FRP rupture followed by steel yielding and buckling—providing a more controlled and gradual failure process. The stress–strain behavior of the FRP group was bilinear with a sharp post-peak drop, indicating limited ductility. Steel-confined specimens maintained a smooth curve with extended post-peak strength due to strain hardening. Hybrid specimens demonstrated intermediate behavior, with high strength and improved post-peak ductility, reflecting the synergistic effect of FRP stiffness and steel ductility. Volumetric strain analysis confirmed these findings: FRP-confined specimens experienced rapid dilation post-rupture, while steel and hybrid groups exhibited more stable and restrained expansion. The hybrid group, in particular, delayed dilation onset and maintained better confinement after steel yielding and FRP rupture.

Overall, the hybrid FRP–steel system offered the most favorable balance between strength, ductility, and confinement effectiveness. It is recommended for applications demanding enhanced axial performance and failure control, particularly in seismic or durability-critical environments.

Statements & declarations

Author Contributions

Abolghasem Salari: Conceptualization, Investigation, Methodology, Formal analysis, Resources, Writing - Original Draft, Writing - Review & Editing.

Morteza Naghipour: Conceptualization, Methodology, Project administration, Supervision, Writing - Review & Editing.

Funding

The authors received no financial support for the research, authorship, and/or publication of this article.

Declarations

The authors declare no conflict of interest.

Data availability

The data presented in this study will be available on interested request from the corresponding author.

References

[1] Richart, F. E., Brandtzæg, A., Brown, R. L. A study of the failure of concrete under combined compressive stresses. Urbana (IL): University of Illinois, Engineering Experiment Station; 1928. Bulletin No.: 185.

[2] Newman, K., Newman, J. B. Failure theories and design criteria for plain concrete. In: Structure, Solid Mechanics and Engineering Design: Proceedings of the Southampton Civil Engineering Materials Conference; 1969; Southampton, UK. p. 963–995.

[3] Mander, J. B., Priestley, M. J. N., Park, R. Theoretical Stress-Strain Model for Confined Concrete. Journal of Structural Engineering, 1988; 114 (8): 1804–1826. doi:10.1061/(asce)0733-9445(1988)114:8(1804).

[4] Han, L. H., Liu, W., Yang, Y. F. Behavior of Thin Walled Steel Tube Confined Concrete Stub Columns Subjected to Axial Local Compression. Thin-Walled Structures, 2008; 46 (2): 155–164. doi:10.1016/j.tws.2007.08.029.

[5] Liu, J., Zhang, S., Zhang, X., Guo, L. Behavior and Strength of Circular Tube Confined Reinforced-Concrete (CTRC) Columns. Journal of Constructional Steel Research, 2009; 65 (7): 1447–1458. doi:10.1016/j.jcsr.2009.03.014.

[6] Qi, H., Guo, L., Liu, J., Gan, D., Zhang, S. Axial Load Behavior and Strength of Tubed Steel Reinforced-Concrete (SRC) Stub Columns. Thin-Walled Structures, 2011; 49 (9): 1141–1150. doi:10.1016/j.tws.2011.04.006.

[7] Lin, S., Zhao, Y. G., He, L. Stress Paths of Confined Concrete in Axially Loaded Circular Concrete-Filled Steel Tube Stub Columns. Engineering Structures, 2018; 173: 1019–1028. doi:10.1016/j.engstruct.2018.06.112.

[8] Xiamuxi, A., Zheng, T., Shao, J., Tan, T. Impact of Steel Tube Wall Thickness on Axial Compression Behavior of Reinforced and Recycled Aggregate Concrete-Filled Square Steel Tube Short Columns. Structures, 2024; 69: 107382. doi:10.1016/j.istruc.2024.107382.

[9] Cao, J., Jin, M., Chen, S., Ding, Q., Liu, J., Xiong, C., Jin, Z. Effect of Confinement of Steel Tube on Durability of Concrete Pier Exposed to Partial/Full Immersion Sulfate Attack Solution. Journal of Building Engineering, 2025; 99: 111477. doi:10.1016/j.jobe.2024.111477.

[10] Kurt, C. E. Concrete filled structural plastic columns. Journal of the Structural Division, ASCE. 1978; 104(1):55–63. doi:10.1061/jsdeag.0004849.

[11] Harmon T, Slattery K, Ramakrishnan S. The effect of confinement stiffness on confined concrete. In: Taerwe L, editor. Proceedings of the Second International RILEM Symposium (FRPRCS-2); 1995 Aug 23–25; Ghent, Belgium. Vol. 1. p. 584–592.

[12] Lam, L., Teng, J. G., Cheung, C. H., Xiao, Y. FRP-confined concrete under axial cyclic compression. Cement and Concrete Composites, 2006; 28(10): 949–958. doi:10.1016/j.cemconcomp.2006.07.007.

[13] Berthet, J. F., Ferrier, E., Hamelin, P. Compressive Behavior of Concrete Externally Confined by Composite Jackets: Part B: Modeling. Construction and Building Materials, 2006; 20 (5): 338–347. doi:10.1016/j.conbuildmat.2005.01.029.

[14] Li, G., Maricherla, D., Singh, K., Pang, S. S., John, M. Effect of Fiber Orientation on the Structural Behavior of FRP Wrapped Concrete Cylinders. Composite Structures, 2006; 74 (4): 475–483. doi:10.1016/j.compstruct.2005.05.001.

[15] Toutanji, H., Han, M., Matthys, S. Axial load behavior of rectangular concrete columns confined with FRP composites. In: Proceedings of the 8th International Symposium on Fiber-Reinforced Polymer Reinforcement for Concrete Structures (FRPRCS-8); 2007 Jul 16–18; Patras, Greece.

[16] Elsanadedy, H. M., Al-Salloum, Y. A., Alsayed, S. H., Iqbal, R. A. Experimental and Numerical Investigation of Size Effects in FRP-Wrapped Concrete Columns. Construction and Building Materials, 2012; 29: 56–72. doi:10.1016/j.conbuildmat.2011.10.025.

[17] Yang, Z., He, C., Kong, Q., Yuan, C. Monitoring the Microcrack Evolution in FRP-Wrapped Concrete Using Diffuse Ultrasound. Journal of Building Engineering, 2025; 109. doi:10.1016/j.jobe.2025.113009.

[18] Zheng, Y., Xu, F. H., Wang, D., Liang, M. Evaluating Ultimate Axial Strain Models for Concrete Square and Rectangular Columns Confined with FRP Composites. Journal of Physics: Conference Series, 2025; 3005 (1): 12008. doi:10.1088/1742-6596/3005/1/012008.

[19] Xiao, Y., He, W., Choi, K. Confined Concrete-Filled Tubular Columns. Journal of Structural Engineering, 2005; 131 (3): 488–497. doi:10.1061/(asce)0733-9445(2005)131:3(488).

[20] Feng, P., Cheng, S., Bai, Y., Ye, L. Mechanical Behavior of Concrete-Filled Square Steel Tube with FRP-Confined Concrete Core Subjected to Axial Compression. Composite Structures, 2015; 123: 312–324. doi:10.1016/j.compstruct.2014.12.053.

[21] Ma, L., Zhou, C., Lee, D., Zhang, J. Prediction of Axial Compressive Capacity of CFRP-Confined Concrete-Filled Steel Tubular Short Columns Based on XGBoost Algorithm. Engineering Structures, 2022; 260: 114239. doi:10.1016/j.engstruct.2022.114239.

[22] Liu, K. H., Xie, T. Y., Cai, Z. K., Chen, G. M., Zhao, X. Y. Data-Driven Prediction and Optimization of Axial Compressive Strength for FRP-Reinforced CFST Columns Using Synthetic Data Augmentation. Engineering Structures, 2024; 300: 117225. doi:10.1016/j.engstruct.2023.117225.

Civil Engineering and Applied Solutions

Research Article

journal homepage: ceas.journals.umz.ac.ir

CEAS Civil Engineering and Applied Solutions

Life Cycle Environmental Impact of High-Strength and Lightweight Pozzolanic Concretes

Mohammad-Amin Dashab [a], Mostafa Kazemi [b*]

[a] *Department of Civil Engineering, Iranshahr Branch, Islamic Azad University, Iranshahr, Sistan and Baluchestan, Iran*
[b] *Industrial Minerals & Blends Laboratory, Euroquartz s.a., Hermalle-Sous-Argenteau, Belgium*

ARTICLE INFO

Keywords:
Environmental assessment
Life cycle
Highs concrete
Lightweight concrete
Pozzolan
Sustainable development

Article history:
Received 23 May 2025
Accepted 12 June 2025
Available online 1 July 2025

ABSTRACT

This study evaluates the environmental and economic performance of six innovative concrete mixtures using Life Cycle Assessment (LCA) and cost analysis. The concrete types incorporate various industrial and agricultural by-products, including PET waste, steel fibers, nano-silica, pumice, ceramic waste, EAF slag, asbestos cement sheets, and rice husk ash. Using the CML 2001, IMPACT 2002+, and ReCiPe methods, environmental impacts were assessed across key categories, such as global warming potential, toxicity, and resource depletion. Results indicate that conventional concrete had the lowest environmental burden overall, while PET/steel fiber concrete showed the highest impact in most categories. Sensitivity analysis identified cement as the primary contributor to environmental damage, followed by micro-silica in select mixes. The economic analysis identified conventional concrete as the most cost-effective, followed by pumice and PET/steel fiber concretes, which were 19.3% and 69.6% more expensive, respectively. Integrating environmental and cost factors revealed that, despite its relatively low cost, PET/steel fiber concrete contributed the most to CO_2 emissions. These findings support more informed material selection for sustainable construction.

1. Introduction

The construction industry is a major contributor to global environmental degradation, largely due to intensive energy use, raw material extraction, and emissions from material production from cement manufacturing, as concrete is the most widely used construction material [1, 2]. The key challenge is balancing the rising global demand for cement and concrete with the urgent need to reduce CO_2 emissions. In response, sustainable concrete structures have gained growing attention, particularly in countries with stringent environmental regulations. A range of strategies has been developed to minimize the environmental footprint of concrete-based infrastructure. These impacts are closely tied to the composition and properties of the materials used in concrete production. As concrete is central to urban development, it contributes to the high emissions from cities, estimated at 70% of global totals. In line with the Kyoto Protocol, this has driven the development of tools to assess the environmental performance of buildings across their life cycle [3]. To effectively address these environmental challenges in the concrete and construction sectors, it is essential to adopt a comprehensive and scientifically grounded evaluation tool-Life Cycle Assessment (LCA) [4].

Given the complexity of materials, energy flows, and processes involved, a systematic analytical approach like LCA is indispensable. LCA enables the comparison and evaluation of environmental impacts across different product systems using a standardized functional unit [5]. According to ISO guidelines, LCA covers the full "cradle-to-grave" span of a product—from raw material acquisition to production, use, recycling, and final disposal [6]. There are two main LCA approaches: process-based LCA, which tracks detailed inputs and outputs for specific processes and is commonly used in construction, and Economic Input-Output LCA (EIO-LCA), which evaluates impacts at a broader economic level [7]. The LCA methodology, as defined by ISO [8], involves four key phases: goal and scope definition, life cycle inventory (LCI) analysis, life cycle impact assessment (LCIA), and

* Corresponding author.
E-mail addresses: kazemi.civil68@gmail.com (M. Kazemi).

https://doi.org/10.22080/ceas.2025.29312.1014
ISSN: 3092-7749/© 2025 The Author(s). Published by University of Mazandaran.
This article is an open access article distributed under the terms and conditions of the Creative Commons Attribution (CC-BY) license (https://creativecommons.org/licenses/by/4.0/deed.en)
How to cite this articleKazemi, M., Dashab, M. Life Cycle Environmental Impact of High-Strength and Lightweight Pozzolanic Concretes. Civil Engineering and Applied Solutions. 2025; 1(2): 14–30. doi: 10.22080/ceas.2025.29312.1014.

interpretation. These steps help quantify various environmental parameters, including global warming potential, resource depletion, toxicity, acidification, and more.

LCA highlights material composition as a key factor in environmental impact. Cement, the main binder in concrete, is a major CO_2 emitter due to fuel combustion and limestone decomposition. Smaller emissions also result from electricity use and the release of other gases like NO_x and CH_4 during production [9]. Producing one ton of cement emits about 930 kg of CO_2-mainly from limestone decomposition (500 kg), fuel combustion (350 kg), and electricity use (80 kg). NO_x emissions vary by fuel type and kiln technology, ranging from 1.5–9 kg per ton [10]. To reduce emissions, Portland cement is often partially replaced with pozzolanic materials—natural or artificial substances that react with calcium hydroxide to form cement-like compounds [11]. Enhancing concrete sustainability also involves reducing the use of virgin aggregates, which make up 70–80% of its weight and 60–70% of its volume [12]. Concrete aggregates are classified as natural or artificial. Natural aggregates-mainly sand and gravel-are cost-effective and commonly sourced from deposits or quarries. However, their extraction through mining can significantly damage rivers and ecosystems, highlighting the need to reduce reliance on these materials [13, 14]. To reduce reliance on natural aggregates, recycled or artificial alternatives are used. Recycled aggregates come from construction waste but often have lower quality due to high water absorption and reduced strength. In contrast, artificial aggregates made from industrial by-products like EAF slag and GGBFS offer better performance and help address waste disposal, supporting environmental sustainability [15]. In addition to aggregates, additives—though used in smaller quantities-play a key role in enhancing concrete performance. Concrete additives are generally classified into two main groups: chemical additives and mineral additives [16].

Francesco Colangelo et al. [17], in their study on the LCA of various concrete types containing waste for sustainable construction, assessed the environmental impacts of all samples using the SimaPro software. The environmental damage analysis (including resource use, ecosystem quality, and human health) revealed that human health is the primary area of concern. Demiral et al. [18] conducted a cradle-to-gate life cycle assessment of self-compacting mortars with fly ash and PET waste using SimaPro and the ReCiPe database. The results showed that incorporating recycled materials reduces environmental impacts by conserving natural aggregates and minimizing landfill waste. Asadollahfardi et al. [19] conducted a cradle-to-gate LCA on five concrete types using SimaPro 8.1. Geopolymer concrete showed a 26% lower global warming potential than ordinary concrete, while micro-silica, nano-silica, and micro-nanobubble concretes had increases of 56%, 17%, and 38%, respectively. Overall, ordinary concrete had the lowest environmental impact during production. Billel et al. [20] showed that using natural volcanic pozzolans improved concrete strength, insulation, and reduced density. A 25% substitution of black pozzolan powder was optimal, offering both economic and environmental benefits. Ersan et al. [21] used cradle-to-gate LCA to compare ordinary and lightweight concretes. Lightweight concrete had 13% lower greenhouse gas emissions, and recycled plastic waste proved to be a sustainable alternative to natural aggregates. Shahmansouri et al. [22] found that adding natural zeolite to concrete exposed to aggressive environments reduced global warming potential, with 20% zeolite achieving the lowest impact. Napulano et al. [23] used LCA to compare lightweight concretes and found that those made with recycled aggregates had significantly lower environmental impacts than those with natural aggregates. Valipour et al. [24] found that replacing 30% of cement with natural zeolite in green concrete significantly reduced global warming potential over a 15-year lifecycle in marine environments. Nath et al. [25] showed that replacing 30–40% of cement with fly ash in marine concrete reduced the carbon footprint by up to 23% and energy use by nearly 10%, while also enhancing durability. However, high-strength concrete increased CO_2 emissions due to higher cement content.

To support informed material selection for sustainable and low-carbon construction, this study focuses on the environmental and economic assessment of high-strength and lightweight concrete mixtures incorporating pozzolanic and recycled materials. Six mix designs were developed, including one conventional concrete and five alternatives containing materials such as pumice, PET waste with steel fibers, nano-silica, ceramic waste with electric arc furnace slag (EAFS), and asbestos cement sheets with rice husk ash. A process-based LCA was conducted following ISO 14040/44 standards [26], using a cradle-to-gate system boundary that includes raw material extraction, transportation, and concrete production. In parallel, an economic analysis was performed based on material and energy costs. To evaluate the robustness of the environmental results and identify key contributing factors, a sensitivity analysis was also conducted by varying input quantities. This integrated approach offers a comprehensive basis for assessing the trade-offs between sustainability and cost in concrete mix design.

2. Materials and methods

2.1. Concrete mix designs

Six concrete mixtures were developed and assessed in this study. Table 1 summarizes their compositions and characteristics. These mixes include:

- Conventional concrete: 42 MPa compressive strength, water-to-cement (w/c) ratio of 0.50
- Pumice concrete: 23 MPa compressive strength, w/c ratio of 0.27
- PET/steel fiber concrete: 35 MPa compressive strength, w/c ratio of 0.30
- Recycled fine aggregate with nano-silica concrete: 40 MPa compressive strength, w/c ratio of 0.50
- Ceramic and EAF slag concrete: 40 MPa compressive strength, w/c ratio of 0.40
- Asbestos cement sheet and rice husk ash concrete: Mix details presented in Table 1.

Table 1. Mix design of concrete types.

Material/type of concrete	Asbestos and rice husk ash	Ceramics and EAFS	Nano-Silica	PET and fibers	Pumice	Ordinary
Portland cement	425	448	404.2	477	468.3	430
water	215	215	215	157	126.7	215
gravel	522	445	855.5	1.04	-	845
Pumice aggregate	-	-	-	-	200.7	-
sand	570.7	275	-	95	-	855
Recycled fines	-	-	793.1	-	-	-
Micro-silica	-	-	-	-	46.8	-
Nano-silica	-	-	25.8	-	-	-
plasticizer	2.1	-	0.4	0.92	0.85	-
PET waste	-	-	-	36.7	-	-
Steel fibers	-	-	-	78.5	-	-
Silica fume	-	-	-	53	-	-
Ceramic	-	52	-	-	-	-
Slag	-	445	-	-	-	-
Rice husk ash	75	-	-	-	-	-
Asbestos cement	387.8	-	-	-	-	-

2.2. Life Cycle Assessment (LCA)

This study employed a process-based LCA using the cradle-to-gate approach, in accordance with ISO 14040/44 standards [26]. The LCA was structured into four main phases: goal and scope definition, inventory analysis, impact assessment, and interpretation.

2.2.1.Goal and scope definition

The primary goal was to evaluate and compare the environmental impacts associated with producing 1 m³ of each concrete type. The cradle-to-gate system boundary includes raw material extraction, transportation, and concrete production. Fig. 1 illustrates the system boundaries applied in this study.

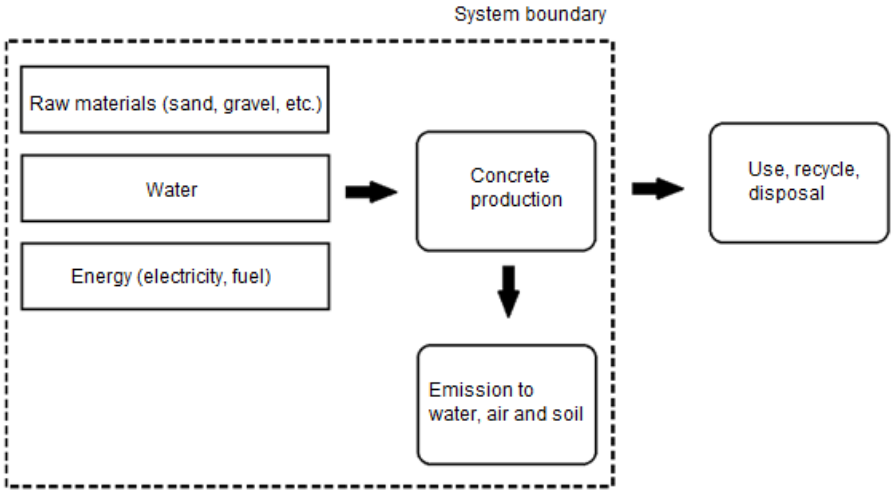

Fig. 1. System boundaries for the production of 1 cubic meter.

2.2.2.Inventory analysis

The life cycle inventory (LCI) data were sourced primarily from the Ecoinvent database and integrated into SimaPro software for analysis. Material quantities and transport distances were carefully recorded for each mix, and energy consumption for production was standardized to 157.9 kWh per m³.

2.2.3.Transportation and energy use

Material transport was modeled using Euro 4 standard trucks with a capacity of 16–32 tons, based on data from the Ecoinvent database integrated into SimaPro. A uniform transport distance of 70 kilometers was assumed for all raw materials. According to

Turner and Collins [27], the CO_2 emission factor for producing and delivering 1 m^3 of concrete, including mixing and transport to a construction site, is 0.0033 kg CO_2. Additionally, emissions related to energy use-such as on-site preparation, access construction, and concrete pumping-were estimated at 0.0094 kg CO_2 per m^3. The energy demand for producing 1 m^3 of ready-mix concrete was taken as 568.6 MJ [28], equivalent to 157.9 kWh, and was applied uniformly across all mix designs in this study.

2.2.4. Software input and mix-specific inventory

Each mix's LCI was entered into SimaPro with full consideration of raw material types, packaging, transport (in tonne-kilometers), and energy use. Tables A-1 through A-6 detail these inventories for all six concrete types.

2.3. Impact assessment and interpretation

The assessment focused on three key areas: human health, ecosystem quality, and resource depletion, following a cradle-to-gate LCA in accordance with ISO 14040/44 [26]. To quantify these impacts, three established methods were applied: CML 2001, ReCiPe, and IMPACT 2002+. These methods offer complementary perspectives by covering both midpoint and endpoint indicators. Midpoint metrics-such as GWP, acidification, and eutrophication-were used to assess specific environmental effects. CML 2001 focuses on these categories, while IMPACT 2002+ extends the analysis to endpoint-level damage, capturing broader implications for human health, ecosystem integrity, climate systems, and resource availability. Impact categories were selected based on their relevance to construction sustainability. This section describes the assessment framework and does not include an interpretation of the results.

2.4. Sensitivity analysis and economic evaluation

Sensitivity analysis was conducted to examine how variations in material quantities affect the environmental outcomes of the LCA [29]. This involved adjusting the volume of all input materials in each concrete mix by ±25%, a standard variation used in LCA studies to reflect typical fluctuations in raw material supply and production conditions. This approach helps assess the robustness of the results and identify parameters with the greatest influence on environmental impact, thereby improving confidence in the findings.

In parallel, an economic evaluation was performed to assess the cost-effectiveness of each concrete mix. The total cost of producing 1 cubic meter of concrete was calculated based on the unit price of all constituent materials and the energy required for production. Energy costs were included using a standard rate per kilowatt-hour. This integrated analysis enabled a comparison of both environmental performance and production costs across the different mix designs.

3. Results

The following section presents the results of the environmental and economic evaluations of the six concrete mixtures. It includes detailed analyses using multiple LCA methods, followed by a sensitivity analysis and cost comparison.

3.1. environmental impact assessment

The results of the evaluation using the CML2001, IMPACT 2002+, and ReCiPe methods for normal concrete, pumice, PET, and fiber concrete, nano-silica concrete, ceramic and EAFS concrete, and asbestos and rice husk ash concrete are presented.

3.1.1. Environmental impact results using the CML 2001 method

The environmental impacts of the six concrete mixtures were assessed using the CML 2001 method, focusing on global warming potential, human toxicity, terrestrial ecotoxicity, and acidification as key midpoint indicators.

As presented in **Table 2**, conventional concrete exhibited the lowest environmental burdens in all categories, including global warming (564.66 kg CO_2 eq), human toxicity (77.38 kg 1,4-DB eq), terrestrial ecotoxicity (0.75 kg 1,4-DB eq), and acidification (1.47 kg SO_2 eq). On the other hand, the PET and fiber concrete mix had the highest values for global warming (939.32 kg CO_2 eq), human toxicity (588.98 kg 1,4-DB eq), terrestrial ecotoxicity (2.22 kg 1,4-DB eq), and acidification (3.11 kg SO_2 eq), reflecting its intensive material and energy inputs.

Table 2. CML 2001-based environmental impact values across four midpoint categories.

Concrete type	Global warming (kg CO_2 eq)	Human toxicity (kg 1,4-DB eq)	Terrestrial ecotoxicity (kg 1,4-DB eq)	Acidification (kg SO_2 eq)
Conventional concrete	564.66	77.38	0.75	1.47
Pumice concrete	736.64	272.8	0.95	2.36
PET and fiber concrete	939.32	588.98	2.22	3.11
Nano-silica concrete	586.09	187.32	0.84	1.97
Ceramic and EAFS concrete	898.72	119.87	1.04	2.09
Asbestos and rice husk ash concrete	706.56	118.06	1.10	2.23

Fig. 2 illustrates the relative share of each concrete type's contribution to total environmental damage in percentage terms. PET and fiber concrete had the highest contributions in all categories: global warming (91.3%), human toxicity (60.2%), and ecotoxicity (57.6%). In contrast, conventional concrete consistently showed the lowest percentage contributions, with values of 54.9%, 8.33%, 19.4%, and 12.9% across the respective categories.

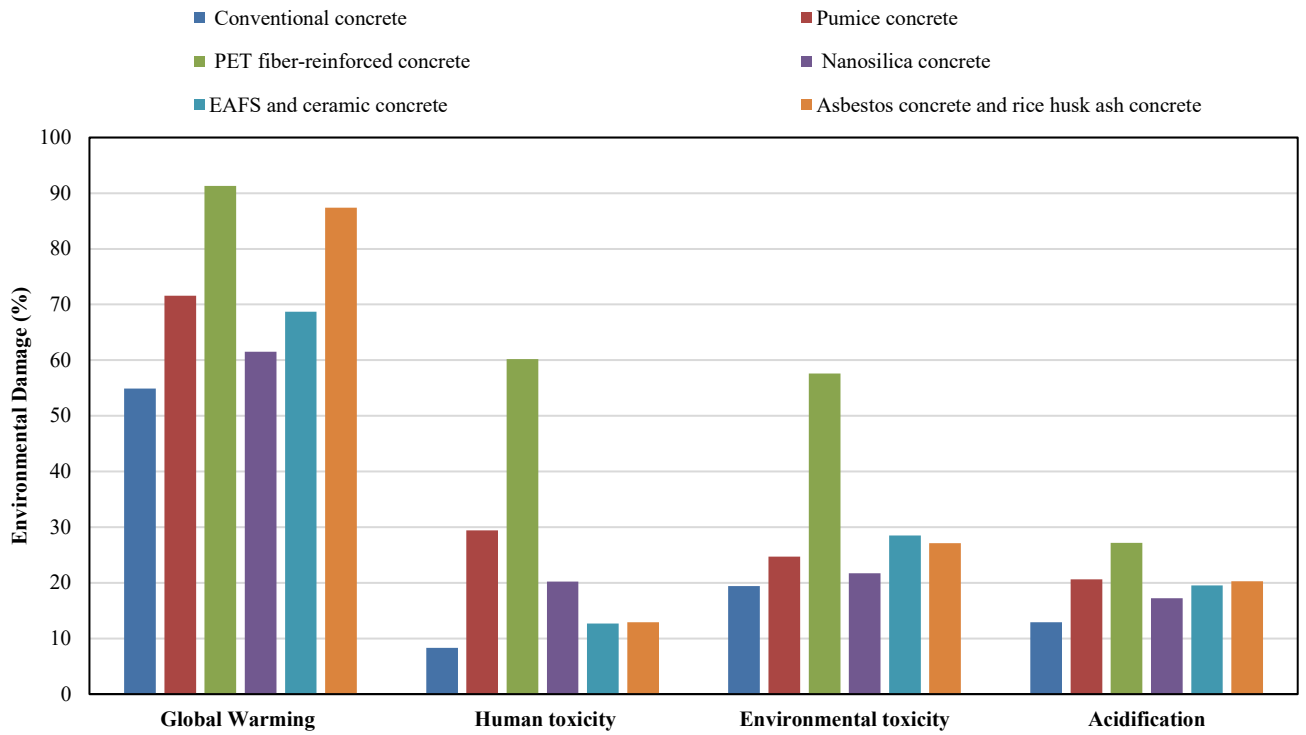

Fig. 2. Percentage contribution of six concrete mixtures to global warming, human toxicity, terrestrial ecotoxicity, and acidification, as assessed by the CML 2001 method.

3.1.2. Environmental impact results using the IMPACT 2002+ method

The environmental performance of the concrete mixtures was further evaluated using the IMPACT 2002+ method, which combines both midpoint and endpoint indicators. This dual-level approach provides a more comprehensive view of environmental damage by considering specific emissions and their broader consequences on human health, ecosystems, climate, and resource availability. As shown in **Table 3**, conventional concrete had the lowest environmental impact across all midpoint categories: global warming (553.26 kg CO_2 eq), ozone layer depletion (0.000031 kg CFC-11 eq), and mineral extraction (4.87 MJ surplus). In contrast, PET and fiber concrete recorded the highest values in global warming (888.98 kg CO_2 eq), ozone layer depletion (0.000053 kg CFC-11 eq), and mineral extraction (37.73 MJ surplus).

Table 3. Characterization results of six concrete mixtures across selected midpoint impact categories using the IMPACT 2002+ method.

Concrete type	Global warming (kg CO_2 eq)	Ozone layer depletion (kg CFC-11 eq)	Mineral extraction (MJ surplus)
Conventional concrete	553.26	0.000031	4.87
Pumice concrete	696.6	0.000044	5.87
PET concrete and fibers	888.98	0.000053	37.73
Nanosilica concrete	605.87	0.000040	5.66
Ceramic concrete and EAFS	884.22	0.000039	13.61
Asbestos concrete and rice husk ash	635.82	0.000038	8.51

Table 4 summarizes the endpoint damage categories including human health (DALY), ecosystem quality, climate change, and resource use. Conventional concrete again had the lowest values in all categories. The PET and fiber concrete had the highest damage across all endpoints: 0.00090 DALY for human health, 265.79 PDF·m²·yr for ecosystem damage, 888.98 kg CO_2 eq for climate change, and 11,837.7 MJ for resource use. Pumice concrete and ceramic/EAFS concrete also exhibited elevated environmental burdens, particularly in climate change and resource categories.

The percentage contribution of each concrete type to total environmental damage is illustrated in Fig. 3. PET and fiber concrete had the highest relative burden in all categories, exceeding 90% in climate change and human health. Pumice concrete also showed substantial impacts: 62.1% in human health and 80.6% in resource depletion. In the ecosystem quality category, asbestos and rice husk ash concrete contributed 22.1%, while ceramic and EAFS concrete showed a strong impact on climate change (89.6%), closely following the PET mix.

Table 4. Damage assessment results of six concrete mixtures across endpoint categories using the IMPACT 2002+ method.

Concrete type	Human health (DALY)	Ecosystem quality ($PDF^{1}*m^{2}*yr$)	Climate change (kg CO_2 e)	Resources (MJ primary)
Conventional concrete	0.00028	99.17	553.26	4388.20
Pumice concrete	0.00062	193.34	696.68	9542.15
PET concrete and fibers	0.00090	265.79	888.98	11837.70
Nanosilica concrete	0.00036	122.87	568.00	5713.39
Ceramic concrete and EAFS	0.00069	131.68	884.22	5856.81
Asbestos concrete and rice husk ash	0.00039	225.13	637.76	5481.01

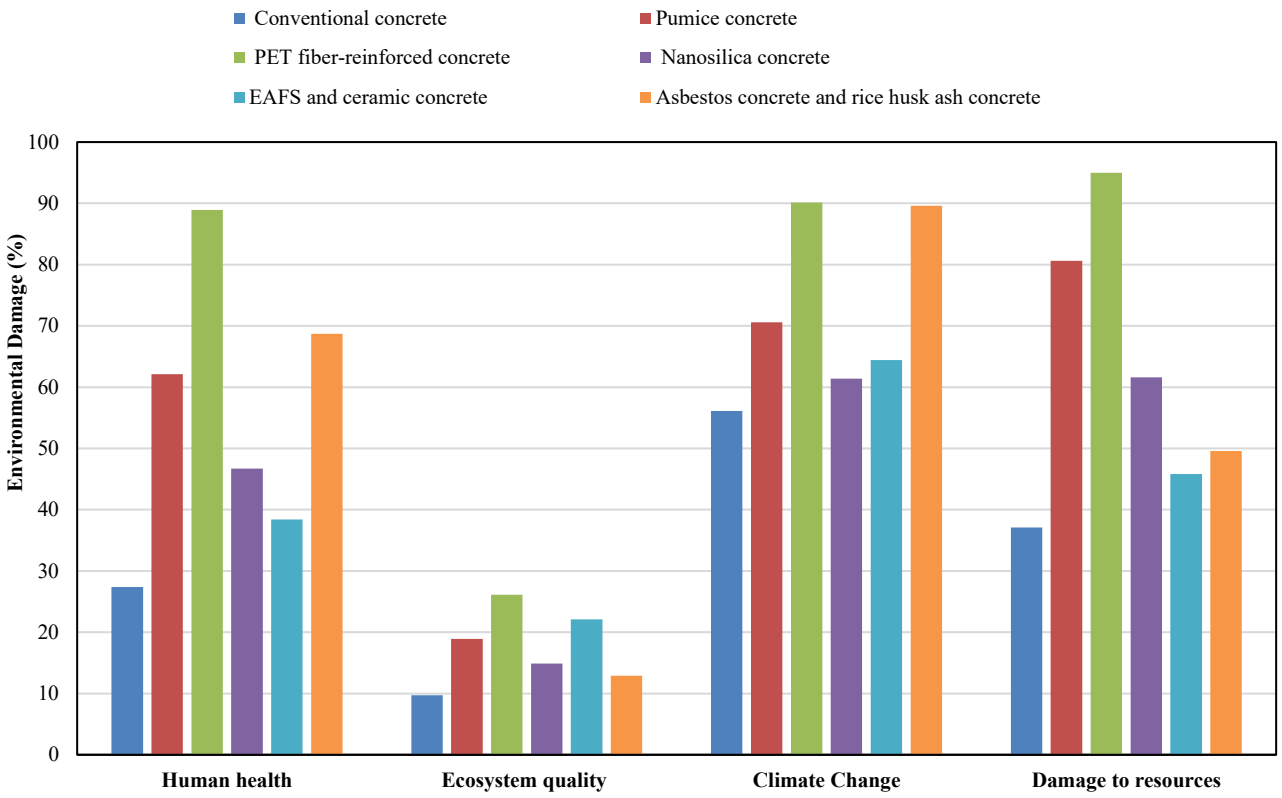

Fig. 3. Relative environmental damage of six concrete types across IMPACT 2002+ endpoint categories (percentage contribution).

3.1.3. Environmental impact results using the recipe method

The environmental burdens of the concrete mixes were also evaluated using the ReCiPe 2016 method, which integrates midpoint impacts into aggregated endpoint damage categories: human health, ecosystems, and resources. This method enables direct comparison across different environmental dimensions in a unified damage framework.

As presented in **Table 5**, conventional concrete consistently exhibited the lowest environmental damage across all categories, with the smallest values for human health (0.0009 DALY), ecosystems (0.00000051 species·yr), and resource use (USD 33.03). In contrast, PET and fiber concrete showed the highest impact on human health (0.0022 DALY), while asbestos and rice husk ash concrete resulted in the greatest damage to ecosystems (0.00000041 species·yr) and resources (USD 69.32). These outcomes reflect the influence of high embodied energy, waste processing, and additive-intensive mix designs in alternative concretes.

Table 5. Endpoint damage results for six concrete mixes based on the ReCiPe 2016 method.

Concrete type	Human health (DALY)	Ecosystems (species.yr)	Resources (USD2013)
Conventional concrete	0.0009	0.0000051	33.03
Pumice concrete	0.0015	0.0000031	44.5
PET concrete and fibers	0.0022	0.0000040	53.06
Nanosilica concrete	0.0011	0.0000026	39.85
Ceramic concrete and EAFS	0.0016	0.0000033	38.47

[1] Potentially Disappeared Fraction

Asbestos concrete and rice husk ash	0.0012	0.0000041	69.32

Fig. 4 illustrates the percentage contribution of each mix to total environmental damage in the three endpoint categories. PET and fiber concrete dominated the human health category with a 64.5% share, while asbestos/rice husk ash concrete had the highest impact on ecosystems (62%) and resource use (97%). As expected, conventional concrete contributed the least across all categories, reinforcing its comparatively lower environmental burden under the ReCiPe method.

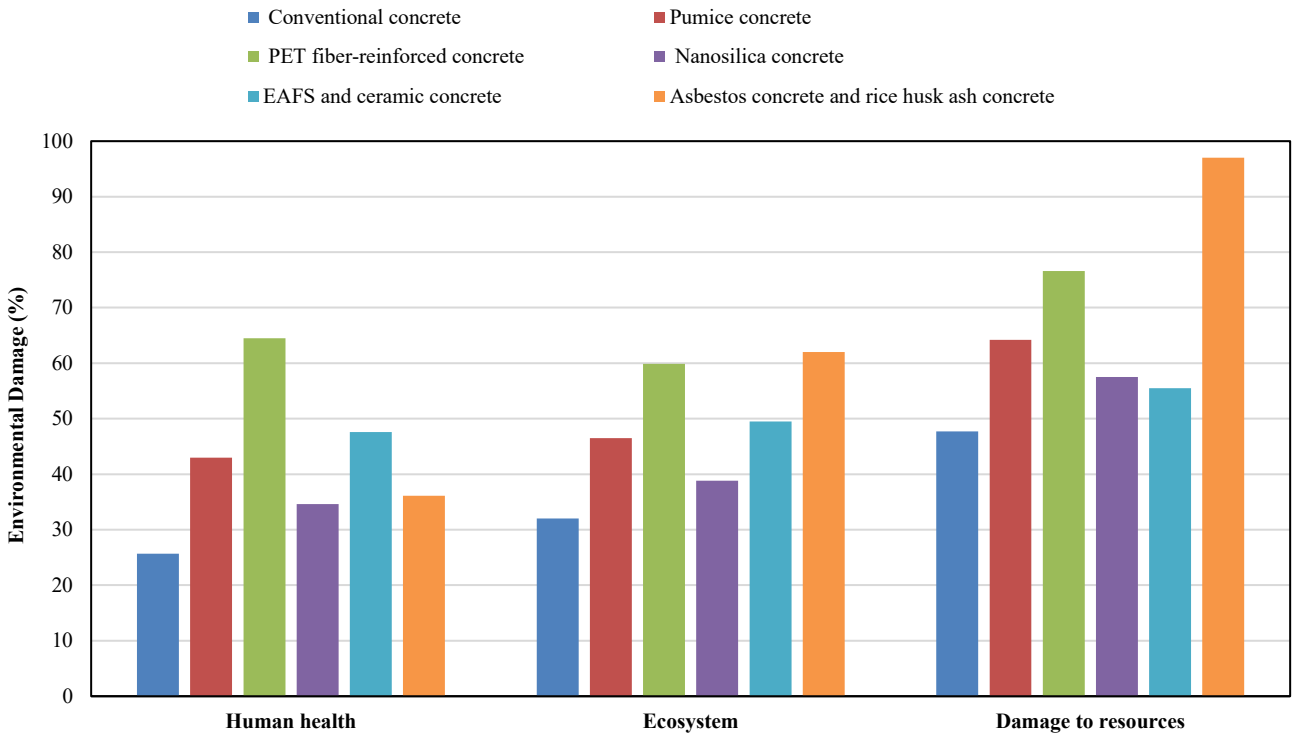

Fig. 4. Relative contribution of six concrete types to ReCiPe 2016 endpoint impact categories (in percentage).

3.2. Sensitivity analysis

To assess the robustness of the life cycle assessment results, a sensitivity analysis was conducted using the IMPACT 2002+ method by applying a ±25% variation in key input materials for each concrete mix. The IMPACT 2002+ method was used for this analysis, as it includes both midpoint and endpoint indicators, allowing for a comprehensive view of environmental effects. The aim was to identify which components had the greatest influence on overall environmental damage across four key categories: human health, ecosystem quality, climate change, and resource use.

3.2.1. Conventional concrete

As shown in Fig. 5, varying the cement content by ±25% had a clear impact across all damage categories. A 25% increase led to a 16.5% rise in climate change potential, while a 25% decrease reduced it by 19.8%. These results confirm cement as the most influential contributor to environmental impacts in this mix.

3.2.2. Pumice concrete

According to Fig. 6, the micro-silica content showed the highest sensitivity. A 25% increase led to rises of 16.3% in human health damage and 15.6% in resource use. In contrast, changes in pumice content produced minimal environmental variation, indicating its relatively low impact.

3.2.3. Pet and fiber concrete

As illustrated in Fig. 7, both micro-silica and PET significantly influenced environmental outcomes. Increasing micro-silica led to 10.5% more human health damage and 11.9% more resource use. Additionally, a 25% increase in cement caused a substantial 11.7% increase in climate change impact.

3.2.4. Nano-silica concrete

Fig. 8 highlights cement as the dominant factor in this mix, with a 25% increase resulting in a 10.5% rise in human health damage and 12.2% in ecosystem degradation. Nano-silica showed moderate sensitivity, while electricity consumption had the greatest effect

on the resource use category.

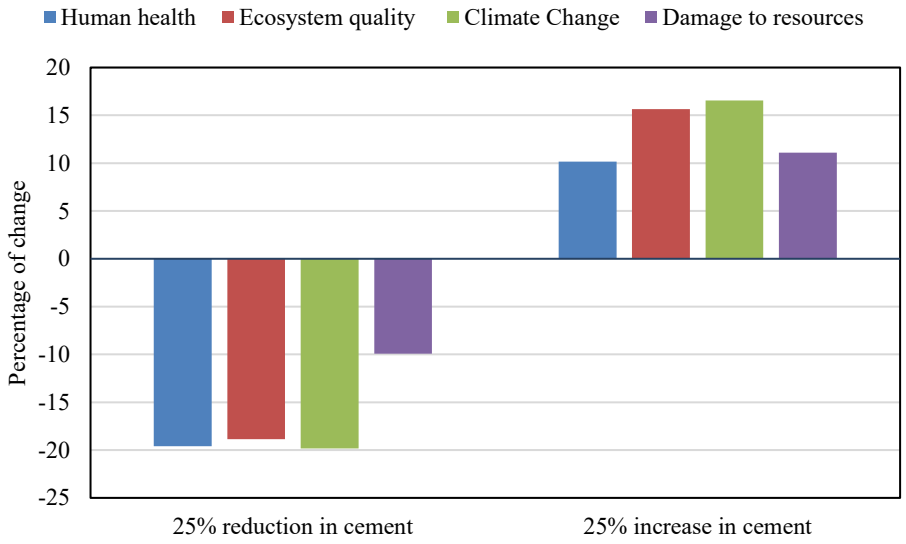

Fig. 5. Sensitivity analysis of conventional concrete under ±25% input variation using the IMPACT 2002+ method.

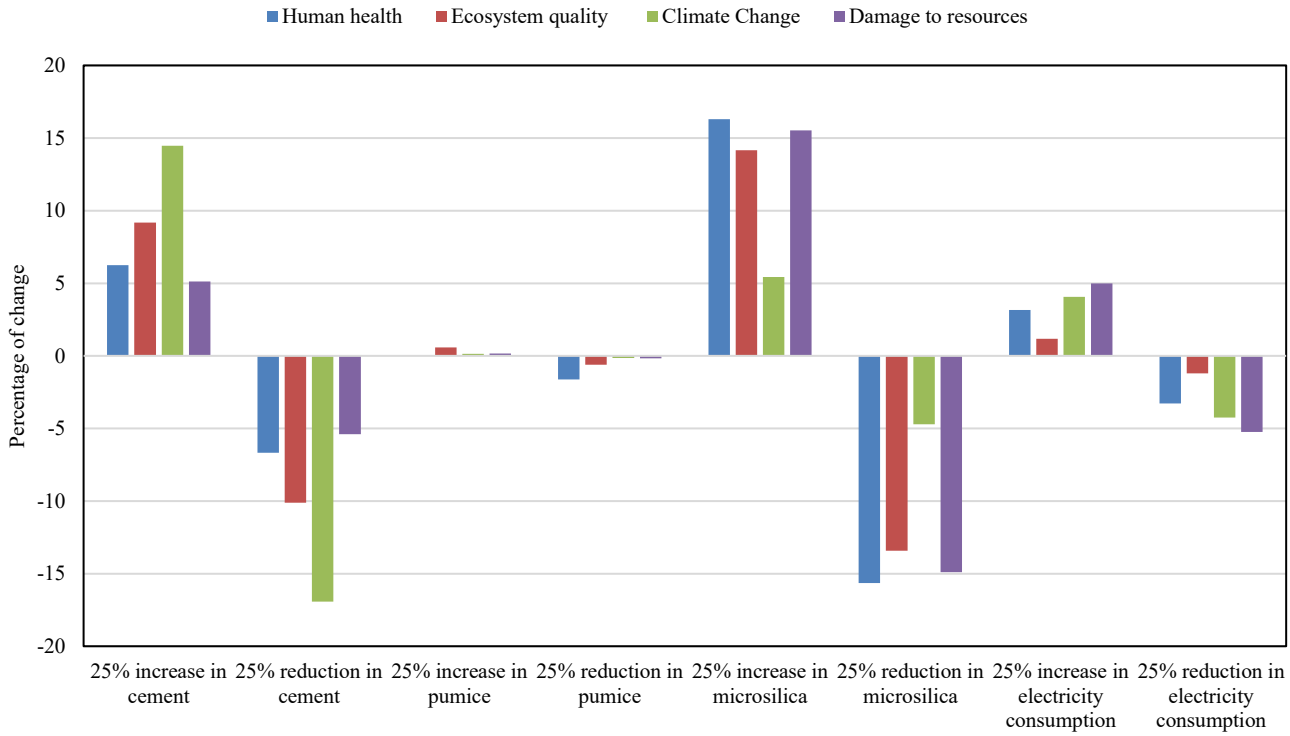

Fig. 6. Sensitivity analysis of pumice concrete under ±25% input variation using the IMPACT 2002+ method.

3.2.5. Asbestos and rice husk ash concrete

Fig. 9 shows that both cement and electricity considerably influenced climate change and human health categories. Notably, rice husk ash had the largest effect on ecosystem damage, with an 11.9% increase observed when its content was increased.

3.2.6. Ceramic and EAF slag concrete

According to Fig. 10, a 25% increase in ceramic waste led to a 12.2% rise in human health damage. Cement again drove increases in both climate change and ecosystem categories, while electricity variation significantly affected resource consumption.

3.2.7. Cross-verification of results using BEES and IPCC methods

To ensure the validity and robustness of the environmental impact results, the findings from the CML 2001 and IMPACT 2002+ methods were cross-verified using two supplementary approaches: BEES (Building for Environmental and Economic Sustainability) and the IPCC method for GWP. These additional methods were selected due to their widespread use and methodological distinctions,

which allow for independent validation of key results.

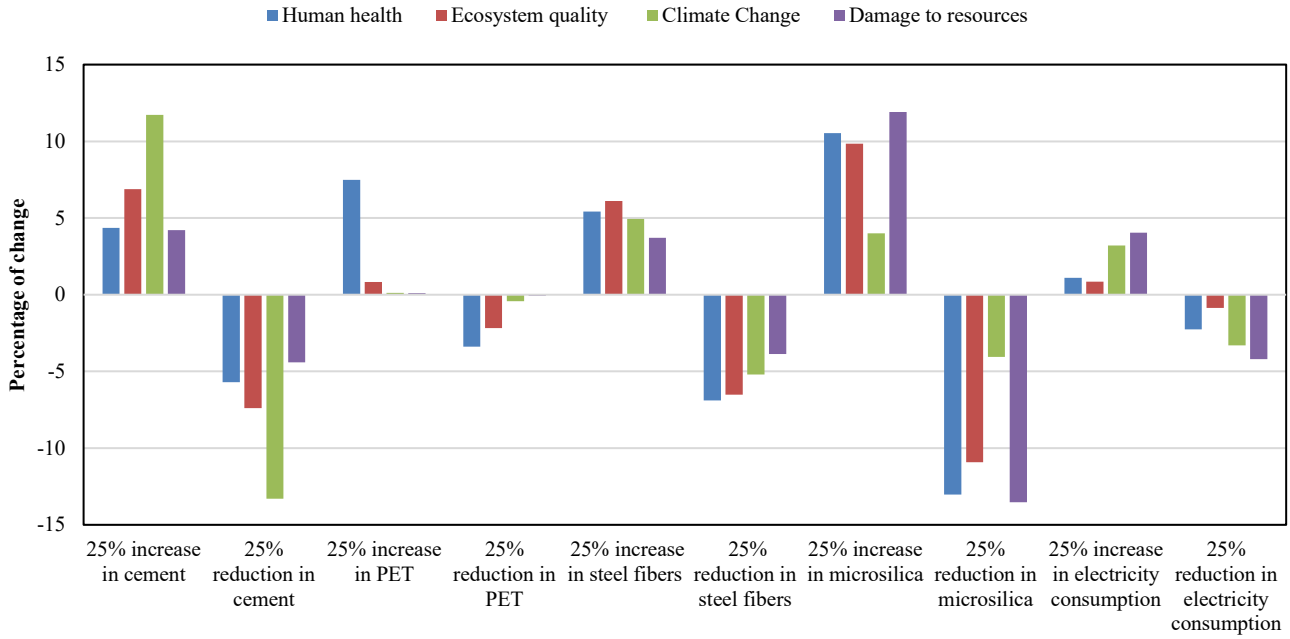

Fig. 7. Sensitivity analysis of PET and fiber-reinforced concrete under ±25% input variation using the IMPACT 2002+ method.

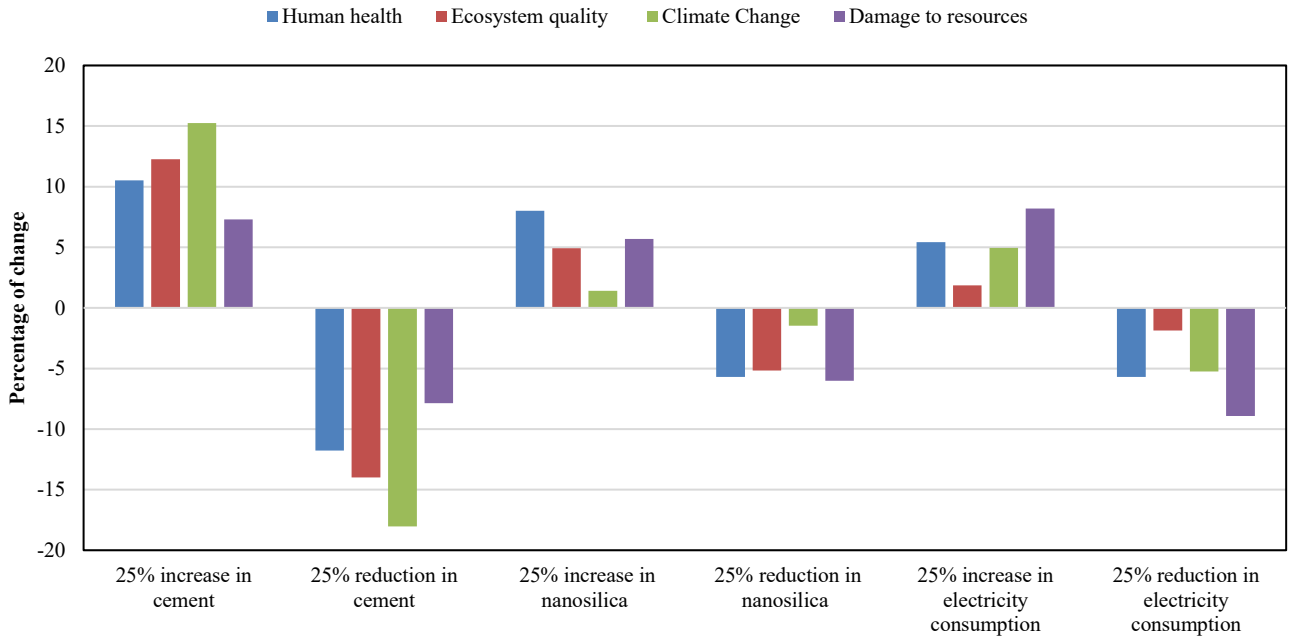

Fig. 8. Sensitivity analysis of nano-silica concrete under ±25% input variation using the IMPACT 2002+ method.

Tables 6 and 9 present the environmental impact results of five concrete types across acidification, eutrophication, global warming potential, and human toxicity. Among them, micro-silica concrete exhibited the highest impact in all categories, particularly in acidification and human toxicity.

Table 7 presents a comparison of global warming potential values derived from the CML 2001 and IMPACT 2002+ methods against those obtained from the BEES model. The results show a high level of agreement across all concrete types, with percentage differences generally below 5%. The largest deviation was observed for the asbestos and rice husk ash concrete mix, at 7.43%. Despite differences in modeling assumptions and units of measurement, the close alignment across methods confirms the reliability and robustness of the life cycle assessment results and indicates that the relative environmental ranking of the concrete mixes is not significantly influenced by the choice of assessment model.

Further validation was performed using the IPCC method, which focuses on climate-related emissions. As shown in Table 8, global warming results from CML 2001 and IPCC show excellent agreement with differences ranging from 0.04% to 0.20%. This confirms the robustness of the findings and indicates that the results are not sensitive to the choice of impact assessment model. These outcomes are consistent with prior research by Asadollahfardi et al. [19], who also reported minimal variation across methods

when evaluating the environmental impacts of different concrete types.

Overall, these comparisons further confirm that methodological differences between IPCC and CML-IA have minimal impact on the outcome, supporting the robustness and consistency of the LCA results across evaluation methods.

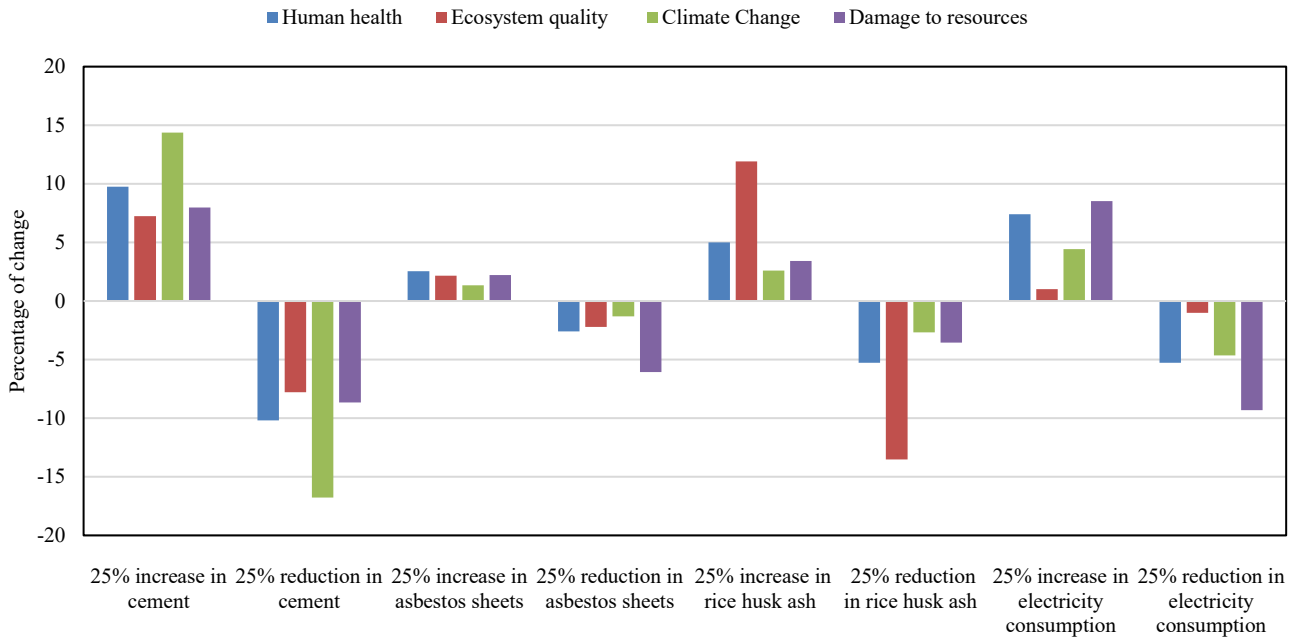

Fig. 9. Sensitivity analysis of asbestos and rice husk ash concrete under ±25% input variation using the IMPACT 2002+ method.

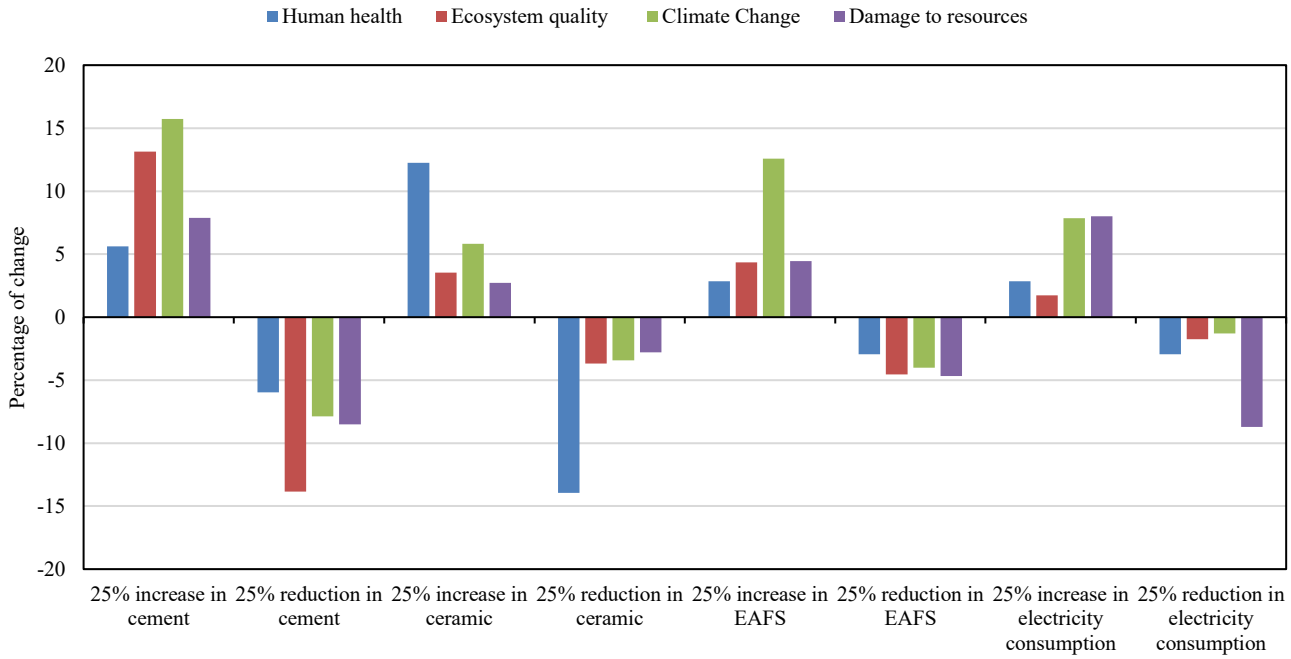

Fig. 10. Sensitivity analysis of ceramic and EAFS concrete under ±25% variation in inputs using the IMPACT 2002+ method.

Table 6. Global warming potential of six concretes: CML 2001 vs. BEES (with % difference).

Concrete type	Global warming for IMPACT (kg CO_2 eq)	Global warming for BEES (g CO_2 eq)	Difference (%)
Conventional concrete	564.66	559251.34	0.96
Pumice concrete	736.64	720658.20	2.19
PET and fiber concrete	939.32	918354.18	2.26
Nano-silica concrete	586.09	578172.58	1.36
Ceramic and arc slag concrete	898.06	891765.86	0.78
Asbestos and rice husk ash concrete	706.56	684874.99	3.12

Table 9 presents the environmental impact results of five concrete types across acidification, eutrophication, global warming potential, and human toxicity. Among them, micro-silica concrete exhibited the highest impact in all categories, particularly in acidification and human toxicity.

Table 7. Global warming potential of six concretes: IMPACT 2002+ vs. BEES (with % difference).

Concrete type	Global warming for IMPACT (kg CO_2 eq)	Global warming for BEES (g CO_2 eq)	Difference(%)
Conventional concrete	553.6	559251.36	1.08
Pumice concrete	696.6	720658.44	3.33
PET and fiber concrete	888.9	918354.18	3.22
Nano-silica concrete	605.8	578172.38	4.61
Ceramic and arc slag concrete	882.2	891764.56	0.85
Asbestos and rice husk ash concrete	635.8	684874.35	7.43

Table 8. Comparison of global warming potential for six concrete types using CML 2001 and IPCC methods (% difference).

Concrete type	Global warming for CML (kg CO_2 eq)	Global warming for IPCC (g CO_2 eq)	Difference(%)
Conventional concrete	564.6	564.89	0.04
Pumice concrete	736.6	737.62	0.13
PET and fiber concrete	939.3	940.58	0.13
Nano-silica concrete	586.09	586.5	0.07
Ceramic and arc slag concrete	898.72	899.04	0.07
Asbestos and rice husk ash concrete	706.56	707.99	0.20

Table 9. Environmental impact indicators for five concrete types (acidification, eutrophication, GWP, human toxicity).

Concrete type	Acidification (kg SO_2 eq)	Eutrophication (kg PO_4^{3-} eq)	Global warming potential (kg CO_2 eq)	Human toxicity (kg 1.4-DB eq)
Concrete with ordinary Portland cement	0.84	0.159	386.44	35.68
Microsilica	1.55	0.572	605.32	182.52
Geopolymer	1.11	0.183	286.85	72.35
Micro-nano bubbles	0.89	0.175	424.17	37.45
Nanosilica	0.96	0.185	453.31	41.04

In Table 10, global warming potential values obtained from the IPCC and CML-IA (World 2000) methods were compared. The results show negligible differences for most concrete types-just 0.6% for ordinary Portland cement, nano-silica, and micro-nanobubble concretes. Slightly higher differences were observed for geopolymer (0.9%) and micro-silica (2.4%) concretes.

Table 10. CML-IA vs. IPCC: Global warming potential for five concretes (% difference).

Concrete type	Global warming for CML (kg CO_2 eq)	Global warming for IPCC (kg CO_2 eq)	Difference(%)
Concrete with ordinary Portland cement	388.84	386.44	0.6
Microsilica	619.73	605.32	2.4
Geopolymer	289.54	286.85	0.9
Micro-nano bubbles	426.72	424.17	0.6
Nanosilica	456.08	453.31	0.8

3.3. Economic analysis of concrete mixes

To complement the environmental analysis, an economic assessment was conducted using life cycle costing based on current Iranian market prices for raw materials. The cost per cubic meter of each concrete type was calculated from material quantities and unit prices (Table 11).

The estimated costs are as follows:

- Conventional Concrete: 9,854,800 IRR
- Pumice Concrete: 11,999,646 IRR
- PET & Fiber Concrete: 20,446,668 IRR
- Nano-silica Concrete: 242,695,148 IRR

- Ceramic & EAFS Concrete: 34,386,450 IRR
- Asbestos & Rice Husk Ash Concrete: 104,029,586 IRR

Table 11. Unit prices of raw materials used in concrete mix designs (based on the Iranian market).

Raw materials used	Unit	Price (I.R Rial)	Raw materials used	Unit	Price (I.R Rial)
Cement	kg	13600	Pumice	kg	2830
Sand	kg	2200	Ceramics	kg	22500
Sand	kg	2200	Electric arc furnace slag	kg	56170
PET waste	kg	185400	Asbestos cement sheets	kg	87270
Steel fibers	kg	520000	Rice hull ash	kg	800000
Microsilica	kg	54000	Lubricant	L	952570
Nanosilica	kg	9000000	-	-	-

Conventional concrete is the most cost-effective option, mainly due to its reliance on widely available and low-cost materials. In contrast, nano-silica concrete has the highest cost, driven by the high price of nanosilica and other specialized additives like microsilica and steel fibers. Other mixes, such as those containing rice husk ash, asbestos sheets, ceramics, and slag, also show elevated costs due to the expensive or limited availability of their components. While these alternatives may offer environmental or performance benefits, their high economic cost can limit practical application, highlighting the trade-off between sustainability and affordability in material selection.

3.4. Integrated environmental–economic evaluation

Given the critical role of both environmental and economic factors in material selection, an integrated assessment was performed to support more informed decision-making. As shown in Fig. 11, conventional concrete emerges as the most balanced option, offering both the lowest production cost and GWP. Nano-silica concrete demonstrates relatively low CO_2 emissions, suggesting environmental benefits; however, its extremely high cost significantly reduces its economic attractiveness. On the other hand, PET fiber-reinforced concrete, while economically moderate, exhibits the highest GWP, making it environmentally less favorable. Alternatives such as pumice concrete and EAFS-ceramic concrete offer more balanced profiles with moderate emissions and reasonable costs. These findings emphasize the importance of evaluating both impact categories jointly, as no single concrete mix optimizes all performance criteria simultaneously.

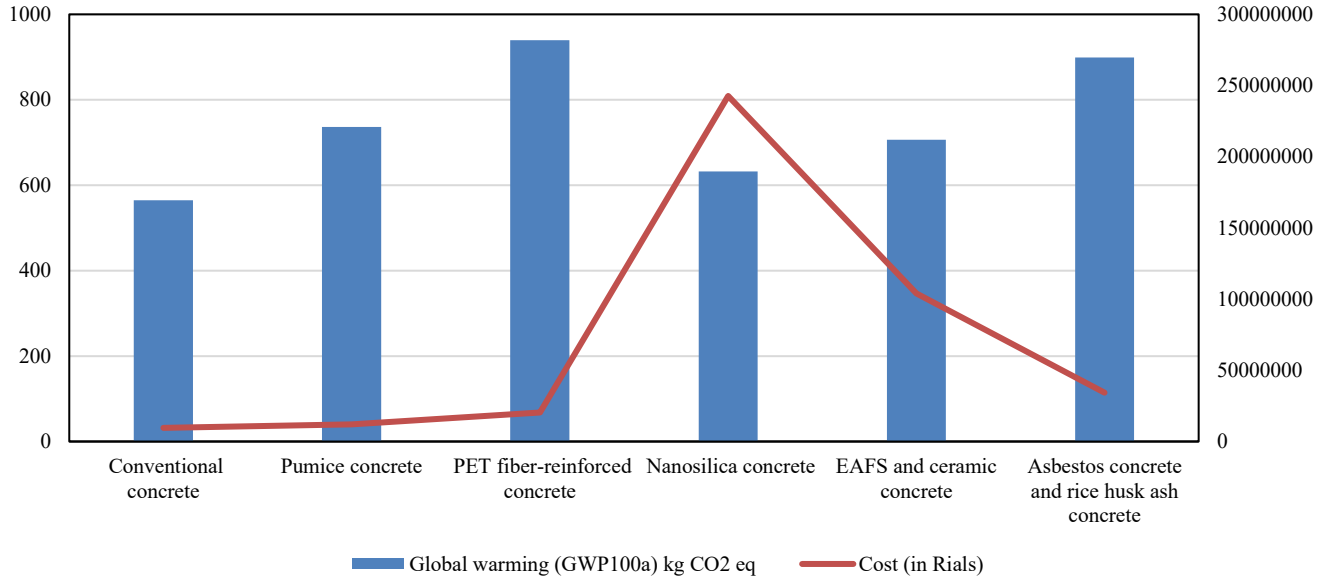

Fig. 11. Economic and environmental assessment of CO2 emissions based on the CML method.

3.5. Research limitations

A key limitation of this study is that some of the proposed concrete mix designs were not implemented at full scale in real-world construction, limiting the availability of accurate performance data, particularly regarding service life. As a result, a cradle-to-gate system boundary was adopted, focusing exclusively on the environmental impacts associated with raw material extraction, processing, and concrete production. Additionally, due to limited transparency and restricted access to emission data from domestic manufacturing facilities in Iran, the life cycle assessment relied on European and international datasets and standards. While this approach provides a consistent methodological framework, it may not fully capture region-specific variations in environmental performance.

4. Conclusion

This study assessed the environmental and economic performance of six concrete mixtures using LCA and cost analysis. The results consistently identified conventional concrete as the most environmentally and economically favorable option. It showed the lowest impacts across key categories such as global warming, human toxicity, ecotoxicity, and acidification, as confirmed by the CML, IMPACT 2002+, and ReCiPe methods.

Among the alternative mixes, PET/steel fiber concrete exhibited the highest environmental burden-particularly in terms of CO_2 emissions and human health impacts-despite being relatively cost-effective. In contrast, nano-silica concrete, though environmentally competitive, was economically impractical due to the high cost of its components. Cement was found to be the most influential contributor to environmental damage across all mixes, with a 25% increase in content-raising impacts by up to 16%. Microsilica also showed notable influence, particularly in the PET and pumice-based mixes. The integrated analysis demonstrated that no single mix optimized all performance aspects. However, pumice concrete and ceramic/EAFS concrete provided moderate emissions with acceptable costs, offering more balanced alternatives. Ultimately, the findings highlight the trade-offs between environmental benefits and economic feasibility, emphasizing the need for context-specific mix selection in sustainable construction.

Statements & declarations

Author Contributions

Mohammad-Amin Dashab: Conceptualization, Investigation, Methodology, Formal analysis, Resources, Writing - Original Draft, Writing - Review & Editing.

Mostafa Kazemi: Conceptualization, Methodology, Project administration, Supervision, Writing - Review & Editing.

Funding

The authors received no financial support for the research, authorship, and/or publication of this article.

Declarations

The authors declare no conflict of interest.

Data availability

The data presented in this study will be available on interested request from the corresponding author

References

[1] Vieira, T., Alves, A., de Brito, J., Correia, J. R., Silva, R. V. Durability-Related Performance of Concrete Containing Fine Recycled Aggregates from Crushed Bricks and Sanitary Ware. Materials and Design, 2016; 90: 767–776. doi:10.1016/j.matdes.2015.11.023.

[2] Meyer, C. The Greening of the Concrete Industry. Cement and Concrete Composites, 2009; 31 (8): 601–605. doi:10.1016/j.cemconcomp.2008.12.010.

[3] Ding, G. K. C. Sustainable Construction-The Role of Environmental Assessment Tools. Journal of Environmental Management, 2008; 86 (3): 451–464. doi:10.1016/j.jenvman.2006.12.025.

[4] Lee, K. M., Inaba, A. Life cycle assessment: best practices of ISO 14040 series. Suwon (KR): Center for Ecodesign and LCA (CEL), Ajou University; 2004.

[5] Klöpffer, W. Background and future prospects in life cycle assessment. Dordrecht (NL): Springer Science & Business Media; 2014. Vol. 53. doi:10.1007/978-94-017-8697-3.

[6] Rebitzer, G., Ekvall, T., Frischknecht, R., Hunkeler, D., Norris, G., Rydberg, T., Schmidt, W.-P., Suh, S., Weidema, B. P., Pennington, D. W. Life Cycle Assessment: Part 1: Framework, Goal and Scope Definition, Inventory Analysis, and Applications. Environment international, 2004; 30 (5): 701–720. doi:10.1016/j.envint.2003.11.005.

[7] Bayer, C., Gamble, M., Gentry, R., Joshi, S. AIA guide to building life cycle assessment in practice. Washington (DC): The American Institute of Architects; 2010. Report No.: 16. p. 17–60.

[8] International Organization for Standardization (ISO). ISO 14044:2006: Environmental management – Life cycle assessment – Requirements and guidelines. Geneva (CH): ISO; 2006.

[9] Tafheem, Z., Khusru, S., Nasrin, S. Environmental impact of green concrete in practice. In: Proceedings of the International Conference on Mechanical Engineering and Renewable Energy; 2011 Dec 22–24; Chittagong, Bangladesh.

[10] Jahren, P., Sui, T. Concrete and sustainability. Boca Raton (FL): CRC Press; 2013. doi:10.1201/b15160.

[11] Shetty, M. S. Concrete technology: theory & practice. New Delhi (IN): S. Chand & Company Ltd.; 2005.

[12] Janamian, K., Aguiar, J. B. Concrete materials and technology: a practical guide. Boca Raton (FL): CRC Press; 2023.

doi:10.1201/9781003384243.

[13] Gambhir, M. L. Concrete technology: theory and practice. New Delhi (IN): McGraw-Hill Education (India); 2013.

[14] del Rey Castillo, E., Almesfer, N., Saggi, O., Ingham, J. M. Light-Weight Concrete with Artificial Aggregate Manufactured from Plastic Waste. Construction and Building Materials, 2020; 265: 120199. doi:10.1016/j.conbuildmat.2020.120199.

[15] George GK, Revathi P. Production and utilisation of artificial coarse aggregate in concrete – a review. IOP Conference Series: Materials Science and Engineering. 2020;936(1):012035. doi:10.1088/1757-899X/936/1/012035.

[16] Tokyay, M. Cement and concrete mineral admixtures. Boca Raton (FL): CRC Press; 2016. doi:10.1201/b20093.

[17] Colangelo, F., Forcina, A., Farina, I., Petrillo, A. Life Cycle Assessment (LCA) of Different Kinds of Concrete Containing Waste for Sustainable Construction. Buildings, 2018; 8 (5): 70. doi:10.3390/buildings8050070.

[18] Demirel, S., Öz, H. Ö., Güneş, M., Çiner, F., Adın, S. Life-Cycle Assessment (LCA) Aspects and Strength Characteristics of Self-Compacting Mortars (SCMs) Incorporating Fly Ash and Waste Glass PET. International Journal of Life Cycle Assessment, 2019; 24 (6): 1139–1153. doi:10.1007/s11367-018-1562-5.

[19] Asadollahfardi, G., Katebi, A., Taherian, P., Panahandeh, A. Environmental Life Cycle Assessment of Concrete with Different Mixed Designs. International Journal of Construction Management, 2021; 21 (7): 665–676. doi:10.1080/15623599.2019.1579015.

[20] Bellil, A., Aziz, A., El Amrani El Hassani, I. I., Achab, M., El Haddar, A., Benzaouak, A. Producing of Lightweight Concrete from Two Varieties of Natural Pozzolan from the Middle Atlas (Morocco): Economic, Ecological, and Social Implications. Silicon, 2022; 14 (8): 4237–4248. doi:10.1007/s12633-021-01155-8.

[21] Ersan, Y. C., Gulcimen, S., Imis, T. N., Saygin, O., Uzal, N. Life Cycle Assessment of Lightweight Concrete Containing Recycled Plastics and Fly Ash. European Journal of Environmental and Civil Engineering, 2022; 26 (7): 2722–2735. doi:10.1080/19648189.2020.1767216.

[22] Shahmansouri, A. A., Akbarzadeh Bengar, H., AzariJafari, H. Life Cycle Assessment of Eco-Friendly Concrete Mixtures Incorporating Natural Zeolite in Sulfate-Aggressive Environment. Construction and Building Materials, 2021; 268: 121136. doi:10.1016/j.conbuildmat.2020.121136.

[23] Napolano, L., Menna, C., Graziano, S. F., Asprone, D., D'Amore, M., De Gennaro, R., Dondi, M. Environmental Life Cycle Assessment of Lightweight Concrete to Support Recycled Materials Selection for Sustainable Design. Construction and Building Materials, 2016; 119: 370–384. doi:10.1016/j.conbuildmat.2016.05.042.

[24] Valipour, M., Yekkalar, M., Shekarchi, M., Panahi, S. Environmental Assessment of Green Concrete Containing Natural Zeolite on the Global Warming Index in Marine Environments. Journal of Cleaner Production, 2014; 65: 418–423. doi:10.1016/j.jclepro.2013.07.055.

[25] Nath, P., Sarker, P. K., Biswas, W. K. Effect of Fly Ash on the Service Life, Carbon Footprint and Embodied Energy of High Strength Concrete in the Marine Environment. Energy and Buildings, 2018; 158: 1694–1702. doi:10.1016/j.enbuild.2017.12.011.

[26] International Organization for Standardization (ISO). ISO 14040:2006: Environmental management – Life cycle assessment – Principles and framework. Geneva (CH): International Organization for Standardization; 2006.

[27] Turner, L. K., Collins, F. G. Carbon Dioxide Equivalent (CO2-e) Emissions: A Comparison between Geopolymer and OPC Cement Concrete. Construction and Building Materials, 2013; 43: 125–130. doi:10.1016/j.conbuildmat.2013.01.023.

[28] Vázquez-Calle, K., Guillén-Mena, V., Quesada-Molina, F. Analysis of the Embodied Energy and CO2 Emissions of Ready-Mixed Concrete: A Case Study in Cuenca, Ecuador. Materials, 2022; 15 (14): 4896. doi:10.3390/ma15144896.

[29] Goedkoop M, Oele M, Leijting J, Ponsioen T, Meijer E. Introduction to LCA with SimaPro. Amersfoort (NL): PRé Consultants; 2016.

Appendix

Table A- 1. LCA input data for conventional concrete in SimaPro, including materials, transport, energy, and CO_2 emissions.

Input process	Unit	Amount	Raw materials, process and emission
Cement, Portland {RoW}| market for | APOS, U	kg	430	Portland cement
Tap water {RoW}| market for | APOS, U	L	215	Water
Gravel, crushed {RoW}| market for gravel, crushed | APOS, U	kg	845	Gravel
Sand {RoW}| gravel and quarry operation | APOS, U	kg	855	Sand
Packing, cement {RoW}| processing | APOS, U	kg	430	Cement packaging
Transport, freight, lorry 16-32 metric ton, EURO4 {RoW}| transport, freight, lorry 16-32 metric ton, EURO4 | APOS, U	tkm	30.1	Cement transportation
Transport, freight, lorry 16-32 metric ton, EURO4 {RoW}| transport, freight, lorry 16-32 metric ton, EURO4 | APOS, U	tkm	59.1	Gravel transportation
Transport, freight, lorry 16-32 metric ton, EURO4 {RoW}| transport, freight, lorry 16-32 metric ton, EURO4 | APOS, U	tkm	59.8	Sand transportation
Electricity, medium voltage | market for | APOS, U	KWh	157.9	Concrete production energy

Carbon dioxide	kg	0.0033	Factory carbon dioxide emissions
Carbon dioxide	kg	0.0094	Carbon dioxide emissions from workshop activities for concrete production

Table A- 2. LCA input data for pumice aggregate in SimaPro, including materials, transport, energy, and CO_2 emissions .

Input process	Unit	Amount	Raw materials, process and emission
Cement, Portland {RoW}| market for | APOS, U	kg	468.3	Portland cement
Tap water {RoW}| market for | APOS, U	L	126.7	Water
Pumice {GLO}| market for | APOS, U	kg	200.7	Pumice
Sand {RoW}| gravel and quarry operation | APOS, U	kg	784.5	Sand
Ferrosilicon {GLO}| market for | APOS, U	kg	46.8	Microsilica
Plasticiser, for concrete, based on sulfonated melamine formaldehyde {GLO}| market for | APOS, U	kg	0.85	Lubricant
Packing, cement {RoW}| processing | APOS, U	kg	468.3	Cement batching
Transport, freight, lorry 16-32 metric ton, EURO4 {RoW}| transport, freight, lorry 16-32 metric ton, EURO4 | APOS, U	tkm	32.8	Cement transportation
Transport, freight, lorry 16-32 metric ton, EURO4 {RoW}| transport, freight, lorry 16-32 metric ton, EURO4 | APOS, U	tkm	14.0	Pumice transportation
Transport, freight, lorry 16-32 metric ton, EURO4 {RoW}| transport, freight, lorry 16-32 metric ton, EURO4 | APOS, U	tkm	54.9	Sand transportation
Transport, freight, lorry 16-32 metric ton, EURO4 {RoW}| transport, freight, lorry 16-32 metric ton, EURO4 | APOS, U	tkm	3.3	Microsilica transportation
Transport, freight, lorry 16-32 metric ton, EURO4 {RoW}| transport, freight, lorry 16-32 metric ton, EURO4 | APOS, U	tkm	0.06	Pumice transportation
Electricity, medium voltage {IR}| market for | APOS, U	KWh	157.9	Concrete production energy
Carbon dioxide	kg	0.0033	Factory carbon dioxide emissions
Carbon dioxide	kg	0.0094	Carbon dioxide emissions from workshop activities for concrete production

Table A- 3. LCA input data for PET and steel fibers in SimaPro, including materials, transport, energy, and CO_2 emissions.

Input process	Unit	Amount	Raw materials, process and emission
Cement, Portland {RoW}| market for | APOS, U	kg	477	Portland cement
Tap water {RoW}| market for | APOS, U	L	157	Water
Gravel, crushed {RoW}| market for gravel, crushed | APOS, U	kg	1.04	Gravel
Sand {RoW}| gravel and quarry operation | APOS, U	kg	95	Sand
Ferrosilicon {GLO}| market for | APOS, U	kg	53	Microsilica
Waste polyethylene terephthalate, for recycling, sorted {RoW}| market for waste polyethylene terephthalate, for recycling, sorted | APOS, U	kg	36.7	PET waste
Steel fibers	kg	78.5	Steel fibers
Packing, cement {RoW}| processing | APOS, U	kg	477	Cement packaging
Transport, freight, lorry 16-32 metric ton, EURO4 {RoW}| transport, freight, lorry 16-32 metric ton, EURO4 | APOS, U	tkm	33.4	Cement transportation
Transport, freight, lorry 16-32 metric ton, EURO4 {RoW}| transport, freight, lorry 16-32 metric ton, EURO4 | APOS, U	tkm	0.07	Gravel transportation
Transport, freight, lorry 16-32 metric ton, EURO4 {RoW}| transport, freight, lorry 16-32 metric ton, EURO4 | APOS, U	tkm	6.6	Sand transportation
Transport, freight, lorry 16-32 metric ton, EURO4 {RoW}| transport, freight, lorry 16-32 metric ton, EURO4 | APOS, U	tkm	3.7	Microsilica transport
Transport, freight, lorry 16-32 metric ton, EURO4 {RoW}| transport, freight, lorry 16-32 metric ton, EURO4 | APOS, U	tkm	2.6	PET waste transportation
Transport, freight, lorry 16-32 metric ton, EURO4 {RoW}| transport, freight, lorry 16-32 metric ton, EURO4 | APOS, U	tkm	5.5	Steel fiber transportation
Electricity, medium voltage {IR}| market for | APOS, U	KWh	157.9	Concrete production energy
Carbon dioxide	kg	0.0033	Factory carbon dioxide emissions
Carbon dioxide	kg	0.0094	Carbon dioxide emissions from workshop activities for concrete production

Table A- 4. LCA input data for nanosilica pozzolan in SimaPro, including materials, transport, energy, and CO_2 emissions.

Input process	Unit	Amount	Raw materials, process and emission
Cement, Portland {RoW}| market for | APOS, U	kg	404.2	Portland cement

Tap water {RoW}| market for | APOS, U	L	215	Water
Gravel, crushed {RoW}| market for gravel, crushed | APOS, U	kg	855.5	Gravel
RC Sand	kg	793.1	Recycled sand
Nanosilica	kg	25.8	Nano-silica
Plasticiser, for concrete, based on sulfonated melamine formaldehyde {GLO}| market for | APOS, U	kg	0.4	Lubricant
Packing, cement {RoW}| processing | APOS, U	kg	404.2	Cement packaging
Transport, freight, lorry 16-32 metric ton, EURO4 {RoW}| transport, freight, lorry 16-32 metric ton, EURO4 | APOS, U	tkm	28.3	Cement transportation
Transport, freight, lorry 16-32 metric ton, EURO4 {RoW}| transport, freight, lorry 16-32 metric ton, EURO4 | APOS, U	tkm	599	Gravel transportation
Transport, freight, lorry 16-32 metric ton, EURO4 {RoW}| transport, freight, lorry 16-32 metric ton, EURO4 | APOS, U	tkm	55.5	Transportation of recycled sand
Transport, freight, lorry 16-32 metric ton, EURO4 {RoW}| transport, freight, lorry 16-32 metric ton, EURO4 | APOS, U	tkm	1.8	Nano-Silica Transportation
Transport, freight, lorry 16-32 metric ton, EURO4 {RoW}| transport, freight, lorry 16-32 metric ton, EURO4 | APOS, U	tkm	0.03	Lubricant transportation
Electricity, medium voltage {IR}| market for | APOS, U	KWh	157.9	Concrete production energy
Carbon dioxide	kg	0.0033	Factory carbon dioxide emissions
Carbon dioxide	kg	0.0094	Carbon dioxide emissions from workshop activities for concrete production

Table A- 5. LCA input data for ceramic waste and EAFS in SimaPro, including materials, transport, energy, and CO_2 emissions.

Input process	Unit	Amount	Raw materials, process and emission
Cement, Portland {RoW}| market for | APOS, U	kg	448	Portland cement
Tap water {RoW}| market for | APOS, U	L	215	Water
Gravel, crushed {RoW}| market for gravel, crushed | APOS, U	kg	445	Gravel
Sand {RoW}| gravel and quarry operation | APOS, U	kg	275	Sand
Ceramic tile {GLO}| market for | APOS, U	kg	52	Ceramic
Electric arc furnace slag	kg	445	EAFS
Packing, cement {RoW}| processing | APOS, U	kg	448	Cement packaging
Transport, freight, lorry 16-32 metric ton, EURO4 {RoW}| transport, freight, lorry 16-32 metric ton, EURO4 | APOS, U	tkm	31.4	Cement transportation
Transport, freight, lorry 16-32 metric ton, EURO4 {RoW}| transport, freight, lorry 16-32 metric ton, EURO4 | APOS, U	tkm	31.1	Gravel transportation
Transport, freight, lorry 16-32 metric ton, EURO4 {RoW}| transport, freight, lorry 16-32 metric ton, EURO4 | APOS, U	tkm	19.2	Sand transportation
Transport, freight, lorry 16-32 metric ton, EURO4 {RoW}| transport, freight, lorry 16-32 metric ton, EURO4 | APOS, U	tkm	3.6	Ceramic transportation
Transport, freight, lorry 16-32 metric ton, EURO4 {RoW}| transport, freight, lorry 16-32 metric ton, EURO4 | APOS, U	tkm	31.1	EAFS transportation
Electricity, medium voltage {IR}| market for | APOS, U	KWh	157.9	Concrete production energy
Carbon dioxide	kg	0.0033	Factory carbon dioxide emissions
Carbon dioxide	kg	0.0094	Carbon dioxide emissions from workshop activities for concrete production

Table A- 6. LCA input data for asbestos cement corrugated sheets and rice husk ash waste in SimaPro, including materials, transport, energy, and CO_2 emissions.

Input process	Unit	Amount	Raw materials, process and emission
Cement, Portland {RoW}| market for | APOS, U	kg	425	Portland cement
Tap water {RoW}| market for | APOS, U	L	215	Water
Gravel, crushed {RoW}| market for gravel, crushed | APOS, U	kg	522	Gravel
Sand {RoW}| gravel and quarry operation | APOS, U	kg	570.2	Sand
Asbestos, crysotile type {GLO}| market for | APOS, U	kg	387.2	Asbestos cement sheet
Rice husk ash (RHS)	kg	75	Rice husk ash
Plasticiser, for concrete, based on sulfonated melamine formaldehyde {GLO}| market for | APOS, U	kg	2.1	Lubricant
Packing, cement {RoW}| processing | APOS, U	kg	425	Cement packaging

Transport, freight, lorry 16-32 metric ton, EURO4 {RoW}| transport, freight, lorry 16-32 metric ton, EURO4 | APOS, U	tkm	29.7	Cement transportation
Transport, freight, lorry 16-32 metric ton, EURO4 {RoW}| transport, freight, lorry 16-32 metric ton, EURO4 | APOS, U	tkm	36.5	Gravel transportation
Transport, freight, lorry 16-32 metric ton, EURO4 {RoW}| transport, freight, lorry 16-32 metric ton, EURO4 | APOS, U	tkm	39.9	Sand transportation
Transport, freight, lorry 16-32 metric ton, EURO4 {RoW}| transport, freight, lorry 16-32 metric ton, EURO4 | APOS, U	tkm	27.2	Asbestos cement sheet transportation
Transport, freight, lorry 16-32 metric ton, EURO4 {RoW}| transport, freight, lorry 16-32 metric ton, EURO4 | APOS, U	tkm	5.2	Rice husk ash transportation
Electricity, medium voltage {IR}| market for | APOS, U	KWh	157.9	Concrete production energy
Carbon dioxide	kg	0.0033	Factory carbon dioxide emissions
Carbon dioxide	kg	0.0094	Carbon dioxide emissions from workshop activities for concrete production

Civil Engineering and Applied Solutions

Research Article

journal homepage: ceas.journals.umz.ac.ir

CEAS Civil Engineering and Applied Solutions

Assessment of the Impact of Land Use/Land Cover Changes in the Hamoun Wetland on Land Surface Temperature Using Satellite Imagery

Mozhgan Yarahmadi [a], Hadi Eskandari Damaneh [b], Shahram Khalighi Sigaroodi [a*]

[a] *Department of Arid and Mountainous Regions Reclamation, Faculty of Natural Resources, University of Tehran, Iran*

[b] *Department of Desert Studies, Research Institute of Forests and Rangelands, Agricultural Research, Education and Extension Organization (AREEO), Tehran, Iran*

ARTICLE INFO

Keywords:
Land use/land cover (LULC) changes
Temperature
Palmer drought severity index (PDSI)
Hamoun

Article history:
Received 7 May 2025
Accepted 26 May 2025
Available online 01 July 2025

ABSTRACT

The Hamoun wetland, situated in southeastern Iran near the Afghanistan border, is a sensitive ecological and socio-economic area that has undergone significant land use and environmental changes over recent decades. This study applied the supervised CART classification method to identify Land Use/Land Cover (LULC) changes over 40 years (corresponding to 1990, 2000, 2010, and 2020) in the Hamoun region. Surface temperature data were analyzed regarding land use changes, and the Palmer Drought Severity Index (PDSI) was utilized to assess drought trends during this time. The results indicate a significant decline in water bodies, agricultural lands, and reed beds. Specifically, the water bodies decreased from 11.25% in 1990 to 2.47% in 2020, agricultural lands from 8.56% to 3.53%, and reed beds from 4.64% to 0.38%. Conversely, low-vegetation areas, barren lands, and urban areas expanded, with barren lands increasing by 14.05%. The overall classification accuracy for the LULC maps was approximately 96%, 96%, 95%, and 98% for the respective years, and the Kappa coefficients were 0.97, 0.97, 0.96, and 0.98, indicating high classification accuracy. Temperature trends declined during the study period, primarily due to severe droughts. The findings highlight a significant relationship between land use changes and surface temperature variations. This research provides valuable insights for policymakers and urban planners, supporting sustainable LULC strategies at the local level.

1. Introduction

Land Use and Land Cover (LULC) changes play a significant role in global and regional climate pattern alterations, including rainfall variability and increases in Land Surface Temperature (LST) [1-4]. Human activities have extensively modified land surface utilization over the past centuries, significantly impacting terrestrial ecosystems and, consequently, the environment [5]. Rapid urbanization and population growth in urban centers are among the primary drivers of land use change. One of the major environmental issues observed across various regions is the rise in LST in response to land use transformations. LST is a critical variable that can be accurately measured using thermal infrared bands with high spatial resolution [6-9]. Therefore, identifying current LULC changes is essential for assessing variations in land surface temperature.

Zhao et al. [10] investigated changes in land use and LULC, land surface temperature (LST), the Normalized Difference Vegetation Index (NDVI), and the Normalized Difference Built-up Index (NDBI) in the Kasur region over three decades. Their findings revealed an expansion of urban areas and a decline in vegetation, water bodies, forests, and barren land, with a negative correlation between NDVI and NDBI. Similarly, Saleem et al. [11] examined LULC changes in the Jammu region of India between

* Corresponding author.
E-mail addresses: Khalighi@ut.ac.ir (S. Khalighi Sigaroodi).

https:// doi.org/10.22080/ceas.2025.29153.1009
ISSN: 3092-7749/© 2025 The Author(s). Published by University of Mazandaran.
This article is an open access article distributed under the terms and conditions of the Creative Commons Attribution (CC-BY) license (https://creativecommons.org/licenses/by/4.0/deed.en)
How to cite this article: Yarahmadi, M., Eskandari Damaneh, H., Khalighi Sigaroodi, S. Assessment of the impact of land use/land cover changes in the Hamoun Wetland on land surface temperature using satellite imagery. Civil Engineering and Applied Solutions. 2025; 1(2): 31–42. doi:10.22080/ceas.2025.29153.1009.

1990 and 2020 using remote sensing data, indicating increased agricultural, barren, and settlement areas alongside vegetation loss and rising LST due to climate change. NDVI was highlighted as an effective indicator of vegetation health and its impact on surface temperature. Hussainet al. [12] analyzed LULC changes and their effect on LST in Khanewal, Pakistan, using remote sensing techniques. Their results demonstrated that the rapid expansion of built-up areas led to vegetation decline and temperature rise, primarily driven by population growth, urban development, and infrastructure expansion—findings that are valuable for regional planning and agricultural management. Moreover, Al Rakib et al. [13] studied the effects of rapid urban growth on LULC and LST in Mymensingh, Bangladesh. Their study found that urban expansion over the past two decades resulted in a loss of vegetation and water resources and an increase in surface temperature by approximately 8°C. Gohainet al. [14] evaluated LULC and LST variations in Pune city from 1990 to 2019, concluding that rapid urban development contributed to increased summer temperatures and decreased winter temperatures. These findings are instrumental for urban planners in making informed decisions. In addition, Tan et al. [15] investigated LULC changes in the Dongting Lake region of China, showing that economic development-induced land changes led to increased LST; built-up areas had higher surface temperatures than water bodies and forests, and the reduction of water surfaces, following the construction of the Three Gorges Dam, led to a 3.5°C increase in winter temperatures.

Remote sensing (RS) techniques have been widely used to assess changes in land use/land cover (LULC) and land surface temperature (LST) in recent years through Landsat imagery [16]. RS offers several advantages, including accessibility to remote areas, provision of otherwise unattainable data, cost-effectiveness, and reduced need for fieldwork. Therefore, many researchers have utilized Landsat and MODIS data to estimate annual changes in LULC and LST. In contrast, traditional field-based studies are time-consuming, expensive, and often unsuitable for large-scale assessments [17]. LST variations are influenced by factors such as changes in land use, seasonal rainfall, climatic conditions, and socio-economic developments [18]. Alterations in land cover patterns are mainly driven by human activities [19], including wildfires [20] and deforestation [21], which contribute to global warming and soil erosion. Geostationary satellites, with their capability to provide data every 30 minutes, offer a unique resource for monitoring daily Earth surface changes.

The Hamoun wetland, situated in southeastern Iran near the border with Afghanistan, is of high ecological and socioeconomic importance. Due to frequent droughts, upstream water management, and land use pressures, the area has experienced significant environmental degradation in recent decades. Understanding the drivers and impacts of such changes is essential for sustainable management. The primary aim of the present study is to analyze and evaluate the temporal trends of LULC changes and their impact on land surface temperature (LST) in the Hamoun wetland during the years 1990, 2000, 2010, and 2020. Using satellite data and remote sensing techniques, this research seeks to identify spatial-temporal patterns of change to support sustainable environmental resource management in the region

2. Materials and methods

2.1. Study area

The Hamoun Wetland is located between 60 degrees 39 minutes and 61 degrees 35 minutes Eastern longitude and 31 degrees 15 minutes and 31 degrees 32 minutes Northern latitude. This wetland consists of lakes, ponds, and marshes, with its surface area constantly fluctuating and changing. The maximum area of Hamoun Wetland is approximately 5700 square kilometers, of which 3820 square kilometers are located in Iran [22]. The depth range of the wetland varies between 1 to 7 meters. Hamoun contains mostly permanent, freshwater lakes. This region is situated in a dry and desert climate of Iran, with an annual rainfall of approximately 61 mm [23]. Geologically, it is part of the Helmand basin, a large portion of which is located in Afghanistan. Fig. 1 shows the location of the study area.

2.2. Data used

To assess the trend of land use/land cover changes, Landsat 8 satellite images were obtained from the Earth Explorer website (earthexplorer.usgs.gov) and were prepared for necessary preprocessing and processing. The details of these images are provided in Table 1.

For preparing the land use map on the acquired images, radiometric correction and atmospheric correction were performed [24]. After applying the necessary preprocessing steps, the land use classification map for the Hamoun region for the years 1990, 2000, 2010, and 2020 was created in the GIS environment. Then, supervised classification using the CART model was applied. This method is recognized as a powerful yet simple tool [25, 26]. In fact, the analysis of complex data requires analytical methods that can control nonlinear relationships and interactions. CART is an invariant regression method. The advantages of using the CART method are:

1. The use of a wide variety of variables, including categorical data, survival data, and ordinal data,
2. Simplicity and robustness,
3. Ease of decomposition, analysis, and interpretation, and
4. The ability to handle missing data.

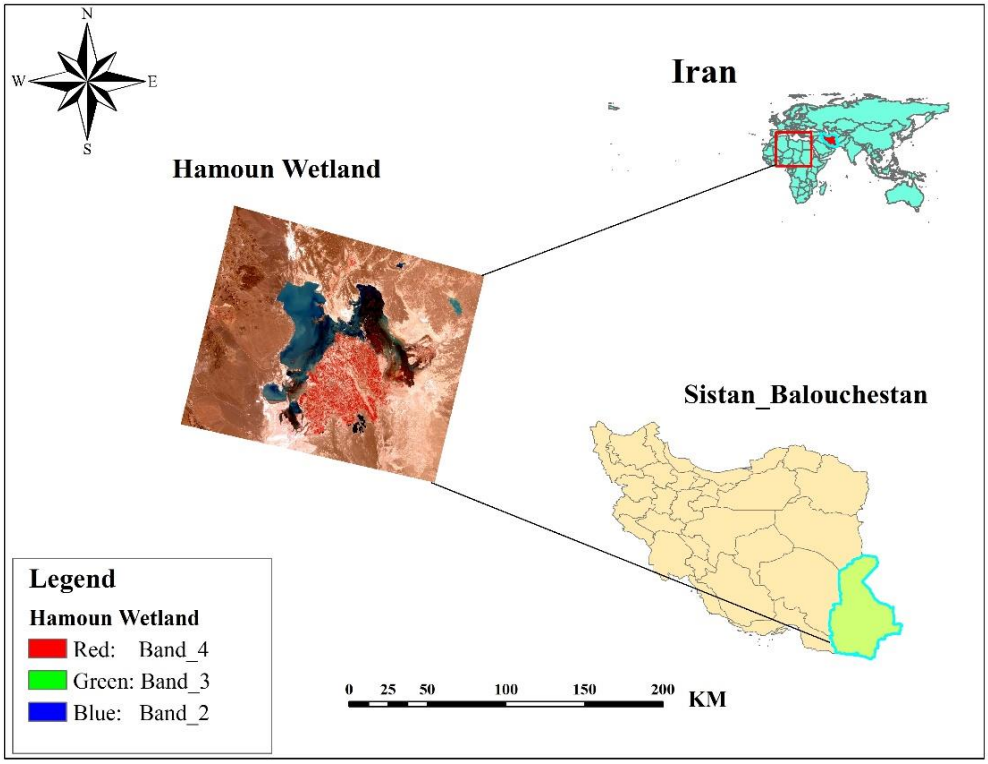

Fig. 1. Location of Hamoun wetland.

Table 1. Specifications of the satellite images used.

Gregorian	Row/Path	Satellite	Sensor	Spatial Resolution (Meters)
1990	39/157	Landsat 5	TM	30
2000	39/157	Landsat 5	TM	30
2010	39/157	Landsat 5	TM	30
2020	39/157	Landsat 5	TM	30

Therefore, this method can serve as an alternative to traditional methods such as logistic regression, multiple regression, and logarithmic-linear models. The CART method was specifically chosen over other classification algorithms such as Support Vector Machines (SVM) and Random Forest due to its interpretability, lower computational cost, and strong performance on datasets with noise and limited sample sizes. This makes CART particularly suitable for analyzing land use changes in complex and ecologically sensitive regions like the Hamoun wetland. The images for land use in the years 1990, 2000, 2010, and 2020 were classified into six land classes, including residential and built-up areas, agricultural land, pastures and low-cover areas, barren land, reed beds, and water bodies. The details of each of these land uses are provided in Table 2. Additionally, NDVI indices were used to estimate vegetation cover, as shown in Eq. 1 [27, 28].

$$\mathrm{NDVI} = \frac{\mathrm{NIR}-\mathrm{R}}{\mathrm{NIR}+\mathrm{R}} \quad (1)$$

$$\mathrm{NDWI} = \frac{\mathrm{B3}-\mathrm{B5}}{\mathrm{B3}+\mathrm{B5}} \quad (2)$$

Table 2. Details of land uses used in the study.

Land Use Land Changes	Explanations
Residential and human-made areas	Residential, commercial areas, transportation networks such as roads and rail networks
Agricultural lands	Dense vegetation cover, agricultural, orchard, and cultivated lands
Pastures and lands with sparse vegetation	Pastures, lands with sparse vegetation
Wastelands	Saline lands and areas without vegetation cover
Water vegetation	Vegetation cover in waterbeds
Waterbeds	Lakes, dams, semi-deep wells

In Eq. 1, NIR represents the near-infrared band, R is the red band, and SWR refers to the shortwave infrared band. The values of these indices typically range between −1 and +1, where values closer to +1 indicate higher index levels. NDVI values range from −1 to +1 regardless of brightness, reflectance, or DN used as input. Generally, negative NDVI values correspond to water bodies, values close to zero are associated with rocks, sands, or concrete surfaces, and positive values indicate vegetative cover, including

plants, shrubs, grasses, and forests. Moreover, many researchers have utilized the Normalized Difference Vegetation Index (NDVI) to detect land cover changes, as it effectively distinguishes vegetation (positive values), bare soil (values near zero), and water bodies (negative values).

In Eq. 2, B3 is the green band, which reflects visible light and is useful for detecting water; B5 is the near-infrared (NIR) band, which is strongly absorbed by water. The NDWI value ranges from -1 to +1, and values greater than zero typically indicate the presence of water bodies.

After the completion of the land use maps and classification of the land uses, the accuracy of these land uses was evaluated. An error matrix was created to assess the accuracy of the generated land uses compared to the ground reality. In this matrix, the producer's accuracy, user's accuracy, overall accuracy, and Kappa coefficient were calculated [29]. The Kappa index considers the incorrectly classified pixels and calculates the classification accuracy relative to a completely random classification. The Kappa index was calculated using Eq. 3.

$$Kappa = \frac{P_0 - P_c}{1 - P_c} \quad (3)$$

In this equation, P_0 represents the observed accuracy, and Pc represents the expected agreement.

2.3. Land use and land cover changes

In this study, land use and land cover changes were examined by analyzing the changes in classified classes during the years 1990, 2000, 2010, and 2020. Accordingly, the changes in various classes were calculated in terms of square kilometers and percentages.

$$Percentage\ of\ Changes = \left(\frac{\mathrm{A}-\mathrm{B}}{\mathrm{B}}\right) * 100 \quad (4)$$

$$Rate\ of\ changes\ (kilometers\ per\ year) = \left(\frac{\mathrm{A}-\mathrm{B}}{C}\right) * 100 \quad (5)$$

In this equation, A represents the area of land use and land cover in the second year, and B represents the area of land use and land cover in the first year. Subsequently, land use changes during the years 1990, 2000, 2010, and 2020 were obtained.

2.4. Land surface temperature data

In climate change studies, one of the most significant indicators reflecting the impacts of climate change is the variation in land surface temperature. Therefore, in this research, to assess the impact of land use on changes in land surface temperature, data from the MODIS satellite under the product name MOD11A2 with a spatial resolution of one kilometer and 8-day temporal intervals for the years 1990, 2000, 2010, and 2020 were extracted from the Earth Data website. The MODIS satellite includes two sensors, Aqua and Terra, which provide long-term datasets with similar land physical parameters for climate and global change studies [30].

2.5. Palmer drought severity index (PDSI)

The Palmer Drought Severity Index (PDSI) is another widely used drought index for monitoring hydrological droughts and is increasingly applied to assess the impacts of climate change [31, 32]. This index is calculated based on temperature, precipitation, and soil moisture data [33]. Table 3 shows the range of PDSI values, which typically vary between -4 and +4 [34].

Table 3. Palmer Drought Severity Index (PDSI) classification.

Drought Range	Drought Classification
<-4	Severe Drought
(-4, -3)	Moderate Drought
(-3, -2)	Mild Drought
(-2, -1)	Normal Wetness
(-1, +1)	Slightly Wet
(+1, +2)	Moderately Wet
(+2, +3)	Very Wet
(+3, +4)	Extremely Wet

3. Results

3.1. Land use changes from 1990 to 2020

The results of the study on land use change over 40 years from 1990 to 2020 are presented in Fig. 2 and Table 4. This study showed that residential areas in the years 1990, 2000, 2010, and 2020 were 0.04%, 0.10%, 0.20%, and 0.30%, respectively, indicating an increasing trend over this period. Additionally, barren lands in 2010 and 2020 were 6714.22 km² and 7166.79 km², respectively, and pastures and lands with sparse vegetation had the largest area during these years, with 13460.84 km² and 14471.50

km², respectively. Over these four decades, reed beds had the smallest area, with 4.64%, 3.14%, 2.27%, and 0.38%, respectively. Moreover, water bodies decreased from 2607.17 km² in 1990 to 573.17 km² in 2020.

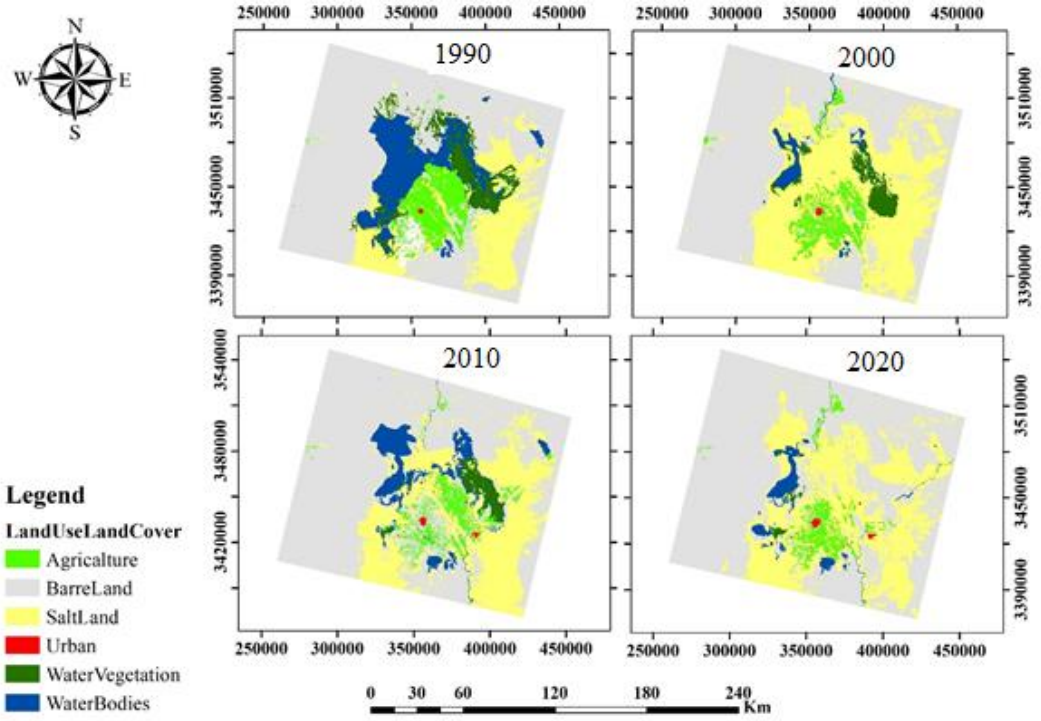

Fig. 2. Land use change map for 1990, 2000, 2010, and 2020 Hamun wetland.

Table 4. Accuracy assessment of land use classes for the years 1990, 2000, 2010, and 2020, Hamun wetland.

	1990				2000				2010				2020			
LULC	Producer Accuracy	User Accuracy	Kappa Coefficient	Overall Accuracy	Producer Accuracy	User Accuracy	Kappa Coefficient	Overall Accuracy	Producer Accuracy	User Accuracy	Kappa Coefficient	Overall Accuracy	Producer Accuracy	User Accuracy	Kappa Coefficient	Overall Accuracy
Agriculture	0.95	0.96			0.99	0.95			0.97	0.96			1	0.96		
SaltLand	0.95	0.98			0.94	0.99			0.94	0.99			0.92	0.98		
BarreLand	0.97	0.98	0.97	0.96	0.94	0.98	0.97	0.96	0.97	0.97	0.96	0.95	0.92	0.97	0.98	0.98
Urban	1	0.93			1	0.92			1	0.94			1	0.93		
WaterVegetation	0.97	0.97			0.99	0.99			0.97	0.97			1	0.94		
WaterBodies	1	0.97			1	0.96			0.99	0.97			1	0.96		

3.2. Accuracy assessment of Hamun land use classes from 1990 to 2020

The evaluation of the accuracy of the Hamun land use maps over 40 years from 1990 to 2020, as shown in **Table 4**, revealed that the Kappa coefficient was 0.97%, 0.97%, 0.96%, and 0.98% for each year, and the overall accuracy was approximately 96%, 96%, 95%, and 98%, respectively. The results of the accuracy estimation for six land use classes—barren lands, pastures and lands with sparse vegetation, reed beds, agriculture, water bodies, and residential areas in the Hamun Lake basin from 1990 to 2020—indicated that the overall accuracy was above 95% and the Kappa coefficient was above 94%, demonstrating sufficient accuracy in the produced land use maps (Table 4).

In this study, the analysis of land use changes in the study area showed that the percentage of barren lands, residential and human-made areas, pastures, and lands with sparse vegetation increased over the four decades. In contrast, the percentage of agricultural lands, reed beds, and water bodies decreased from 8.56%, 4.64%, and 11.25% in 1990 to 3.53%, 0.38%, and 2.47% in 2020, respectively.

Between 1990 and 2000, a decrease in agricultural lands, pastures, and lands with sparse vegetation, and water bodies was observed. Specifically, barren lands, residential and human-made areas, and reed beds increased by 21.28%, 0.06%, and 9.39%, respectively. Furthermore, between 2000 and 2010, pastures and lands with sparse vegetation, residential and human-made areas, and reed beds were on the rise. However, during this period, agricultural lands, barren lands, and water bodies decreased by -0.88%, -9.19%, and -0.87%, respectively. Between 2010 and 2020, reed beds and water bodies showed a decreasing trend of -3.48% and -1.91%, respectively. On the other hand, agricultural lands, pastures and lands with sparse vegetation, barren lands, and residential

areas increased.

Overall, from 1990 to 2020, the trend in land use changes for pastures and lands with sparse vegetation, barren lands, and residential and human-made areas increased by 3.88%, 14.05%, and 0.16%, respectively, while agricultural lands, reed beds, and water bodies decreased by -5.04%, -8.78%, and -4.27% (Table 5).

Table 5. Rate and percentage of area changes in hamun wetland land uses from 1990 to 2020.

Use Types Land	1990-2000%	2000-2010	2010-2020	1990-2020
Agricultural Land	-3.44	-0.88	-0.72	-5.04
Pastures and Lands with Sparse Vegetation	-7.02	6.75	4.14	3.88
Barren Lands	21.28	-9.19	1.95	14.05
Residential and Human-Made Areas	0.06	0.09	0.00	0.16
Water Vegetation	9.39	4.09	-3..48	-8.78
Water Bodies	-1.50	-0.87	-1.91	-4.27

During the years 2000–1990, out of 100 percent of agricultural lands, 48 percent were converted to pastures and lands with sparse vegetation, and out of 100 percent of water bodies, 68 percent were converted to pastures and lands with sparse vegetation, Moreover, out of 100 percent of reed beds, 51 percent were converted to pastures and lands with sparse vegetation, whereas during the years 2020–2010, out of 100 percent of agricultural lands, 42 percent were converted to pastures and lands with sparse vegetation, out of 100 percent of water bodies, 57 percent were converted to pastures and lands with sparse vegetation, and out of 100 percent of reed beds, 78 percent were converted to barren lands. Additionally, during the years 1990–2020, out of 100 percent of agricultural lands, 50 percent were converted to pastures and lands with sparse vegetation, out of 100 percent of water bodies, 53 percent were converted to pastures and lands with sparse vegetation, and out of 100 percent of reed beds, 50 percent were converted to barren lands and 45 percent to pastures and lands with sparse vegetation (Fig. 3).

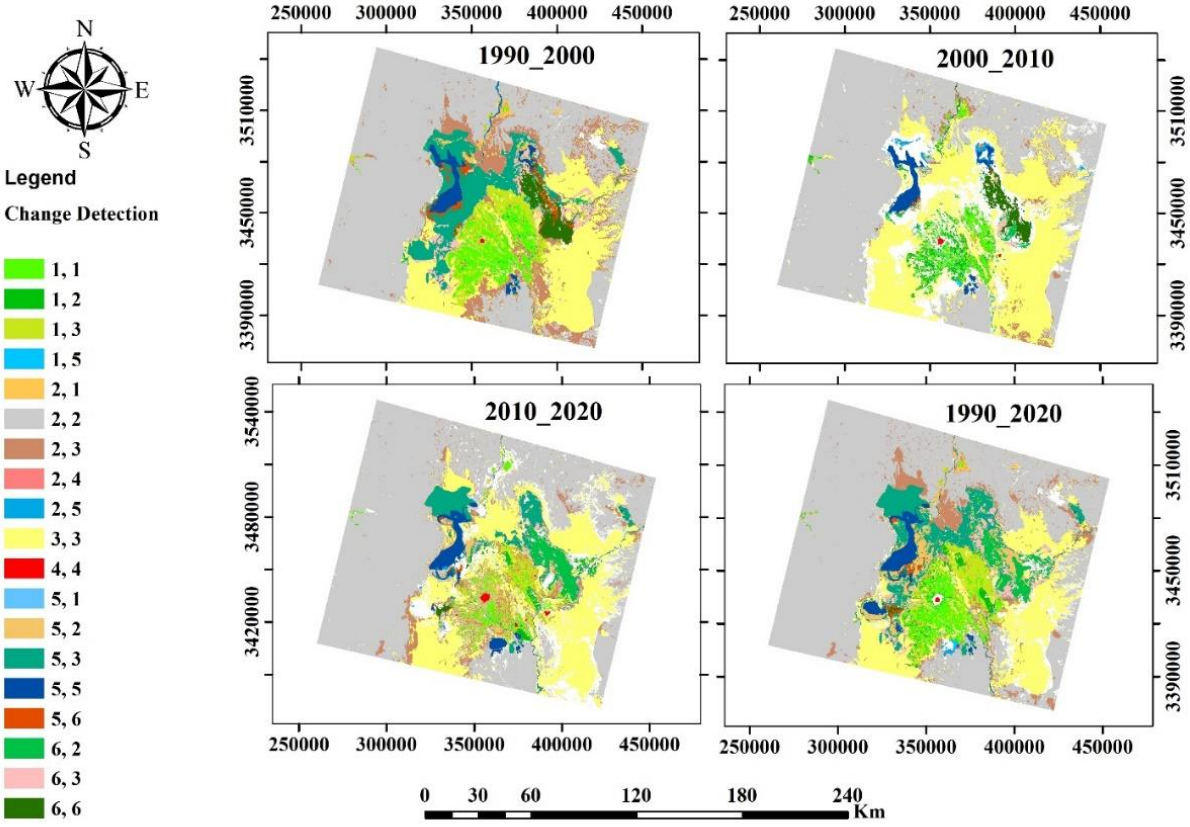

Fig. 3. Rates and percentage areas of land use changes from 1990 to 2020 in the Hamoun wetland.

The results showed that the NDVI decreased from 1990 to 2010 due to water scarcity and the expansion of barren lands (Fig. 4).

The results also indicate that the water bodies had the highest extent in 1990, but showed a decreasing trend in 2000, 2010, and 2020 due to the onset of drought (Fig. 5).

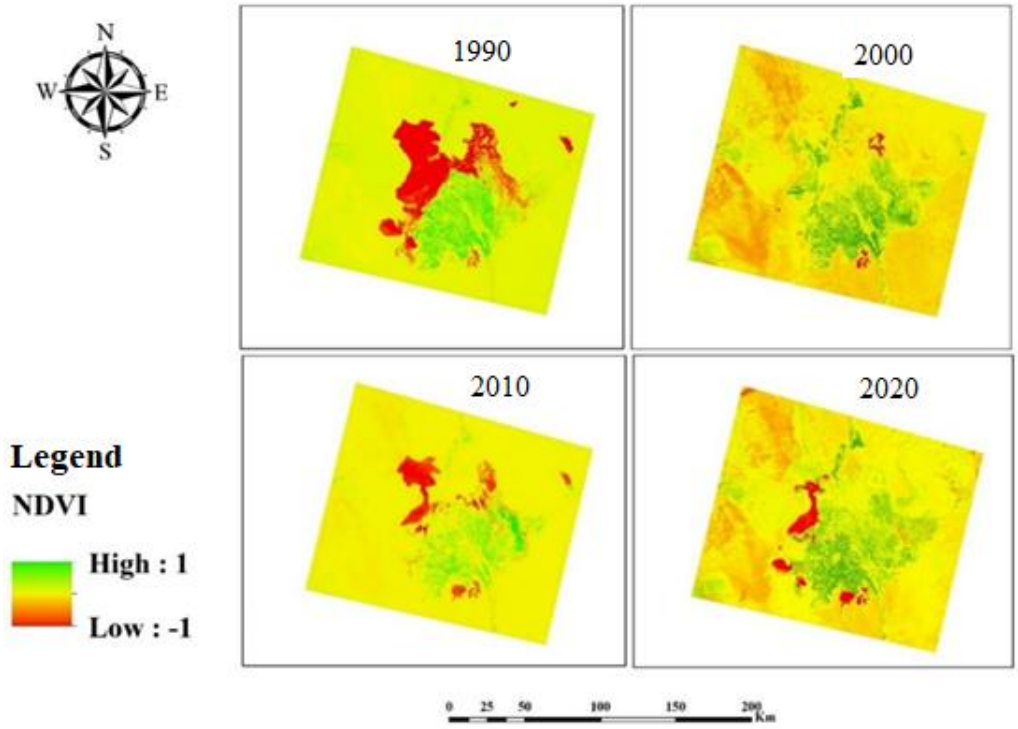

Fig. 4. Normalized difference Vegetation Index (NDVI) in the years 1990, 2000, 2010, and 2020 in the Hamoun wetland.

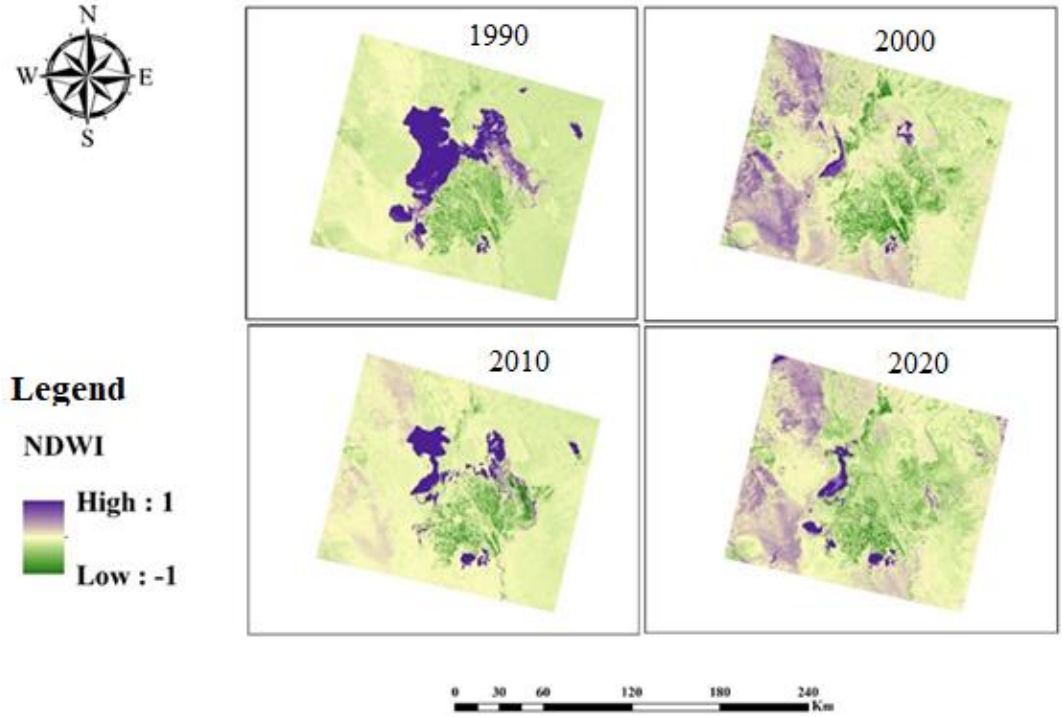

Fig. 5. Water Body index in the years 1990, 2000, 2010, and 2020 in the Hamoun wetland.

3.3. Land surface temperature (LST)

The main issue for government managers in the contemporary context of global warming is the increase in LST in urban areas [35]. As shown in Fig. 6, the highest average daytime temperature in 2000 (Fig. 6(a)) corresponds to barren lands and reed beds, while the lowest average temperature is observed in water bodies. In the same year (2000), the highest average nighttime temperature (Fig. 6(d)) is found in barren and urban areas, and the lowest is in reed beds. In 2010 (Fig. 6(c)), the highest and lowest average daytime temperatures are recorded in barren lands and water bodies, respectively. For the same year, the highest nighttime temperature (Fig. 6(e)) is seen in water bodies, while the lowest is in barren lands. In 2020 (Figs. 6(c) and 6(f)), both daytime and nighttime average temperatures across all land cover types show a decreasing trend. The highest average daytime temperature is found in barren lands, while the lowest is in water bodies (Fig. 6(c)). Conversely, the highest nighttime temperature is seen in water bodies and the lowest in rangelands and sparsely vegetated lands (Fig. 6).

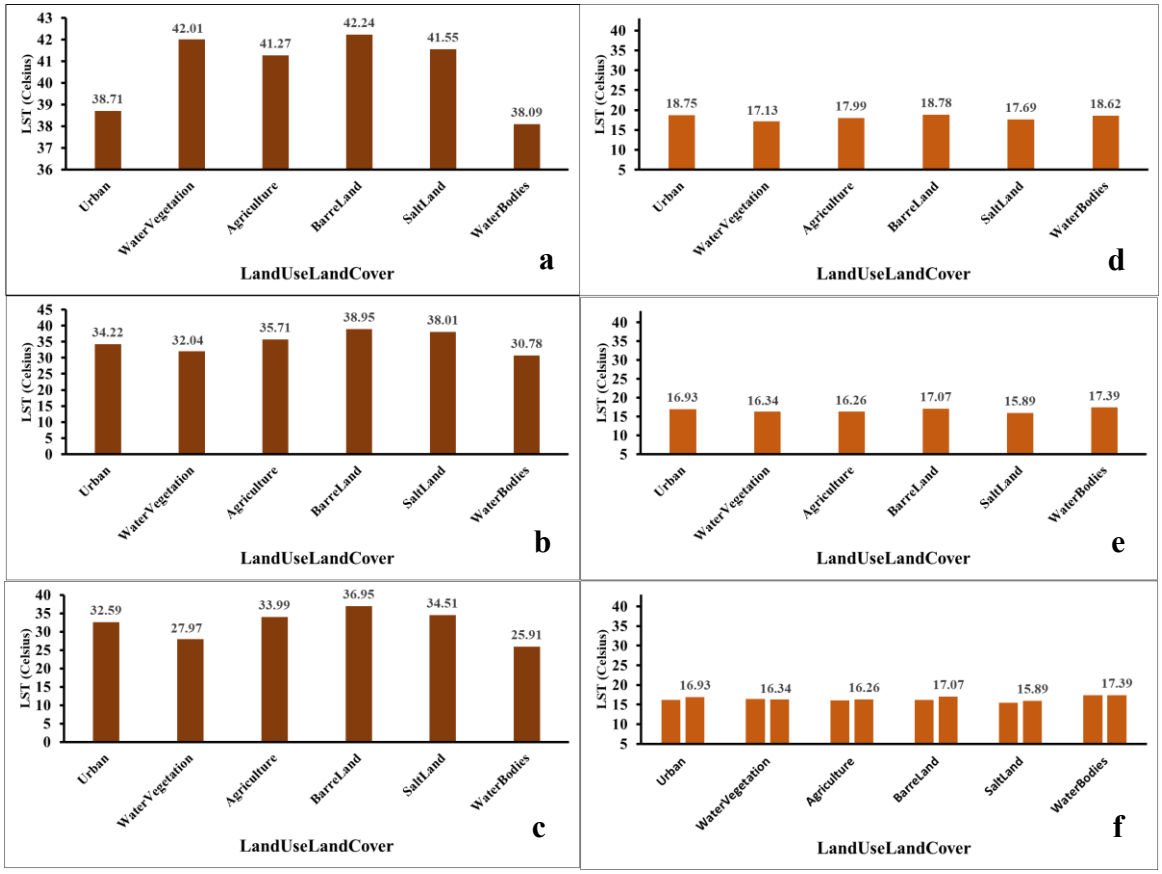

Fig. 6. (a), (b), and (c) Land Surface Day Temperature, (d), (z), and (r) Land Surface Night Temperature in the years 2000, 2010, and 2020 in the Hamoun Wetland.

3.4. Palmer drought severity index

According to the results obtained in Fig. 7, continuous droughts were observed from 1990 to 2020. The results presented in Fig. 8 showed that in 1990, the highest percentage was moderate wet conditions (88.04%), while the lowest percentage was normal drought (11.96%). Additionally, in 2000, the highest amount of drought, including severe, moderate, and mild drought, was observed, with percentages of 0.14%, 36.93%, and 62.93%, respectively. Then, in 2010, moderate drought (34.51%) and mild drought (65.49%) had the highest percentages. Finally, in 2020, four classes were evaluated in the region: moderate wet, mild, very wet, and extremely wet, with the highest percentage being very wet (42.31%), as identified in Fig. 7.

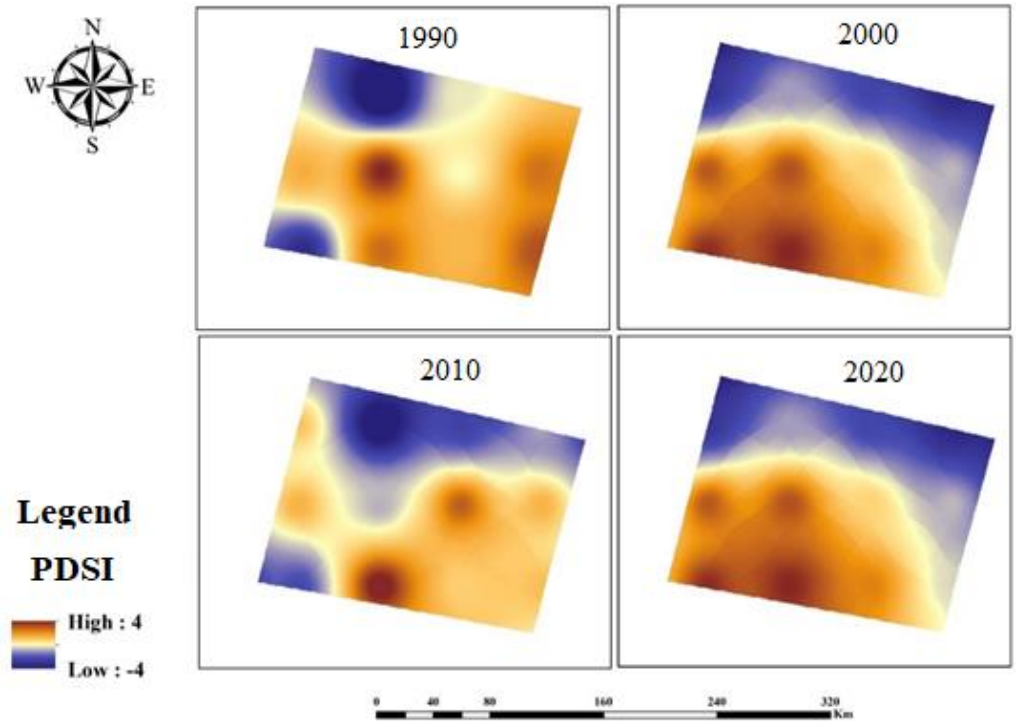

Fig. 7. Palmer drought index for the years 1990, 2000, 2010, and 2020 in Hamoun wetland.

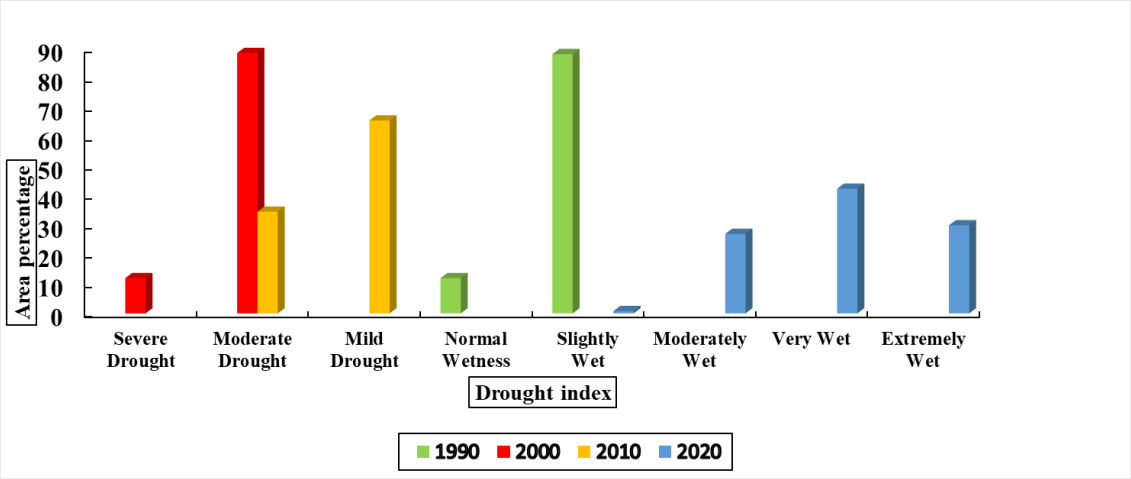

Fig. 8. Palmer drought index for the years 1990, 2000, 2010, and 2020 in Hamoun wetland.

The drought indices in 2000 and 2010 show moderate, normal, and extended droughts. As shown in Fig. 8, a significant drying of the water body occurred in 2000. Additionally, moderate wet conditions were observable in 1990, and more severe wet conditions occurred in 2010. With the land use changes, a decrease in temperature in the studied area was observed, which is due to the droughts that occurred over these four decades.

4. Discussion

The results of the land use change analysis using satellite images in the study area showed that over these forty years, the trend of water bodies, agricultural lands, and reed beds decreased, while barren lands, pastures, areas with sparse vegetation, and cities increased. This aligns with the results of Safari Shad et al. (2000). In other words, over time, with the reduction of water bodies, the amount of agricultural lands and reed beds decreased, but pastures, barren lands, and urban areas increased. Due to the increase in barren lands, conditions suitable for soil erosion potential arise, leading to massive 120-day dust storms blowing from the wetland to the residential areas [36]. On the other hand, Maleki and Koupaei [37] indicated that between 1985 and 2020, in the Hamun wetland, water flowed only 20% of the time, and on average, for less than two months between 1985 and 2020. It also shows that due to repeated droughts and reduced water inflows to Iran, parts of the water bodies have completely dried up. In these years, farmers, livestock herders, fishermen, and wildlife have been harmed [37]. These issues highlight the importance of restoring the Hamun wetland. Furthermore, with the reduction of barren lands, the potential for soil erosion has also decreased. The surface temperature analysis results show a significant decreasing trend from 1990 to 2020, attributed to the ongoing droughts during this period.

The study of climate change trends conducted by Karami et al. [38] indicates a decrease in water reserves. Therefore, the findings of this study show a reduction in water reserves in this wetland due to drought.

The results of the studies by Haji Hosseini et al. [39] regarding land use changes downstream of the Kajaki Dam in Afghanistan showed that the increase in the area under cultivation of agricultural products is one of the reasons for the decrease in the runoff entering Iran from the Helmand River, leading to a reduction in the cultivated area and an increase in barren lands.

According to these results, there is a direct relationship between land use changes and the lives of stakeholders. Sharif Nia et al. [40] examined the situation of stakeholder groups (livestock herders, farmers, etc.) regarding their connection to the wetland and found that stakeholders considered the restoration of this wetland essential for their livelihoods and it has a significant impact on the local population's lives.

5. Conclusion

The present study was conducted to examine the trend of land use changes and their effect on land surface temperature (LST) in the Hamoun wetland from 1990 to 2020 using Geographic Information Systems (GIS) and remote sensing. Landsat 5 and 8 images were used for analyzing the land use changes. Additionally, annual temperature data were used to examine temperature changes, and the Palmer Drought Severity Index (PDSI) was utilized to assess drought conditions.

Overall, the land use changes in the Hamoun wetland were analyzed over four decades using the supervised classification method (CART), which showed a high Kappa coefficient of over 94%. The results of the current study indicate that the area of water bodies has decreased, leading to a reduction in agricultural lands and reed beds. As a result of these changes, pastures, areas with sparse vegetation, barren lands, and urban areas have shown an increasing trend. Furthermore, land surface temperature has shown a significant decreasing trend due to the occurrence of droughts over these decades. In general, the area of water bodies, reed beds, agricultural lands, and the average land surface temperature have decreased.

Thus, by using Landsat 5 and 8 images, the trend of land use changes can be effectively assessed, and by using MODIS images, the changes in land surface temperature can be accurately estimated. The Hamoun wetland is considered one of the important areas of the country from social, economic, and environmental perspectives. The shortage of incoming water resources and water bodies,

along with the drying up of the wetland, has led to the migration of many people from the border areas. Afghanistan's activities upstream of the Helmand River have had an impact on the water resources entering Iran's basin. During drought periods, due to the lack of water resources and the increase in barren lands, very few farmers and livestock herders have been able to use the area.

Due to the water shortage in the studied region, the conditions have become very challenging, especially for stakeholders in agriculture, which has created migration conditions for these stakeholders. According to the presented results, the changes in the extent of water bodies have affected other land uses. Therefore, the preservation and restoration of the Hamoun wetland and the management of water resources are crucial for the living conditions in the region.

Statements & declarations

Author Contributions

Mozhgan Yarahmadi: Conceptualization, Investigation, Methodology, Formal analysis, Resources, Writing - Original Draft, Writing - Review & Editing.

Hadi Eskandari Damaneh: Investigation, Visualization, Validation, Formal analysis, Resources, Writing - Original Draft, Writing - Review & Editing.

Shahram Khalighi Sigaroodi: Conceptualization, Methodology, Formal analysis, Project administration, Supervision, Writing - Review & Editing.

Funding

The authors received no financial support for the research, authorship, and/or publication of this article.

Declarations

The authors declare no conflict of interes.

Data availability

The data presented in this study will be available on interested request from the corresponding author.

References

[1] FAO/UNEP. Terminology for integrated resources planning and management. Rome (Italy): Food and Agriculture Organization/United Nations Environment Programme; 1999.

[2] Mann, M. E., Zhang, Z., Rutherford, S., Bradley, R. S., Hughes, M. K., Shindell, D., Ammann, C., Faluvegi, G., Ni, F. Global Signatures and Dynamical Origins of the Little Ice Age and Medieval Climate Anomaly. Science, 2009; 326 (5957): 1256–1260. doi:10.1126/science.1177303.

[3] Ramachandra, T. V., Aithal, B. H., D, D. S. Land Surface Temperature Analysis in an Urbanising Landscape through Multi- Resolution Data. Research & Reviews: Journal of Space Science & Technology, 2012; 1 (1): 1–10.

[4] Sahoo, S., Dhar, A., Kar, A. Environmental Vulnerability Assessment Using Grey Analytic Hierarchy Process Based Model. Environmental Impact Assessment Review, 2016; 56: 145–154. doi:10.1016/j.eiar.2015.10.002.

[5] Guo, Z., Wang, S. D., Cheng, M. M., Shu, Y. Assess the Effect of Different Degrees of Urbanization on Land Surface Temperature Using Remote Sensing Images. Procedia Environmental Sciences, 2012; 13: 935–942. doi:10.1016/j.proenv.2012.01.087.

[6] Kidder, S. Q., Wu, H. T. A Multispectral Study of the St. Louis Area under Snow-Covered Conditions Using NOAA-7 AVHRR Data. Remote Sensing of Environment, 1987; 22 (2): 159–172. doi:10.1016/0034-4257(87)90056-3.

[7] Balling, R. C., Brazel, S. W. High-Resolution Surface Temperature Patterns in a Complex Urban Terrain. Photogrammetric Engineering & Remote Sensing, 1988; 54 (9): 1289–1293.

[8] Srivastava, P. K., Majumdar, T. J., Bhattacharya, A. K. Study of Land Surface Temperature and Spectral Emissivity Using Multi-Sensor Satellite Data. Journal of Earth System Science, 2010; 119 (1): 67–74. doi:10.1007/s12040-010-0002-0.

[9] Zhang, F., Tiyip, T., Kung, H., Johnson, V. C., Maimaitiyiming, M., Zhou, M., Wang, J. Dynamics of Land Surface Temperature (LST) in Response to Land Use and Land Cover (LULC) Changes in the Weigan and Kuqa River Oasis, Xinjiang, China. Arabian Journal of Geosciences, 2016; 9 (7). doi:10.1007/s12517-016-2521-8.

[10] Zhao, Q., Haseeb, M., Wang, X., Zheng, X., Tahir, Z., Ghafoor, S., Mubbin, M., Kumar, R. P., Purohit, S., Soufan, W., Almutairi, K. F. Evaluation of Land Use Land Cover Changes in Response to Land Surface Temperature With Satellite Indices and Remote Sensing Data. Rangeland Ecology and Management, 2024; 96: 183–196. doi:10.1016/j.rama.2024.07.003.

[11] Saleem, H., Ahmed, R., Mushtaq, S., Saleem, S., Rajesh, M. Remote Sensing-Based Analysis of Land Use, Land Cover, and Land Surface Temperature Changes in Jammu District, India. International Journal of River Basin Management, 2024; 1–16.

doi:10.1080/15715124.2024.2327493.

[12] Hussain, S., Karuppannan, S. Land Use/Land Cover Changes and Their Impact on Land Surface Temperature Using Remote Sensing Technique in District Khanewal, Punjab Pakistan. Geology, Ecology, and Landscapes, 2023; 7 (1): 46–58. doi:10.1080/24749508.2021.1923272.

[13] Al Rakib, A., Akter, K. S., Rahman, M. N., Arpi, S., Kafy, A. A. Analyzing the pattern of land use land cover change and its impact on land surface temperature: a remote sensing approach in Mymensingh, Bangladesh. In: Proceedings of the 1st International Student Research Conference - 2020; 2020 Apr; Dhaka, Bangladesh.

[14] Gohain, K. J., Mohammad, P., Goswami, A. Assessing the impact of land use land cover changes on land surface temperature over Pune city, India. Quaternary International, 2021; 575: 259–269. doi:10.1016/j.quaint.2020.04.052.

[15] Tan, J., Yu, D., Li, Q., Tan, X., Zhou, W. Spatial Relationship between Land-Use/Land-Cover Change and Land Surface Temperature in the Dongting Lake Area, China. Scientific Reports, 2020; 10 (1): 9245. doi:10.1038/s41598-020-66168-6.

[16] Parastatidis, D., Mitraka, Z., Chrysoulakis, N., Abrams, M. Online Global Land Surface Temperature Estimation from Landsat. Remote Sensing, 2017; 9 (12): 1208. doi:10.3390/rs9121208.

[17] Dissanayake, D., Morimoto, T., Ranagalage, M. Accessing the Soil Erosion Rate Based on RUSLE Model for Sustainable Land Use Management: A Case Study of the Kotmale Watershed, Sri Lanka. Modeling Earth Systems and Environment, 2019; 5 (1): 291–306. doi:10.1007/s40808-018-0534-x.

[18] Jiang, J., Tian, G. Analysis of the Impact of Land Use/Land Cover Change on Land Surface Temperature with Remote Sensing. Procedia Environmental Sciences, 2010; 2: 571–575. doi:10.1016/j.proenv.2010.10.062.

[19] Yue, W., Xu, J., Tan, W., Xu, L. The Relationship between Land Surface Temperature and NDVI with Remote Sensing: Application to Shanghai Landsat 7 ETM+ Data. International Journal of Remote Sensing, 2007; 28 (15): 3205–3226. doi:10.1080/01431160500306906.

[20] Nunes, M. C. S., Vasconcelos, M. J., Pereira, J. M. C., Dasgupta, N., Alldredge, R. J., Rego, F. C. Land Cover Type and Fire in Portugal: Do Fires Burn Land Cover Selectively? Landscape Ecology, 2005; 20 (6): 661–673. doi:10.1007/s10980-005-0070-8.

[21] Huang, S., Siegert, F. Land Cover Classification Optimized to Detect Areas at Risk of Desertification in North China Based on SPOT VEGETATION Imagery. Journal of Arid Environments, 2006; 67 (2): 308–327. doi:10.1016/j.jaridenv.2006.02.016.

[22] Dehghani, T., Koolivand, I., Mehdizadeh, S., Ahmadpari, H., Zolfagharan, A., Mohamadi, E. Monitoring land-use changes using remote sensing, ENVI and ArcGIS software in Hamoun Wetlands. In: Proceedings of the 3rd International and 6th National Conference on Conservation of Natural Resources and Environment; 2022 Sep 12–13; Ardabil, Iran.

[23] Kharazmi, R., Abdollahi, A. A., Rahdari, M. R., Karkon varnosfaderani, M. Monitoring Land Use Change and its Impacts on Land Degradation and Desertification Trend Using Landsat Satellite Images (Case study: East of Iran, Hamoon Wetland). Journal of Arid Regions Geographic Studies, 2022; 7(25): 64-75.

[24] Eskandari Damaneh, H., Zehtabian, G. R., Khosravi, H., Azareh, A. Investigation and Analysis of Temporal and Spatial Relationship between Meteorological and Hydrological Drought in Tehran Province. Scientific- Research Quarterly of Geographical Data (SEPEHR), 2016; 24(96): 113-120. doi:10.22131/sepehr.2016.18947.

[25] Biro, K., Pradhan, B., Buchroithner, M., Makeschin, F. Land Use/Land Cover Change Analysis And Its Impact On Soil Properties In The Northern Part Of Gadarif Region, Sudan. Land Degradation and Development, 2013; 24 (1): 90–102. doi:10.1002/ldr.1116.

[26] Yousefi J. Image binarization using the Otsu thresholding algorithm. Ontario (Canada): University of Guelph; 2011.

[27] Tucker, C. J., Justice, C. O., Prince, S. D. Monitoring the Grasslands of the Sahel 1984-1985. International Journal of Remote Sensing, 1986; 7 (11): 1984–1985. doi:10.1080/01431168608948954.

[28] Gao, B. C. NDWI - A Normalized Difference Water Index for Remote Sensing of Vegetation Liquid Water from Space. Remote Sensing of Environment, 1996; 58 (3): 257–266. doi:10.1016/S0034-4257(96)00067-3.

[29] Kafy, A. A., Naim, M. N. H., Subramanyam, G., Faisal, A. Al, Ahmed, N. U., Rakib, A. Al, Kona, M. A., Sattar, G. S. Cellular Automata Approach in Dynamic Modelling of Land Cover Changes Using RapidEye Images in Dhaka, Bangladesh. Environmental Challenges, 2021; 4: 100084. doi:10.1016/j.envc.2021.100084.

[30] Salomonson, V. V, Guenther, B., Masuoka, E. A summary of the status of the EOS Terra Mission Moderate Resolution Imaging Spectroradiometer (MODIS) and attendant data product development after one year of on-orbit performance. In: Proceedings of the International Geoscience and Remote Sensing Symposium (IGARSS); 2001 Jul 9–13; Sydney, Australia. doi:10.1109/igarss.2001.976790.

[31] Mika, J., Horváth, S., Makra, L., Dunkel, Z. The Palmer Drought Severity Index (PDSI) as an Indicator of Soil Moisture. Physics and Chemistry of the Earth, 2005; 30 (1-3 SPEC. ISS.): 223–230. doi:10.1016/j.pce.2004.08.036.

[32] Zhai, J., Su, B., Krysanova, V., Vetter, T., Gao, C., Jiang, T. Spatial Variation and Trends in PDSI and SPI Indices and Their Relation to Streamflow in 10 Large Regions of China. Journal of Climate, 2010; 23 (3): 649–663. doi:10.1175/2009JCLI2968.1.

[33] Barichivich, J., Osborn, T., Harris, I., van der Schrier, G., & Jones, P. (2021). Monitoring global drought using the self-calibrating Palmer Drought Severity Index [in" State of the Climate in 2020" eds. Dunn RJH, Aldred F, Gobron N, Miller JB & Willett KM]. Bulletin of the American Meteorological Society, 102(8), S68-S70. doi: 10.1175/BAMS-D-21-0098.1.

[34] Zheng, Z., Jin, L., Li, J., Chen, J., Zhang, X., Wang, Z. Moisture Variation Inferred from Tree Rings in North Central China and Its Links with the Remote Oceans. Scientific Reports, 2021; 11 (1): 16463. doi:10.1038/s41598-021-93841-1.

[35] Dhar, R. B., Chakraborty, S., Chattopadhyay, R., Sikdar, P. K. Impact of Land-Use/Land-Cover Change on Land Surface Temperature Using Satellite Data: A Case Study of Rajarhat Block, North 24-Parganas District, West Bengal. Journal of the Indian Society of Remote Sensing, 2019; 47 (2): 331–348. doi:10.1007/s12524-019-00939-1.

[36] Miri, A., Ahmadi, H., Ekhtesasi, M. R., Panjehkeh, N., Ghanbari, A. Environmental and Socio-Economic Impacts of Dust Storms in Sistan Region, Iran. International Journal of Environmental Studies, 2009; 66 (3): 343–355. doi:10.1080/00207230902720170.

[37] Maleki, S., Koupaei, S. S., Soffianian, A., Saatchi, S., Pourmanafi, S., Rahdari, V. Human and Climate Effects on the Hamoun Wetlands. Weather, Climate, and Society, 2019; 11 (3): 609–622. doi:10.1175/WCAS-D-18-0070.1.

[38] Karami, R., Salman Mahini, A., Ghobani Nasrabadi, H., Khalil Evaluation of Climate Change in the Hamun International Wetland Basin Using the LARS-WG6 Model. Natural Environmental Hazards, 11 (31): 107–122.

[39] Haji Hosseini, H., Shigan, M., Morid, V., Alireza Study of Land Use Changes Downstream of the Kajaki Dam in the Helmand River Basin, Afghanistan, Using the Maximum Likelihood Classifier. Decision Trees, and Support Vector Machines. Remote Sensing and GIS Journal of Iran, 5 (4).

[40] Sharif Nia, H., Pahlevan Sharif, S., Yaghoobzadeh, A., Yeoh, K. K., Goudarzian, A. H., Soleimani, M. A., Jamali, S. Effect of acupressure on pain in Iranian leukemia patients: A randomized controlled trial study. International Journal of Nursing Practice, 2017; 23(2): e12513. doi:10.1111/ijn.12513.

Civil Engineering and Applied Solutions

Research Article

journal homepage: ceas.journals.umz.ac.ir

CEAS Civil Engineering and Applied Solutions

Dynamic Analysis of Fatigue-Cracked Beams: The Nonlinear Response with the Analytical Method

Ali Asgari [a*], Alireza Khabiri [a]

[a] *Department of Civil Engineering, Faculty of Engineering and Technology, University of Mazandaran, Babolsar, Iran*

ARTICLE INFO

Keywords:
Fatigue beam
Cracked beam
Breathing crack
Nonlinear response
Damping ratio

Article history:
Received 21 April 2025
Accepted 12 May 2025
Available online 01 July 2025

ABSTRACT

In this study, the bending vibration of a fatigue-cracked beam and associated constraint conditions have been solved by implementing the Homotopy Perturbation Method. A structure with a single degree of freedom, varying stiffness, and a periodic function is employed to simulate the dynamic behavior of the beam. The crack is represented as an ongoing disturbance function within the displacement field, which could be obtained from fracture mechanics. The governing equation's solution shows the super harmonics of the dominant frequency, resulting from nonlinear impacts on the dynamic vibration response of the cracked beam. The proposed method gives an analytical closed-form solution that can be easily used to analyze and design structures dynamically. The outcomes show that growing crack depth reduces the natural frequencies of a cracked beam. Moreover, increasing the severity of the crack and moving its location toward the center of the beam increases the system's damping. Perturbation methods rely on a small parameter, which is challenging to determine for real-life nonlinear problems. To overcome this shortcoming, a powerful analytical method is introduced to solve the motion equation of the cracked beam.

1. Introduction

Mathematical modeling of beams and frames, incorporating various theories and effects, is a vital study area within structural engineering [1, 2]. This applied topic plays a crucial role in understanding and predicting the behavior of structural components under diverse loading conditions [3]. Numerous scientific issues and phenomena, including the vibration of a beam with fatigue cracks, occur in nonlinear models [4-6]. Identifying analytical solutions for these problems is challenging. Cracks are typically detected using a nonlinear approach that monitors variations in the dynamic response features, like natural frequencies, damping, and mode shapes [7–9]. In the analysis of linear vibrations in a cracked beam, the beam crack is assumed to stay open during the beam's vibrations [10, 11]. These linear vibration methods often fail to produce practical results due to low defect sensitivity. Ke et al. [12] examined how open-edge crack parameters affect free vibration and buckling features of cracked beams composed of functionally graded materials. The nonlinear performance of a cantilevered cracked beam modeled with bilinear stiffness under harmonic excitation was investigated to deliberate the crack closure effects [13, 14]. Kisa and Brandon [15] employed a bilinear stiffness model to assess the variations in beam stiffness at the crack position. They presented the contact flexural stiffness matrix within a finite element (FE) model to effectively simulate the impact of crack closure, which was integrated into the initial flexural stiffness matrix at the crack site during a half-cycle of shaking. This stiffness matrix deliberates only two conditions: entirely open and entirely closed states of the crack. Under this assumption, the assumed cracked beam exhibits just dual stiffness values: a more significant value for the closed crack state and a smaller value for the wide crack state. This approach suggests that the crack expands and contracts instantaneously. The experimental tests show that the transition between closed and open cracks, and contrarily, happens more smoothly [16]. Abraham and Brandon [17] have modeled the changes in stiffness at the position of the breathing crack by using several expressions of the Fourier transform series.

* Corresponding author.
E-mail addresses: a.asgari@umz.ac.ir (A. Asgari).

https://doi.org/10.22080/ceas.2025.29000.1002.
ISSN: 3092-7749/© 2025 The Author(s). Published by University of Mazandaran.
This article is an open access article distributed under the terms and conditions of the Creative Commons Attribution (CC-BY) license (https://creativecommons.org/licenses/by/4.0/deed.en)
How to cite this article: Asgari, A., Khabiri, A. Dynamic analysis of fatigue-cracked beams: the nonlinear response with the analytical method. Civil Engineering and Applied Solutions. 2025; 1(2): 43-54. doi:10.22080/ceas.2025.29000.1002.

Cheng et al. [18] have examined a single degree of freedom (SDOF) cracked cantilever beam through time-varying stiffness to investigate frequency-forced vibration behavior. The time-varying stiffness of the beam is shown as a regular periodic function. They presumed that the damping ratio of the flexural cracked beam is 0.01 and obtained forced vibration responses of the cracked beam through the numerical Runge-Kutta technique. Likewise, they stated that using an open crack model for crack detection does not provide high accuracy in monitoring fundamental frequency and tends to underestimate the severity of the crack. Following a similar methodology, Ariaei et al. announced a technique to assess the dynamic Euler-Bernoulli undamped beams with the effect of breathing cracks subjected to a moving point mass [19]. This approach utilizes the discrete element technique in conjunction with the FE method. Researchers have similarly employed signal processing methods to establish the above-mentioned model for beam crack detection [20, 21]. Zhang and Testa experimentally explored the closure properties of the vibration response of a fatigue-cracked T-style steel structure [22]. Bovsunovsky and Surace investigated the super harmonic vibration of a flexural cracked cantilever beam caused by the nonlinear effects of crack closure [23]. They clarified that these nonlinear effects create considerable challenges in achieving analytical solutions. Consequently, they employed a FE model, enabling the prediction of alterations in damping due to the cracked beam. They exhibited that nonlinear effects in the vibration response depend on the crack parameters and the damping scale in the vibrating system. In another work, Curadelli et al. employed changes in system damping to identify structural damage through wavelet analysis [24]. Dimarogonas provided valuable, detailed surveys on crack modeling approaches, emphasizing the importance of utilizing practical numerical models in the diagnostic method [25]. The cracked beam's analytical response presents valuable physical insights into the issue at hand, allowing for an easy assessment of how all parameters affect the solution. Rezaee and Hassan Nejad [26] applied an analytical method, the perturbation method, to solve the motion equation of a cracked beam. They demonstrated that the dynamic response of the cracked beam takes the form of an exponential function and a nonlinear oscillatory behavior function. The exponential part of the reaction introduces the decay rate due to the system damping, and the oscillatory portion is the solution of the Mathieu formula, showing super harmonics of the beam's dominant frequency. They also showed that the system response's damping rate can be derived from the constants of the Mathieu equation.

A recent study of contemporary structural health monitoring evaluates infrastructure using high-resolution imaging techniques to identify and measure defects like cracks. Structural engineers rely on this data to refine structural models and assess the safety and integrity of the structures. The practical use of cracked beams is a critical indicator of structural integrity in various applications. By monitoring cracks in beams, engineers can assess the extent of deterioration over time. This is particularly important in civil engineering, where infrastructure such as bridges and buildings must remain safe and functional. Regularly monitoring cracked beams enables timely maintenance interventions and helps prevent catastrophic failures. Additionally, data gathered from cracked beams can inform predictive maintenance strategies, ensuring that resources are allocated efficiently and that infrastructure remains reliable for public use [27]. An experimental study examined the relationship between crack propagation and deflection in reinforced concrete beams. A four-point loading test was conducted on specimens with varied reinforcement ratios and concrete cover thicknesses [28].

As is well known, perturbation methods rely on a small parameter, which is often challenging to determine for real-life nonlinear phenomena problems. In this paper, to overcome this shortcoming, a novel, robust analytical technique is presented to solve the governing equation (GE) of motion of the fatigue-cracked beam. The Homotopy Perturbation Method (HPM) deforms a complex problem and turns it into an easily solvable issue. The analytical results for a specified case are compared with typical experimental and numerical methods to validate. This method gives an analytical solution for the nonlinear cracked beam equation, which does not need meshing like the numerical method. Also, this method's result is proposed in the closed-form formula, which can be easily used for further structural evaluations.

2. Mathematical modeling

In practical terms, cracked beams are central to a wide range of applications, from ensuring safety in infrastructure and buildings to informing design processes and enhancing material performance. Understanding cracked beams allows engineers and construction professionals to make informed decisions that improve safety and longevity. According to beam crack modeling, the model conforms to the Euler-Bernoulli assumptions and is excited in its first frequency mode. This assumption is valid when the beam is subject to the initial mode by ignoring the contributions of the higher modes.

This mathematical modeling introduces a practical and credible model for examining the nonlinear dynamic characteristics of an SDOF fatigue-cracked beam. The beam's equivalent mass is located at its center in this model. For better visualization, see the beam's stiffness by the variations in location and depth of the crack (see Fig. 1). Consequently, the disparity of the flexibility of the beam as a result of the crack is assessed. Then, the change in the equivalent stiffness of the fatigue-cracked section through the vibration is assumed to be a time-varying function. However, the lumped parameters of the structure are decisive.

2.1. Assess the flexibility of a beam supported by pins with a crack

Assuming a bending moment is exerted on a fatigue-cracked beam, it will also experience additional rotation due to the crack. The extra rotation at the crack position is proportional to the beam flexure. According to Castigliano's theorem, U_T is the crack's strain energy, and the additional rotation takes the following form [29]:

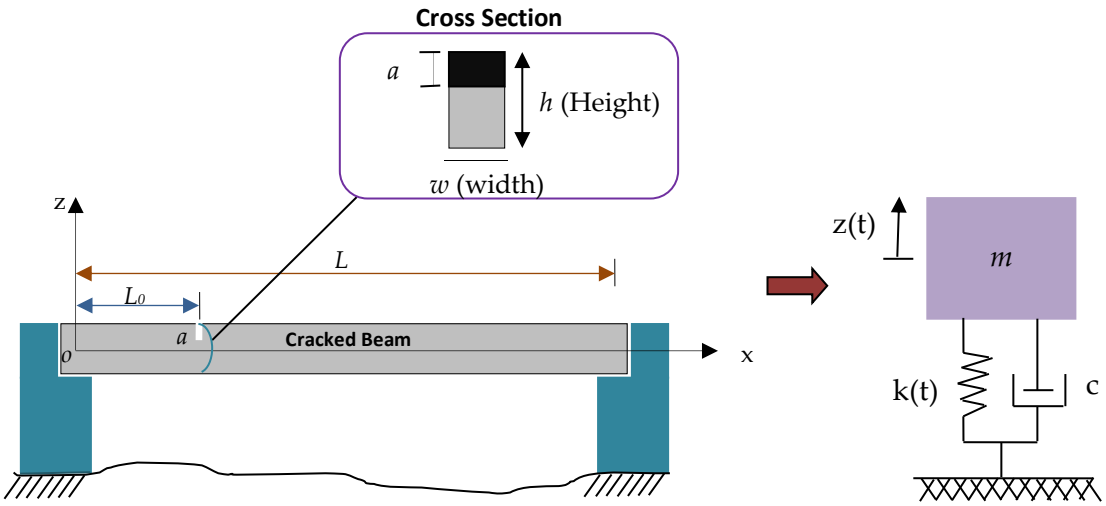

Fig. 1. (a) The pinned-supported fatigue-Cracked beam with a specified damage location, and (b) The schematic SDOF mass, spring, and damping model.

$$\theta = \frac{\partial U_T}{\partial M} \tag{1}$$

The strain energy is presented in the form below [30]:

$$U_T = \int_{Crack} \varsigma_s(\alpha) d\alpha \tag{2}$$

This equation is called the Paries' Equation. The integral in Eq. 2 is an integral over a surface as follows [23]:

$$U_T = \int_{-\frac{w}{2}}^{\frac{w}{2}} \int_0^a \varsigma_s(\alpha) d\alpha dy \tag{3}$$

where the crack depth notation is a, also ς_s is the strain energy density, obtainable from the subsequent equation [31]:

$$\begin{aligned} &\text{Plane strain: } \varsigma_s = \frac{1-\nu^2}{E}\left[K_I^2 + K_{II}^2 + \frac{K_{III}^2}{1-\nu}\right] \\ &\text{Plane stress: } \varsigma_s = \frac{1}{E}[K_I^2 + K_{II}^2 + (1+\nu)K_{III}^2] \end{aligned} \tag{4}$$

In the above formulas E and νrespectively are Young's modulus and Poisson's ratio. In this paper, the plain strain assumption is used. In addition, in Eq. 4, K_I, K_{II},and K_{III} are the Stress Intensity Factors (SIF) related to the fracture modes. In fracture mechanics, the SIF are established for a beam of unit thickness containing a transverse crack [22]. The intensity of stress concerning a single-edge crack under pure bending is:

$$K_I = \sigma_0 \sqrt{\pi a} F_I\left(\frac{a}{h}\right) \tag{5}$$

$$\sigma_0 = \frac{6M}{wh^2} \tag{6}$$

$$\varsigma_s = \frac{1-\nu^2}{E}\sigma_0^2 \pi a F_I^2(\alpha),\ F_I(\alpha) = 1.12 - 1.4\alpha + 7.33\alpha^2 - 13.4\,\alpha^3 + 14\,\alpha^4 \tag{7}$$

By substituting Eq. 7 into Eq. 3 and integrating over the crack surface, the amount of the strain energy U_T can be obtained as:

$$U_T = \frac{36\,\pi\,(1-\nu^2)}{E}\frac{M^2}{wh^2} g(\alpha) \tag{8}$$

where

$$g(\alpha) = 19.6\,\alpha^{10} - 40.7556\,\alpha^9 + 47.1063\,\alpha^8 - 33.051\,\alpha^7 + 20.2948\,\alpha^6 - 9.9736\,\alpha^5 + 4.5948\,\alpha^4 - 1.04533\,\alpha^3 + 0.6272\,\alpha^2 \tag{9}$$

Conversely, the alterations in the beam's flexibility produced by the crack resulted from the formula presented by Dimarogonas and Paipatis [29]:

$$\Delta C = \frac{\partial^2 U_T}{\partial P^2} = \frac{18\,L_0^2 \pi (1-\nu^2)}{Ewh^2} g(\alpha) \tag{10}$$

This equation calculates the changes in flexibility of a pinned-supported beam caused by the crack.

2.2. Finding the motion GE

Assume a uniform pinned-supported beam with a length L, which is shown in Fig. 1. The crack depth is presented as a, and it is situated at a distance of L_0 from the beam's left end. The beam cross-section's width and height are w and h, respectively. It is assumed that the beam vibrates at its fundamental frequency mode. So, the flexurally fatigued cracked beam can be modeled as an SDOF. The crack is modeled as a fatigue crack with breathing behaviors. Henceforward, the beam stiffness will change through the vibration caused by the crack's opening and closing, and the beam's dynamic response will have a nonlinear characteristic.

To achieve the equivalent mass and stiffness of the system, the initial mode shape of the beam is considered to take the form below [32]:

$$\Phi(x) = sin\left(\frac{\pi x}{L}\right) \tag{11}$$

Additionally, the beam stiffness for the scenario of an entirely closed crack is provided by [33]:

$$k_c = \frac{1}{C} = \int_0^L EI\, \Phi''^2(x)\, dx = \frac{\pi^4 EI}{2L^3} \tag{12}$$

where k_c and C represent the stiffness and flexibility of the fatigue-cracked beam once the crack is completely closed, EI is the bending rigidity. Additionally, the notation of the beam's stiffness once the crack model is completely open is $k_o = 1/C_o$, and C_o is the flexibility for the completely open beam's crack as:

$$C_0 = C + \Delta C \tag{13}$$

As previously noted, the flexural Fatigue-Cracked beam's vibration changes the system's equivalent stiffness due to the crack's opening and closing. Thus, the following time-varying function can be employed to model the equivalent stiffness variations of the SDOF structure[19]:

$$k(t) = k_0 + k_{\Delta c}\,[1 + cos(\omega_b t)] \tag{14}$$

In the above formula, $k_{\Delta c}$ represents the amplitude of changes in equivalent stiffness in the following form:

$$k_{\Delta c} = \frac{1}{2}(k_c - k_o) \tag{15}$$

Eq. 14 states that the cracked beam at the static equilibrium position of the beam has a stiffness that represents the average of the maximum stiffness values for both entirely open and entirely closed crack scenarios. Consequently, as the beam vibrates and moves up and down around its equilibrium position, its equivalent stiffness fluctuates around this average value. It is logical to assume that when the beam is displaced in the direction that begins to open the crack, its stiffness gradually decreases; conversely, moving the beam in the opposite direction continuously increases stiffness. In Eq. 14, ω_b is the crack breathing frequency, and for the case of a fully closed crack, $(k(t) = k_c)$, we have $\omega_b t = 2\,n\,\pi,\, n = 1,2,3,\ldots$. and for the case of a fully open crack $(k(t) = k_0)$, we have $\omega_b t = (2\,n - 1)\,\pi, n = 1,2,3,\ldots$. The breathing frequency can be approximated as [34]:

$$\omega_b = \frac{2\omega_c\omega_o}{\omega_c+\omega_o} \tag{16}$$

where $\omega_o = \sqrt{k_o/m}$, and $\omega_c = \sqrt{k_c/m}$ are the frequencies of the cracks that relate to completely open and closed crack cases. Eq. 16 suggests that the system's dominant frequency consistently lies between the open and closed crack cases.

In the above equations, the fraction $m\omega_b^2$ can be written in terms of k_c and k_o as:

$$m\omega_b^2 = \frac{4\,k_o k_c}{k_o+k_c+2\sqrt{k_o k_c}} \tag{17}$$

In addition, to determine the beam's equivalent mass, one could proceed as follows:

$$m = \int_0^L m(x)\,\Phi^2(x)dx = 0.5\,\bar{m}L \tag{18}$$

The mass per unit length of the beam is $\bar{m}$. Taking into account c as the damping equivalent coefficient for the SDOF model of the damaged beam (refer to Fig. 1) and integrating the lumped modal parameters such as equivalent mass and time-varying flexural stiffness, we derive the GE of motion as:

$$m\ddot{z} + c\dot{z} + \{k_o + k_{\Delta c}[1 + cos(\omega_b t)]\}z = 0 \tag{19}$$

An analytical solution for the equation mentioned above has not been reported, and there are numerical solutions that assume a constant damping coefficient [18].

By utilizing the subsequent variable change:

$$t = \frac{2\tau}{\omega_b},\ \frac{dz}{dt} = \frac{\omega_b}{2}\frac{dz}{d\tau},\ \frac{d^2z}{dt^2} = \frac{\omega_b^2}{4}\frac{d^2z}{d\tau^2} \tag{20}$$

and replacing the above relations into Eq. 19, and dividing Eq. 19 by $\frac{4\,m}{\omega_b^2}$ and rearranging the equation, it becomes:

$$\frac{d^2z(\tau)}{d\tau^2} + 4\xi\frac{dz(\tau)}{d\tau} + [\delta + 4\xi^2 + 2\varepsilon\,cos(2\tau)]\,z(\tau) = 0 \tag{21}$$

where, δ, ε and ξ are non-dimensional parameters and damping ratio, respectively, which are defined as:

$$\varepsilon = \frac{2k_{\Delta C}}{m\,\omega_b^2} = \frac{k_c - k_o}{m\,\omega_b^2}, \xi = \frac{c}{2\,m\,\omega_b}, \delta = \frac{4\,(k_o - k_{\Delta C})}{m\,\omega_b^2} - 4\,\xi^2 = \frac{2(k_o + k_c)}{m\omega_b^2} - 4\xi^2 \tag{22}$$

This equation exhibits a stable periodic solution when δ is expressed in terms of ε (with ε being much less than 1) as:

$$\delta = \sum_{i=0}^{\infty} G_i p^i \tag{23}$$

where G_0 is an integer number (G_0 = 0, 1, 2, …) and $p \in [0,1]$ is an embedding parameter, and $G_i (i = 1,2,3,\ldots,\infty)$ represented as the unknown expansion coefficients, which will be determined later. For each value ofG_0one can acquire the corresponding expansion coefficients, thus, the associated transition curves. Each individual point on the curves represents a stable and periodic result to Eq. 21 (Fig. 2). In this illustration, the hatched regions indicate the unstable areas.

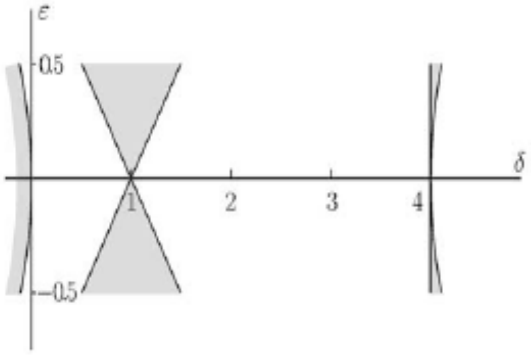

Fig. 2. The Transition curves distinguish among the regions of stability and instability plane. The hatched areas represent the unstable region [34].

By substituting Eq. 17 into Eq. 22, and using relations$k_o = 1/C_o$ and $k_c = 1/C$,ε and δ are obtained as:

$$\varepsilon = \frac{\chi^2 + 2\chi(1+\sqrt{1+\chi})}{4(1+\chi)},\ \chi = \frac{\Delta C}{C} \tag{24}$$

$$\delta = \frac{8 + 2\,\chi^2 + 8\,\chi + 4\,(2+\chi)(\sqrt{1+\chi})}{4\,(1+\chi)} - 4\,\xi^2 \tag{25}$$

It's evident from Eq. 24 and 25 that ε and δ are functions of χ and the damping ratio denoted by ξ. For a periodic result to the motion equation (Eq. 21), the $\varepsilon - \delta$ curve needs to align via a transition curve. Then, the variation limits of χ should be established since the Mathieu equation features a periodic solution.

3. The HPM for solving the motion equation

An analytical relation exists between a cracked beam's damping ratio and crack parameters. This division presents an analytical method for the free vibration of the supported beam. The initial conditions used for the solution of Eq. 21 are regarded as $z(0) = 1$ and $\dot{z}(0) = 0$. The initial conditions relate to the deformation of the equivalent mass from its equilibrium position by a distance of A, and the primary velocity of $-Ac/2m$.

As noted in the previous section, the Motion equation should have a periodic solution any time δ can be expressed in terms of ε as stated by Eq. 23. In Fig. 2, G_0 should be equal to 2.

In this letter, we apply the HPM to solve the discussed problem. The structure of the HPM is shown as follows:

$$(v,p) = L(v) - L(z_0) + pL(z_0) + p[N(v) - f(r)] = 0, \tag{26}$$

The notations $v(r,p)$: $\Omega \times [0,1] \to R$, L represents the linear, N represents the nonlinear part of the differential equation and $f(\tau)$is a known analytical function.

Considering Eq. 26 we have:

$$H(v,0) = L(v) - L(z_0) = 0,\ H(v,1) = L(v) + N(v) - f(r) = 0 \tag{27}$$

In that $p \in [0,1]$ is an embedding parameter and z_0 is the initial estimate that satisfies the B.C. By substituting Eq. 21 into Eq. 26, it becomes:

$$H(v,p) = [\frac{d^2v(\tau)}{d\tau^2} + 4\,\xi\,\frac{dv(\tau)}{d\tau} + [\delta + 4\,\xi^2]v(\tau) - L(z_0)] + pL(z_0) + 2\,p\varepsilon\,cos(2\,\tau)\,v(\tau)] = 0, \quad (28)$$

The procedure for the changes in p from 0 to unity is $v(\tau,p)$, which changing from z_0 to z_r. z is considered as:

$$v(\tau) = \sum_{i=0}^{\infty} v_i(\tau)p^i \quad (29)$$

The most accurate estimate for the solution is:

$$z(\tau) = \lim_{p\to 1} \sum_{i=0}^{\infty} v_i(\tau)p^i \quad (30)$$

Inserting Eqs. 23 and 29 into Eq. 28 yields:

$$H(v,p) = [\sum_{i=0}^{\infty} \ddot{v}_i(\tau)p^i + 4\,\xi \sum_{i=0}^{\infty} \dot{v}_i(\tau)p^i + [\sum_{i=0}^{\infty} G_i p^i + 4\,\xi^2] \sum_{i=0}^{\infty} v_i(\tau)p^i - L(z_0)] + pL(z_0) + [2\,\varepsilon\,cos(2\,\tau)] \sum_{i=0}^{\infty} v_i(\tau)p^i] = 0, \quad (31)$$

Assuming $L(z_0) = 0$ and simplification and rearranging based on powers of p-terms and setting the coefficients to each power of p equal to 0 would result in an infinite collection of differential equations as:

$$p^0: \ddot{v}_0(\tau) + 4\,\xi\dot{v}_0(\tau) + (4\,\xi^2 + 4)v_0(\tau) = 0, v_0(0) = 1, \dot{v}_0(0) = 0 \quad (32\text{-}1)$$

$$p^1: \ddot{v}_1(\tau) + 4\xi\dot{v}_1(\tau) + (4\xi^2 + 4)v_1(\tau) = (2\varepsilon - G_1 - 4\varepsilon\,cos^2(\tau))v_0(\tau), v_1(0) = 0,\ \dot{v}_1(0) = 0 \quad (32\text{-}2)$$

$$p^2: \ddot{v}_2(\tau) + 4\xi\dot{v}_2(\tau) + (4\xi^2 + 4)\,v_2(\tau) = (2\varepsilon - G_1 - 4\varepsilon\,cos^2(\tau))z_1(\tau) - G_2v_0(\tau), v_2(0) = 0, \dot{v}_2(0) = 0 \quad (32\text{-}3)$$

$$p^3: \ddot{v}_3(\tau) + 4\,\xi\dot{v}_3(\tau) + (4\xi^2 + 4)v_3(\tau) = (2\,\varepsilon - G_1 - 4\,\varepsilon\,cos^2(\tau))v_2(\tau) - G_2v_1(\tau) - G_3v_0(\tau), v_3(0) = 0, \dot{v}_3(0) = 0 \quad (32\text{-}4)$$

The infinite set outlined in Eq. 32 has been solved recursively. To derive solutions for this set of equations, certain conditions must be placed on G_i . The first part of this set provides the zero-order estimate for the solution:

$$v_0(\tau) = e^{-2\xi\tau}(A_0\,sin(2\tau) + B_0\,cos(2\tau)) \quad (33)$$

The constants $A_0$and B_0in Eq. 33 are assessed by applying the initial conditions. Solving Eq. 32-1 and taking into account suitable initial conditions, gives $v_0(\tau) = e^{-2\xi\tau}\,cos(2\tau)$. Using Eq. 32-2, we have

$$v_1(\tau) = \varepsilon e^{-2\xi\tau}\left(-\frac{1}{3} + \frac{1}{6}cos(2\tau) + \frac{1}{6}cos^2(2\tau) - \frac{1}{4}G_1\tau\,sin(2\tau)\right) \quad (34)$$

To meet the periodicity conditions for $v_0(\tau)$, G_1 is equal to zero. Henceforward, the answer to the second part of Eq. 32 is:

$$v_1(\tau) = \varepsilon e^{-2\xi\tau}\left(-\frac{1}{3} + \frac{1}{6}cos(2\tau) + \frac{1}{6}cos^2(2\tau)\right) \quad (35)$$

Knowing that $G_1 = 0$, and using Eq. 32-3, $v_2(\tau)$ is obtained in the following form:

$$v_2(\tau) = \frac{1}{288}e^{-2\xi\tau}(3\varepsilon^2\,cos^3(2\tau) + 8\varepsilon^2\,cos^2(2\tau) + 5\varepsilon^2\,cos(2\tau) + 30\left(\varepsilon^2 - \frac{12}{5}G_2\right)\tau\,sin(2\tau) - 16\,\varepsilon^2\right) \quad (36)$$

$v_2(\tau)$ will be periodic when the term's coefficient is set equal to zero, so $G_2 = 5/12\,\varepsilon^2$. Thus, similar procedures can be used; other equations of Eq. 32 can be solved recursively.

$$v_3(\tau) = \frac{1}{2880}e^{-2\xi\tau}(\varepsilon^3\,cos^4(2\tau) + 5\,\varepsilon^3\,cos^3(2\tau) + 29\,\varepsilon^3\,cos^2(2\tau) - 77\,\varepsilon^3\,cos(2\tau) - 720\,G_3\,\tau\,sin(2\tau) + 42\,\varepsilon^3), \quad G_3 = 0 \quad (37)$$

$$v_4(\tau) = \frac{1}{1658880}e^{-2\xi\tau}(12\,\varepsilon^4\,cos^5(2\tau) + 96\,\varepsilon^4\,cos^4(2\tau) + 1299\,\varepsilon^4\,cos^3(2\tau) - 5408\,\varepsilon^4\,cos^2(2\tau) - 16415\,\varepsilon^4\,cos(2\tau) - 22890\left(\frac{13824}{763}G_4 + \varepsilon^4\right)\tau\,sin(4\tau) + 20416\,\varepsilon^4), \quad G_4 = -\frac{763}{13824}\varepsilon^4 \quad (38)$$

$$v_5(\tau) = \frac{1}{116121600}e^{-2\xi\tau}(12\,\varepsilon^5\,cos^6(2\tau) + 140\varepsilon^5\,cos^5(2\tau) + 3335\,\varepsilon^5\,cos^4(2\tau) - 20685\,\varepsilon^5\,cos^3(2\tau) - 226585\,\varepsilon^5\,cos^2(2\tau) + 501113\,\varepsilon^5\,cos(2\tau) - 29030400\,G_5\tau\,sin(2\tau) - 257330\,\varepsilon^5), G_5 = 0 \quad (39)$$

Continuing with this process results in additional terms of $v_i(\tau)$, a few first terms will ensure suitable precision for the solution, and the other terms make a minor impact on the solution. By using a variable transformation $\tau = \omega_b t/2$ and $p \to 1$, the solution

for Eq. 19 in relations of ω_b at the actual time t is achieved:

$$z(t) = e^{-\frac{c}{2m}t}\Big[cos(\omega_b t) + \frac{1}{6}\varepsilon(cos^2(\omega_b t) + cos(\omega_b t) - 2) + \frac{1}{288}\varepsilon^2(3\,cos^3(\omega_b t) + 8\,cos^2(\omega_b t) + 5\,cos(\omega_b t) - 16) + \frac{1}{2880}\varepsilon^3(cos^4(\omega_b t) + 5\,cos^3(\omega_b t) + 29\,cos^2(\omega_b t) - 77\,cos(\omega_b t) + 42) + \frac{1}{1658880}\varepsilon^4\Big(12\,cos^5(\omega_b t) + 96\,cos^4(\omega_b t) + 1299\,cos^3(\omega_b t) - 5408\,cos^2(\omega_b t) - 16415\,cos(\omega_b t) + 20416 + \frac{1}{116121600}\varepsilon^5(12\,cos^7(\omega_b t) + 140\,cos^5(\omega_b t) + 3335\,cos^4(\omega_b t)\Big) - 20685\,cos^3(\omega_b t) - 226585\,cos^2(\omega_b t) + 501113\,cos(\omega_b t) - 257330 + \frac{1}{58060800}\varepsilon^6(72\,cos^7(\omega_b t) + 1152\,cos^6(\omega_b t) + 4224\,cos^5(\omega_b t)\Big) - 367968\,cos^4(\omega_b t) - 8571195\,cos^3(\omega_b t) + 30518176\,cos^2(\omega_b t) + 176434669\,cos(\omega_b t) - 198057152) + \dots.\Big] \quad (40)$$

, and

$$\delta = 4 + \frac{5}{12}\varepsilon^2 - \frac{763}{13824}\varepsilon^4 + \frac{1002401}{79626240}\varepsilon^6 - \frac{1669068401}{458647142400}\varepsilon^8 + \dots. \quad (41)$$

Eq. 41 has a clear physical interpretation. Eq. 22 shows δ , which is a function of the SDOF model parameters, breathing frequency, and the structural stiffness modifications caused by the crack. Also, Eq. (41) formulates δ in terms of ε for a periodic solution of D.E. (Eq. 21).

Thus, applying Eq. 25 alongside Eq. 41 establishes a relationship for the damping ratio of the fatigue-cracked beam based on its geometric dimensions, mechanical properties, and crack characteristics, as follows

$$\xi = \frac{1}{3317760}\frac{1}{1+\chi}(\sqrt{6}((1+\chi)(-917294284800 - 917294284800\chi - 191102976000\,\varepsilon^2 - 191102976000\,\varepsilon^2\chi + 25314508800\,\varepsilon^4 + 253145088000\,\varepsilon^4\chi - 5773829760\,\varepsilon^6 - 5773829760\,\varepsilon^6\chi + 1669068401\,\varepsilon^8 + 1669068401\,\varepsilon^8\chi + 229323571200\,\chi^2 + 917294284800\sqrt{1+\chi} + 458647142400\sqrt{1+\chi}\chi))^{1/2}) \quad (42)$$

where ε is a function of χ (See: Eq. 22). The Motion equation has an analytical and periodic solution only if δ and ε parameters of Eq. 21)are situated on the transition curves. An unbounded solution exists for any plane and location in the unstable region (highlighted sections in Fig. 2). Nonetheless, considering the cited crack's physical evidence, beam ε is always positive, and the associated transition curve $\delta - \varepsilon$ emanates from the point $\delta = 4$ on the δ axis. It is illustrated that when ε approaches zero, the precision of the asymptotic response will rise. Thus, utilizing Eq. 24, which illustrates the relationship between ε and χ, it is observed that when χ is less than 1.5, the value of ε will always be below unity. The formula between χ and the mechanical properties of the considered flexural fatigue-cracked beam takes the dimensionless form:

$$\chi = \frac{\Delta C}{C} = \frac{3\pi^5(1-\nu^2)}{4}\left(\frac{L_0}{L}\right)^2\left(\frac{h}{L}\right)g(\alpha) \quad (43)$$

Utilizing this dimensionless equation, χ can plot against the crack depth ratio $\alpha = a/h$, and the crack location ratio $\beta = L_0/L$ to establish the valid domain of the solution. The region of $\chi > 1.5$ is valid for the analytical solution. This method enables the derivation of the analytical solution for the free vibration response. Additionally, the beam's damping ratio can be computed based on the specified geometric dimensions, mechanical characteristics, and crack depth.

4. Results and discussion

Using the HPM outlined in section 3, this study investigates both the quantitative and qualitative parameters affecting the behavior of a fatigue-cracked beam. To compare the proposed method's results and the experimental findings reported in the reference [34], an aluminum pinned-supported with a length of 235 mm and a cross-sectional area of 7×23 mm^2 serves as a case example in this study. The material density and Young's modulus of elasticity of the beam are 2800 kg/m^3 and 72 GPa. As mentioned in section 2.2, the stiffness of a beam with a fatigue crack varies continuously over time as the beam vibrates, i.e., during each half-cycle of beam vibration, the stiffness of the beam transitions smoothly between the two extremes that represent a fully open crack and a fully closed crack case. Fig. 3 illustrates the change in stiffness overtime during a half-cycle vibration for a beam with a crack position ratio β = 0.2 and variable crack depth ratios of α. In this figure, the extreme values of the curve relate to entirely closed cases of the crack (i.e., the unaltered beam), and the lowest values relate to completely open cases of the crack. Additionally, this figure shows that a deeper crack leads to a broader range of stiffness variations, consequently decreasing the dominant frequency.

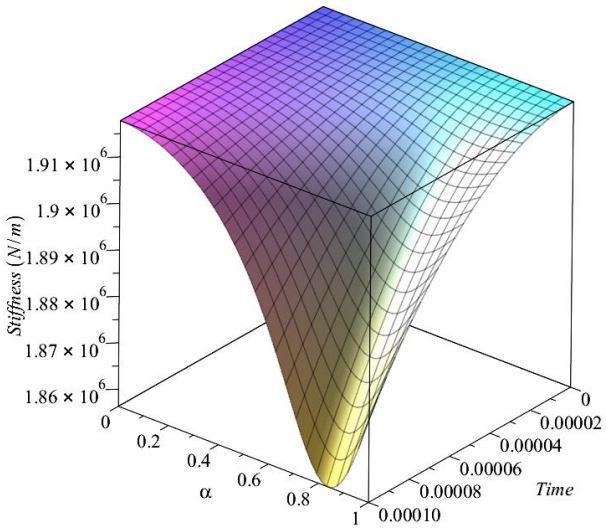

Fig. 3. The fatigue-Cracked beam's stiffness changes over time(s) with the position ratio for β = 0.2 and various crack depth ratios.

The recommended analytical method can assess a fatigue-cracked beam's free deformation and acceleration results for a specified crack depth and position. The computed free vibration responses of the fatigue-cracked beam for the crack parameters illustrated in Fig. 3 are presented in Figs. 4 and 5. In both scenarios, the initial deformation is z (0) = 1 cm. These figures indicate that greater crack depth results in a more significant decay of the fatigue-cracked beam's response. The emergence of the dominant frequency's super harmonics results from variations in the stiffness of the fatigue-cracked beam during vibration.

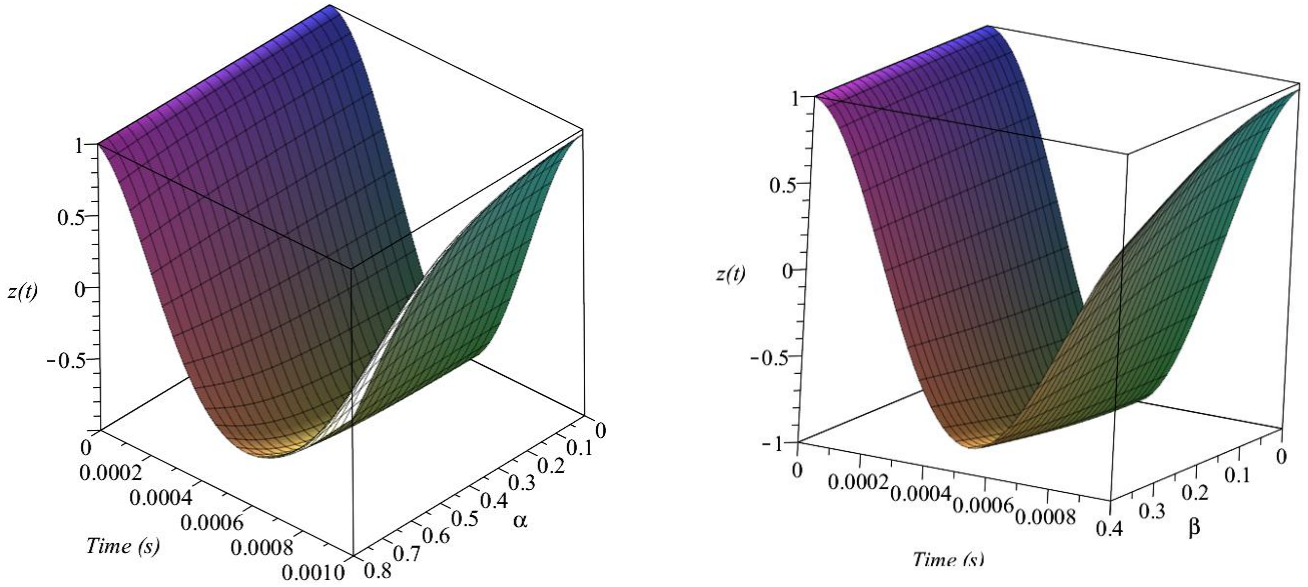

β = 0.2 **α=0.4**

Fig. 4. The deformation response of the beam with (a) a constant crack position ratio (β = 0.2) and varying crack depth ratios, and (b) a constant crack depth ratio (α = 0.4) and varying crack position ratios.

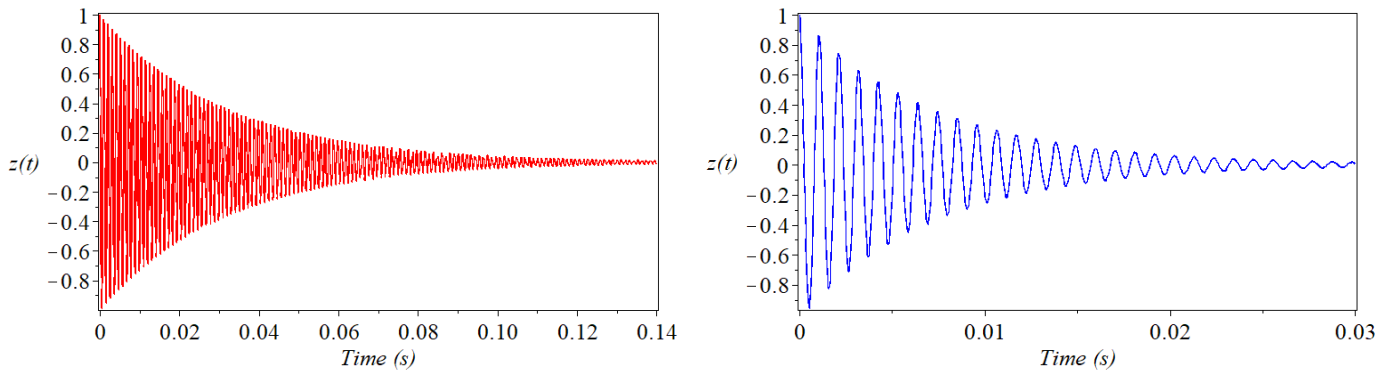

(a) (b)

Fig. 5. The beam deformation response of the crack position ratio β = 0.2 and dual crack depth ratios of (a) α=0.2, and (b) α=0.4.

One major advantage of the given analytical method is its capability to estimate the system's damping due to the crack. Fig. 6 illustrates how the damping factor varies with the crack position ratio at dissimilar crack depth ratios. The figure indicates that the system damping reaches its peak for a specific crack depth when the crack is situated at the beam's midpoint. Consequently, the

damping factor is responsive to the crack's depth and location.

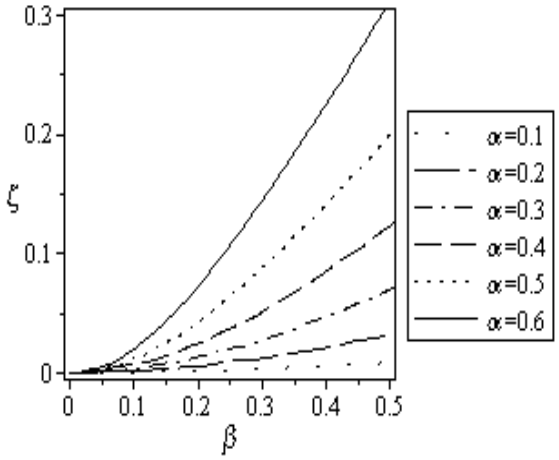

Fig. 6. Damping factor variation of the vibration flexural cracked beam concerning the crack position ratio for various crack depth ratios.

To verify the analytical solution for the beam for the crack parameters $\alpha = 0.4$ and $\beta = 0.2$, the motion equation is resolved numerically via the fourth-order Runge-Kutta technique, with the results presented in Table 1. The primary conditions match those used in the analytical case. The comparison of HPM and numerical results shows strong agreement between the analytical and numerical solutions. It's important to note that the beam's damping factor is not included in numerical methods; thus, an assumed value is necessary. In this context, some researchers have taken values of 0.01 and 0.15 for the damping factor in the vibration analysis of flexural fatigue-cracked beams. As previously mentioned, the system's damping relies on the crack parameters, and the damping factor for a fatigue-fractured beam changes based on crack depth and location. Consequently, the damping factor is derived from the suggested analytical method and applied in the numerical analysis to enhance the accuracy of the numerical method [21].

Table 1. Comparison of the free vibration response of the crack parameters $\beta = 0.2$ and $\alpha = 0.4$ measured from HPM and numerical model.

Time	Displacement (cm)		Velocity (cm/s)	
	Numerical result	(HPM)	Numerical result	(HPM)
0	1	1	0	0
0.001	0.796182	0.803836	2020.033	1907.988
0.005	-0.20705	-0.19625	2773.582	2796.619
0.01	-0.19011	-0.19387	-991.598	-965.217
0.05	8.49E-04	8.58E-04	3.231528	3.10251
0.1	4.32E-07	4.507453432 E-07	5.55E-03	5.446 E-03
0.5	8.90E-12	7.656194548 E-031	-1.07E-07	-5.1E-27
1	-9.84E-12	-9.7E-62	5.06E-08	-7.6E-57

To ensure a legitimate analytical closed-form solution, $\Delta C/C$ must be less than 1.5. Consequently, the shaded area defines the allowable variation limits for the crack parameters (see Fig. 7). The crack terms of the referenced beams are situated within the hatched area. Thus, the analytical solutions acquired are considered valid. To evaluate the accuracy of the results produced by the proposed analytical solution, a comparison is made with the experimental results presented by Chondros et al. [34]. The crack is situated at the center of the bending beam (with assumption $\beta = 0.5$); the suggested analytical method applies to both the breathing and the open crack models.

The solid curve in Fig. 8 illustrates how the fundamental frequency ratio changes for the transverse dynamic vibration of a pinned-supported beam with a breathing crack situated at the midpoint. This variation is plotted against the depth of the crack ratios. In Fig. 8, the experimental results reported by Chondros et al. [34]. The solid curve comparison with the experimental data shows that the proposed method's results agree with the experimental findings reported in the literature. Furthermore, this figure illustrates that the frequency decrease in the open crack mode for a specific crack location ratio is more significant than that in the breathing model. This finding has been established earlier [18].

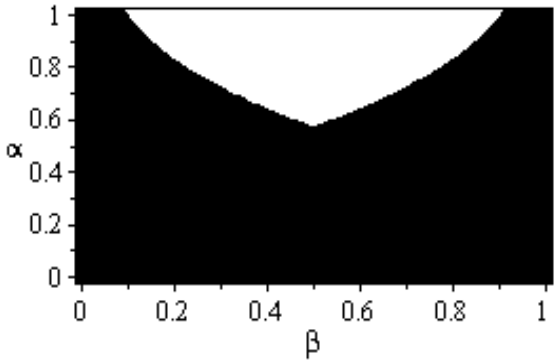

Fig. 7. The area of the flexural crack terms necessary for acquiring a legitimate analytical solution for the vibration analysis of an aluminum-pinned supported beam measuring 7 × 23 × 235 mm³.

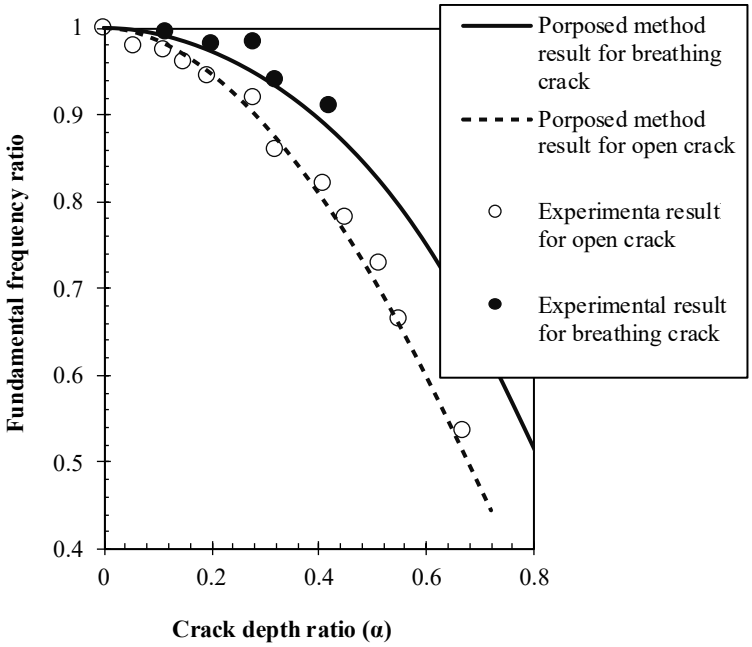

Fig. 8. The variation in the dominant frequency ratio of a cracked pinned-supported bending beam compared to the depth ratio for the crack in the position ratio β = 0.5.

5. Conclusion

This study introduces an analytical alternative novel technique for analyzing the vibrations of a flexural cracked beam. The cracked beam behaves as a nonlinear SDOF structure, with nonlinearity stemming from the crack's breathing behavior. The GE is addressed using the perturbation technique. The solution is valid across a broad spectrum of crack parameters, mechanical characteristics of the beam, and geometric dimensions. This approach estimates the cracked beam's damping ratio due to the crack's existence.

The findings reveal that the crack's depth and location influence the damping factor. Moreover, the super harmonics of the dominant frequency in the response spectra of the cracked beam illustrate its nonlinear dynamic behavior, potentially serving as an indicator of cracks in structural health monitoring applications.

A numerical method is employed alongside the proposed approach to confirm the analytical findings. The free vibration of the flexural cracked beam, calculated using the analytical approach at a specific crack depth and position, matches the numerical results. The outcomes confirm that the solution is consistent with the analytical numerical response.

To confirm the results, a plot of the fundamental frequency ratio against the crack depth ratio for a given crack location ratio is generated according to the breathing flexural crack model, juxtaposed with the experimental findings from the literature. The results indicate compatibility with similar experimental data.

Statements & declarations

Author contributions

Ali Asgari: Conceptualization, Investigation, Formal analysis, Software, Validation, Resources, Writing - Original Draft , Methodology, Writing - Review & Editing, Original Draft,.

Alireza Khabiri: Writing - Review & Editing.

Funding

Funding information is not available.

Declaration

The authors declare that they have no known competing financial interests or personal relationships that could have appeared to influence the work reported in this paper.

Data availability

Data will be made available on request.

References

[1] Khabiri, A., Asgari, A., Taghipour, R., Bozorgnasab, M., Aftabi-Sani, A., Jafari, H. Analysis of Fractional Euler-Bernoulli Bending Beams Using Green's Function Method. Alexandria Engineering Journal, 2024; 106: 312–327. doi:10.1016/j.aej.2024.07.023.

[2] Bahreini, A., Asgari, A., Khabiri, A., Taghipour, R. Analysis of Plane Multi-Span Frames with the Analytical Method of Force-Displacement Combination. Sharif Journal of Civil Engineering. doi:10.24200/j30.2024.64303.3318.

[3] Asgari, A., Ganji D. D., Davodi A. G. Extended tanh method and exp-function method and its application to (2+1)-dimensional dispersive long wave nonlinear equations. Journal of the Applied Mathematics, Statistics and Informatics, 2010; 6: 61–72.

[4] Ganguly, S. Methodologies for Modeling and Identification of Breathing Crack: A Review. MethodsX, 2023; 11: 102420. doi:10.1016/j.mex.2023.102420.

[5] Behvar, A., Haghshenas, M., Djukic, M. B. Hydrogen Embrittlement and Hydrogen-Induced Crack Initiation in Additively Manufactured Metals: A Critical Review on Mechanical and Cyclic Loading. International Journal of Hydrogen Energy, 2024; 58: 1214–1239. doi:10.1016/j.ijhydene.2024.01.232.

[6] Sangid, M. D. The Physics of Fatigue Crack Initiation. International Journal of Fatigue, 2013; 57: 58–72. doi:10.1016/j.ijfatigue.2012.10.009.

[7] Faverjon, B., Sinou, J. J. Identification of an Open Crack in a Beam Using an a Posteriori Error Estimator of the Frequency Response Functions with Noisy Measurements. European Journal of Mechanics, A/Solids, 2009; 28 (1): 75–85. doi:10.1016/j.euromechsol.2008.02.006.

[8] Lam, H. F., Ng, C. T., Veidt, M. Experimental Characterization of Multiple Cracks in a Cantilever Beam Utilizing Transient Vibration Data Following a Probabilistic Approach. Journal of Sound and Vibration, 2007; 305 (1–2): 34–49. doi:10.1016/j.jsv.2007.03.028.

[9] Chati, M., Rand, R., Mukherjee, S. Modal Analysis of a Cracked Beam. Journal of Sound and Vibration, 1997; 207 (2): 249–270. doi:10.1006/jsvi.1997.1099.

[10] Chondros, T. G. The Continuous Crack Flexibility Model for Crack Identification. Fatigue and Fracture of Engineering Materials and Structures, 2001; 24 (10): 643–650. doi:10.1046/j.1460-2695.2001.00442.x.

[11] Loya, J. A., Rubio, L., Fernández-Sáez, J. Natural Frequencies for Bending Vibrations of Timoshenko Cracked Beams. Journal of Sound and Vibration, 2006; 290 (3–5): 640–653. doi:10.1016/j.jsv.2005.04.005.

[12] Ke, L. L., Yang, J., Kitipornchai, S., Xiang, Y. Flexural Vibration and Elastic Buckling of a Cracked Timoshenko Beam Made of Functionally Graded Materials. Mechanics of Advanced Materials and Structures, 2009; 16 (6): 488–502. doi:10.1080/15376490902781175.

[13] Friswell, M. I., Penny, J. E. T. A simple nonlinear model of a cracked beam. In: Proceedings of the International Modal Analysis Conference; 1992 Feb 3–7; California (US).

[14] Sinha, J. K., Friswell, M. I., Edwards, S. Simplified Models for the Location of Cracks in Beam Structures Using Measured Vibration Data. Journal of Sound and Vibration, 2002; 251 (1): 13–38. doi:10.1006/jsvi.2001.3978.

[15] Kisa, M., Brandon, J. Effects of Closure of Cracks on the Dynamics of a Cracked Cantilever Beam. Journal of Sound and Vibration, 2000; 238 (1): 1–18. doi:10.1006/jsvi.2000.3099.

[16] Rytter A. Vibrational based inspection of civil engineering structures [PhD thesis]. Aalborg (DK): University of Aalborg; 1993.

[17] Abraham, O. N. L., Brandon, J. A. The Modelling of the Opening and Closure of a Crack. Journal of Vibration and Acoustics, Transactions of the ASME, 1995; 117 (3): 370–377. doi:10.1115/1.2874463.

[18] Cheng, S. M., Wu, X. J., Wallace, W., Swamidas, A. S. J. Vibrational Response of a Beam with a Breathing Crack. Journal of Sound and Vibration, 1999; 225 (1): 201–208. doi:10.1006/jsvi.1999.2275.

[19] Ariaei, A., Ziaei-Rad, S., Ghayour, M. Vibration Analysis of Beams with Open and Breathing Cracks Subjected to Moving Masses. Journal of Sound and Vibration, 2009; 326 (3–5): 709–724. doi:10.1016/j.jsv.2009.05.013.

[20] Douka, E., Hadjileontiadis, L. J. Time-Frequency Analysis of the Free Vibration Response of a Beam with a Breathing Crack. NDT and E International, 2005; 38 (1): 3–10. doi:10.1016/j.ndteint.2004.05.004.

[21] Loutridis, S., Douka, E., Hadjileontiadis, L. J. Forced Vibration Behaviour and Crack Detection of Cracked Beams Using Instantaneous Frequency. NDT and E International, 2005; 38 (5): 411–419. doi:10.1016/j.ndteint.2004.11.004.

[22] Zhang, W., Testa, R. B. Closure Effects on Fatigue Crack Detection. Journal of Engineering Mechanics, 1999; 125 (10): 1125–1132. doi:10.1061/(asce)0733-9399(1999)125:10(1125).

[23] Bovsunovsky, A. P., Surace, C. Considerations Regarding Superharmonic Vibrations of a Cracked Beam and the Variation in Damping Caused by the Presence of the Crack. Journal of Sound and Vibration, 2005; 288 (4–5): 865–886. doi:10.1016/j.jsv.2005.01.038.

[24] Curadelli, R. O., Riera, J. D., Ambrosini, D., Amani, M. G. Damage Detection by Means of Structural Damping Identification. Engineering Structures, 2008; 30 (12): 3497–3504. doi:10.1016/j.engstruct.2008.05.024.

[25] Dimarogonas, A. D. Vibration of Cracked Structures: A State of the Art Review. Engineering Fracture Mechanics, 1996; 55 (5): 831–857. doi:10.1016/0013-7944(94)00175-8.

[26] Rezaee, M., Hassannejad, R. Free Vibration Analysis of Simply Supported Beam with Breathing Crack Using Perturbation Method. Acta Mechanica Solida Sinica, 2010; 23 (5): 459–470. doi:10.1016/S0894-9166(10)60048-1.

[27] Reta, A. K., Taube, C., Morgenthal, G. Structural Condition Assessment of Cracked RC Beams Based on Digital Crack Measurements. Engineering Structures, 2025; 323: 119211. doi:10.1016/j.engstruct.2024.119211.

[28] Meiramov, D., Ju, H., Seo, Y., Lee, D. Correlation between Deflection and Crack Propagation in Reinforced Concrete Beams. Measurement: Journal of the International Measurement Confederation, 2025; 240: 115527. doi:10.1016/j.measurement.2024.115527.

[29] Dimarogonas, A. D., Paipetis, S. A. Analytical Methods in Rotor Dynamics.; Springer Science & Business Media: Dordrecht, Netherlands, 1983; doi:10.1007/978-94-007-5905-3.

[30] Chondros, T. G., Dimarogonas, A. D., Yao, J. A Continuous Cracked Beam Vibration Theory. Journal of Sound and Vibration, 1998; 215 (1): 17–34. doi:10.1006/jsvi.1998.1640.

[31] Kranz, R. L. Microcracks in Rocks: A Review. Tectonophysics, 1983; 100 (1–3): 449–480. doi:10.1016/0040-1951(83)90198-1.

[32] Shaw, S. Vibrations in mechanical systems: analytical methods and applications. Berlin (DE): Springer Science & Business Media; 1989. Vol. 31. doi:10.1137/1031116.

[33] Clough, R. W., Penzien, J. Dynamics of structures. Berkeley (US): Computers & Structures, Inc.; 1975.

[34] Chondros, T. G., Dimarogonas, A. D., Yao, J. Vibration of a Beam with a Breathing Crack. Journal of Sound and Vibration, 2001; 239(1): 57–67. doi:10.1006/jsvi.2000.3156.

Civil Engineering and Applied Solutions

Research Article

journal homepage: ceas.journals.umz.ac.ir

CEAS Civil Engineering and Applied Solutions

Damage Identification in Truss Structures Using a Hybrid PSO-HHO Algorithm with Selective Natural Frequencies and Mode Shape

Sayyed Hadi Alavi [a], Amirhossein Pilehvaran [a], Mohammadreza Mashayekhi [a*]

[a] *Civil Engineering Department, K.N. Toosi University of Technology, Tehran, Iran*

ARTICLE INFO

Keywords:
Structural damage detection
Modal parameters
Hybrid PSO-HHO algorithm
Inverse problem

Article history:
Received 25 May 2025
Accepted 13 June 2025
Available online 1 July 2025

ABSTRACT

Structural damage can be detected non-destructively by comparing the dynamic characteristics of a structure before and after a major event. Optimization techniques are effective tools for damage identification using structural dynamic properties, as the problem is formulated and solved inversely. To achieve this, the damage levels in each element are treated as decision variables. The objective is to fine-tune these variables so that the model's response closely aligns with the experimentally observed dynamic characteristics of the damaged structure. This study proposes a hybrid Particle Swarm optimization- Harris Hawks optimization algorithm for damage detection in truss structures based on dynamic structural responses. To evaluate the effectiveness of the proposed method, two case study of planar truss is considered as a numerical examples. The results highlight the importance of incorporating modal parameters to accurately identify the damage scenario. The results demonstrate that the hybrid algorithm significantly outperforms the individual algorithms in accurately detecting structural damage.

1. Introduction

Structures may sustain damage during their service life due to various factors, including corrosion, deterioration, excessive loading, and construction errors [1]. Damages may obvious as changes in the structural stiffness or effective mass, potentially leading to disruptions in the structural performance. Proper inspection, monitoring, and maintenance of structures are essential to ensure economic efficiency and promote sustainability in engineering [2,3]. Damage detection is considered the initial stage of a broader process known as damage identification [4]. Non-destructive damage detection methods identify structural damage without causing damage to the structure, utilizing its dynamic characteristics. Compared to destructive techniques, these methods are safer, more cost-effective, and better suited for continuous structural monitoring [5]. Non-destructive methods are primarily implemented through analytical approaches. For years, researchers have been investigating non-destructive techniques for damage identification. In general, when a structural member is damaged, the resulting changes directly influence the stiffness matrix of the structure, leading to alterations in its vibrational behavior [6]. For this reason, one of the effective approaches in non-destructive structural damage identification is to examine changes in the dynamic properties of the structure by utilizing natural frequencies and mode shapes [7,8]. On the other hand, various structural responses can be used as damage indicators, but modal parameters have the advantage of being independent of external excitation [9].

The first studies on damage identification based on monitoring changes in natural frequencies are conducted by Adams et al. [10,11]. They found that natural frequencies are highly dependent on the overall stiffness and mass distribution of the structure; therefore, even minor damages can cause measurable changes in these frequencies. Moreover, modal behavior provides more detailed information about the damage distribution, especially when frequency changes alone are insufficient to pinpoint the exact

* Corresponding author.
E-mail addresses: m.mashayekhi@kntu.ac.ir (M. Mashayekhi).

https://doi.org/ 10.22080/ceas.2025.29333.1016
ISSN: 3092-7749/© 2025 The Author(s). Published by University of Mazandaran.
This article is an open access article distributed under the terms and conditions of the Creative Commons Attribution (CC-BY) license (https://creativecommons.org/licenses/by/4.0/deed.en)
How to cite this article: Alavi, S. H., Pilehvaran, A., Mashayekhi, M. Damage Identification in Truss Structures Using a Hybrid PSO-HHO Algorithm with Selective Natural Frequencies and Mode Shape. Civil Engineering and Applied Solutions. 2025; 1(2): 55–73. doi:10.22080/ceas.2025.29333.1016.

location of the damage [12,13]. Extensive research has been conducted to detect structural damage using various indicators derived from dynamic characteristics [14–18]. Among these indicators are methods based on modal data correlation, parameter estimation techniques [19], frequency response functions [20], and geometric transfer matrices [21].

Non-destructive damage identification methods in structures are typically formulated as inverse problems and addressed through two main approaches: closed-form (analytical) solutions and optimization techniques. The closed-form solutions, which rely on precise mathematical relationships, are suitable for simple structures and noise-free data [22]. However, for complex structures or data contaminated with noise, optimization methods are preferred due to their flexibility and ability to handle uncertainties [23,24]. The general approach of optimization methods involves minimizing the discrepancy between the actual structural response and the response predicted by the optimization model. Sahu and Maity [25] investigated the impact of damage on the static behavior of structures using a neuro-genetic algorithm. In various studies, different optimization algorithms have been employed together with modal analyses of structures for damage identification [26–28]. Kaveh and Zolghadr [9] investigated and evaluated the damage present in truss structures under both two-dimensional and three-dimensional conditions using a population-based algorithm.

In this study, a hybrid metaheuristic algorithm is proposed for damage identification in truss structures using an inverse optimization approach. The objective function is designed to compare the dynamic characteristics of the intact (undamaged) structure with those of the structure under various damage scenarios. Initially, the dynamic characteristics of the intact structure are obtained through structural analysis. Then, by reducing the stiffness in certain truss members, possible damage scenarios are simulated. For each scenario, the dynamic response is computed, and the objective function quantifies the discrepancy between the dynamic characteristics such as natural frequencies and mode shapes of the intact and damaged structures. The metaheuristic optimization algorithm iteratively searches for the damage scenario that minimizes this discrepancy, effectively identifying the most probable location and extent of the damage. This method enables an efficient and automated damage identification process without the need for direct damage measurements, relying solely on changes in the dynamic behavior of the structure. The remainder of the paper is organized as follows: Section 2 presents the damage identification formulation. Section 3 describes the proposed metaheuristic algorithm. Section 4, presented the optimization formulation of this study. Section 5, described the methodology of damage detection with hybrid optimization algorithms. Section 6 presents a structural case study to evaluate the efficiency of the proposed method. Section 7 discusses the results of the case study, in Section 8 discusses the limitation of this study, and finally, Section 9 provides the conclusions of the research.

2. Modal-based damage identification in truss structures

In the term of structural health monitoring, damage identification is modeled as an optimization problem aimed at detecting changes in dynamics structural parameters such as natural frequencies, mode shape, particularly reductions in member stiffness. These changes lead to observable variations in dynamic properties such as natural frequencies and mode shapes. In this section, a concise formulation for structural damage identification based on changes in natural frequencies is presented. The analysis process begins with a review of the displacement-based finite element equations.

2.1. Structural dynamic equation

The dynamic equation of motion for an undamped multi-degree-of-freedom system is expressed in Eq. 1:

$$[M]\{\ddot{x}\} + [K]\{x\} = 0 \tag{1}$$

where K is the stiffness matrix and M is the mass matrix, while x is the displacement vector corresponding to the dynamic problem. For clarity in expressing the finite element terms, a truss structure composed of n elements is considered as the system in this study. In finite element modeling of truss structures, each member is idealized as a two-node bar element that is subjected only to axial forces. This method follows a displacement-based approach, in which the overall structural response is assembled from the behavior of individual elements. Accordingly, the equations corresponding to the dynamic characteristics of the truss structure are presented in following. For a bar element with length L, cross-sectional area A, and Young's modulus E, the stiffness matrix in the local coordinate system is defined by Eq. 2 [29].

$$[k_e] = \frac{AE}{L}\begin{bmatrix} 1 & -1 \\ -1 & 1 \end{bmatrix} \tag{2}$$

Assuming a uniform mass distribution along the member, the mass matrix in the local coordinate system is defined as shown in Eq. 3.

$$[m_e] = \frac{\rho AL}{6}\begin{bmatrix} 2 & 1 \\ 1 & 2 \end{bmatrix} \tag{3}$$

For an element in a two-dimensional structure, the structural properties are transformed from the local coordinate system to the global coordinate system using the transformation matrix T, as defined in the Eq. 4.

$$[T] = \begin{bmatrix} C & S & 0 & 0 \\ -S & C & 0 & 0 \\ 0 & 0 & C & S \\ 0 & 0 & -S & C \end{bmatrix} \tag{4}$$

where C and S represent $cos\alpha$ and $sin\alpha$, respectively. The transformed stiffness and mass matrices in the global coordinate system are then obtained through Equations 5 and 6, respectively.

$$[K] = [T]^T.[k_e].[T] \tag{5}$$

$$[M] = [T]^T.[m_e].[T] \tag{6}$$

2.2. Damage formulation

The modal properties of the undamaged structure are obtained by solving the eigenvalue problem. The Eq. 7 is formulated based on the dynamic model of the structure in its free-vibration state, without incorporating any damage.

$$[K]\{\varphi_i\} - \omega_i{}^2[M]\{\varphi_i\} = \{0\} \tag{7}$$

where ω_i denotes the ith natural frequency, and ϕ_i represents the corresponding mode shape. These parameters characterize the undamaged modal properties of the structure.

Within the concept of inverse problem-based damage identification, each structural member is typically assigned a damage index that reflects its health condition and quantifies the potential stiffness reduction due to damage. This index, typically denoted by α_i, takes a value between zero and one, where zero indicates a completely healthy member and one corresponds to a fully damaged member. In this study, the stiffness matrix is modified to account for the effect of damaged members and is reformulated accordingly, as presented in Eq. 8

$$[K^d] = \sum_{i=1}^{Ele}(1-\alpha_i).[K_i] \tag{8}$$

To incorporate structural damage, the global stiffness matrix K is replaced by a modified stiffness matrix K^d (see Eq. 9), which reflects the stiffness reduction caused by damage. It is assumed that the mass matrix M remains unaffected by the damage [30].

$$[K^d]\{\varphi_j^d\} - \omega_j^{d\,2}[M]\{\varphi_j^d\} = \{0\} \tag{9}$$

where ω_j and ϕ_j correspond to the jth natural frequency and its associated mode shape of the damaged structure. This eigenvalue equation determines the natural frequencies and mode shapes of the damaged structure, which are utilized in the damage identification process. The process of frequency and mode shape variation due to damage is illustrated schematically in the Fig. 1.

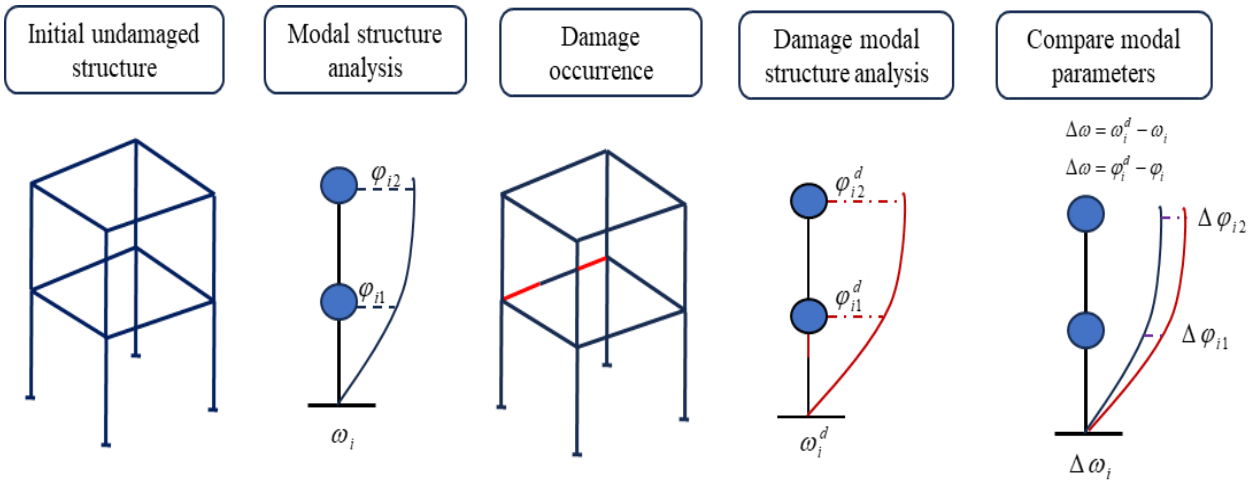

Fig. 1. Schematic representation of frequency and mode shape variations due to structural damage.

3. Optimization approach

In structural damage identification through inverse problem solving, the objective function is typically formulated based on the difference between the observed structural responses and those predicted by the model [31]. This approach typically presents a complex landscape with numerous local minima and multiple global optimal solutions [32]. Therefore, an effective solution to this inverse problem necessitates the use of a robust optimization algorithm capable of thoroughly and efficiently exploring the search space to accurately identify the most probable damage configuration. In recent years, metaheuristic algorithms have been widely employed for structural damage identification [33–35]. Inspired by natural phenomena such as evolution, swarm behavior, or physical laws, these algorithms exhibit strong global search capabilities and are less susceptible to the challenges posed by the non-convex nature of the objective function. Their ability to effectively handle discrete or continuous variables, noisy data, and complex search spaces makes metaheuristic algorithms particularly well-suited for solving inverse problems related to structural damage identification [36]. In this study, a hybrid metaheuristic algorithm combining particle swarm optimization and the harris hawks

optimization algorithm is proposed. First, the structures of each base algorithms are reviewed, and subsequently, the hybrid algorithm is presented.

3.1. Particle swarm optimization (PSO) algorithm

The PSO is a population-based metaheuristic algorithm inspired by the social behavior of animals searching for food [37]. In this algorithm, each particle represents a potential solution and navigates through the search space by updating its position based on its own experience and the experience of neighboring particles. Each particle possesses both a position and a velocity, and its movement is influenced by personal experience (its own best previous position) and social experience (the best position found by the entire swarm). In each iteration, the velocity of a particle is updated based on its personal best position and the global best position found by the swarm. Subsequently, the particle's new position is determined [38,39]. Through repeated iterations, the particles gradually converge toward optimal regions of the search space. The general steps of the PSO algorithm can be summarized as follows:

1. Initially, the position and velocity of each particle are randomly initialized within the defined bounds of search space, as expressed in Eq. 10.

$$\begin{aligned} x_i^{(0)} &= x_{min} + r_1.(x_{max} - x_{min}) \\ v_i^{(0)} &= v_{min} + r_2.(v_{max} - v_{min}) \end{aligned} \tag{10}$$

   The variables r_1 and r_2 are uniformly distributed random numbers in the range [0, 1]. The subscripts *min* and *max* denote the lower and upper bounds of the search space for the particle's position *x* and velocity *v,* respectively.

2. The objective function is evaluated for each particle, and both the personal best position and the global best position are updated accordingly.

3. The velocity of each particle is updated based on three components: momentum, the tendency toward its own best-known position (P_i), and the tendency toward the best-known position of the entire swarm (P_G), according to the Eq. 11. Using the updated velocity, the position of each particle is updated according to the following Eq. 12.

$$v_i^{(t+1)} = \omega.v_i^{(t)} + c_1.r_1.(P_i - x_i^{(t)}) + c_2.r_2.(P_G - x_i^{(t)}) \tag{11}$$

$$x_i^{(t+1)} = x_i^{(t)} + v_i^{(t+1)} \tag{12}$$

4. In each iteration, if a particle's current objective function value is better than its personal best, its best-known position is updated accordingly. Similarly, if the P_G improves, it is also updated. This process continues until a stopping criterion is met either reaching the maximum number of iterations or observing no significant improvement in the global best over several consecutive iterations [40]. Further details of the PSO algorithm are presented in [41,42].

3.2. Harris hawks optimization (HHO) algorithm

The HHO algorithm is a bio-inspired metaheuristic approach that draws inspiration from the collaborative hunting tactics of harris' hawks, introduced by Heidari et al. in 2019 [43]. These birds employ adaptive, group-based strategies that respond dynamically to prey movements and environmental factors. The HHO replicates these behaviors through an iterative process that effectively balances global exploration with local exploitation using probabilistic and adaptive techniques. By modeling hunting stages such as sudden ambushes and varied besieging maneuvers, the algorithm navigates complex search spaces to identify optimal solutions. Owing to its flexibility, robustness, and ease of implementation, the HHO has been successfully applied to a wide range of optimization problems in engineering and science. The main step of the HHO algorithm described in following.

1. Generate an initial population of *n* hawks, each representing a solution vector in a search space. Each variable is randomly initialized within its bounds, as expressed in Eq. 13:

$$x_i^{(j)} = x_{min}^{(j)} + r.\left(x_{max}^{(j)} - x_{min}^{(j)}\right) \tag{13}$$

   The variables *r* is random number uniformly distributed in the range [0, 1]. The subscripts *min* and *max* denote the lower and upper bounds of the search space for the hawk's position *x.*

2. After initializing the population, the algorithm evaluates each hawk's fitness and selects the best one (with the lowest objective value) as the rabbit (i.e., the current best solution). This best solution guides the movement of the rest of the hawks and is updated whenever a better solution is found during the iterations.

3. The HHO algorithm adjusts its search based on the prey's escape energy, defined by Eq. 14.

$$E = 2E_0\left(1 - \frac{t}{T}\right) \tag{14}$$

where E_0 in range -1 to 1, is the initial energy, t is the current iteration, and T is the maximum iterations. If $|E| \geq 1$, the HHO algorithm explores broadly by using Eq. 15.

$$x_{t+1} = \begin{matrix} x_{rand} - \alpha_1 |x_{rand} - 2\alpha_2 x_t| & q \geq 0.5 \\ x_{rabbit} - \bar{x} - \alpha_3 (lB + \alpha_4 (uB - lB)) & q < 0.5 \end{matrix} \quad (15)$$

where x_{rand} is a randomly selected hawk, $\bar{x}$ is the average position of hawks, and α_i, q are random numbers. In $|E| < 1$, the hawks switch to exploitation with different strategies depending on E a random number α. In this phase, for soft besiege ($|E| \geq 0.5$ and $\alpha \geq 0.5$) and hard besiege ($|E| < 0.5$ and $\alpha \geq 0.5$), using Eqs. 16 and 17, respectively.

$$x_{t+1} = \Delta x - E.|J.x_{rabbit} - x_t|, \Delta x = x_{rabbit} - x_t \quad (16)$$

$$x_{t+1} = x_{rabbit} - E.|\Delta x| \quad (17)$$

4. After reaching the maximum iteration T, return the best solution X_{rabbit} as the optimal result. More detail of the HHO algorithms is expressed in [44].

3.3. Hybrid metaheuristic optimization algorithm PSO-HHO

The hybrid PSO-HHO algorithm integrates the strengths of both methods to address complex optimization problems effectively. The PSO's rapid convergence and robust global search complement HHO's adaptive strategies, which balance exploration and exploitation [45]. This hybridization mitigates PSO's tendency to get trapped in local optima by leveraging HHO's diverse hunting mechanisms [46], such as surprise pounce and Levy flight-based jumps, while enhancing HHO's slower convergence in high-dimensional problems through PSO's collective dynamics. By integrating these features, the hybrid algorithm achieves improved efficiency, stability, and solution quality in multimodal optimization tasks.

The hybrid PSO-HHO algorithm integrates PSO and HHO by dividing the population into two interacting subgroups to optimize complex problems. The PSO subgroup rapidly explores the search space using collective particle dynamics, updating positions based on individual and global best solutions. Meanwhile, the HHO subgroup refines solutions through adaptive hunting strategies, such as surprise pounce and dynamic besieging, focusing on precise exploitation. Interaction occurs iteratively: PSO shares its top-performing solutions with HHO to enhance local search precision, while HHO's best solutions guide PSO's global exploration by updating its reference points [47]. A probabilistic crossover mechanism blends solutions from both subgroups to maintain diversity and prevent premature convergence. This cooperative framework leverages PSO's fast global search to accelerate HHO's slower convergence in high-dimensional spaces. In turn, HHO's adaptive strategies help PSO escape local optima, resulting in improved solution accuracy, robustness, and efficiency for multimodal optimization tasks [48]. The Fig. 2 provides an overview of the hybrid algorithm, illustrating the interactions between PSO and HHO algorithm.

4. Optimization formulation

This section addresses the key aspects of applying the proposed optimization algorithm to structural damage identification. The formulation includes the definition of decision variables, the specification of problem constraints, and the construction of the objective function that are fundamental components of any optimization process. The decision variables in this study are defined as stiffness reduction factors for each structural element, resulting in a total variable count equal to the number of elements in the model. The optimization problem is formulated as an unconstrained problem, with no additional constraints applied to the decision variables or the solution space. The primary objective is to minimize the discrepancy between the dynamic response obtained from the computational model and the response measured from the actual (possibly damaged) structure. This discrepancy is quantitatively represented through an objective function. To this end, the objective function is defined as $f(\alpha)$, which evaluates the difference between the computed and measured modal parameters. This function typically consists of two main components:

1. Frequency difference term: this component evaluates the relative difference between the natural frequencies computed from the numerical model and those measured from the damaged structure, as expressed by the Eq. 18:

$$f_1(\alpha) = \sum_{i=1}^{n_f} \left(\frac{\omega_i^d - \omega_i}{\omega_i}\right) \quad (18)$$

2. Mode shape difference term: this component quantifies the discrepancy between the measured and computed mode shapes as expressed in Eq. 19. Finally, the objective function is computed as a weighted combination of the previously defined components, as expressed in the Eq. 20.

$$f_2(\alpha) = \sum_{i=1}^{n_f} \sum_{j}^{n} \left(\frac{\varphi_{(i,j)}^d - \varphi_{(i,j)}}{\varphi_{(i,j)}}\right) \quad (19)$$

$$f(\alpha) = f_1(\alpha) + f_2(\alpha) \quad (20)$$

3. wehrer n_f and n are representing the number of modes and the number of degrees of freedom, respectively. The objective function is formulated to assess the degree of agreement between the response of the damaged structure and that predicted

by the assumed damage scenario. The aim of the optimization process is to identify the damage scenario that results in the smallest discrepancy from the actual behavior of the damaged structure. A lower objective function value reflects a closer match between the simulated scenario and the true structural response. This process involves repetitive iterations to achieve minimization. The next section introduces the methodology of damage detection based proposed hybrid metaheuristic algorithm used in this study.

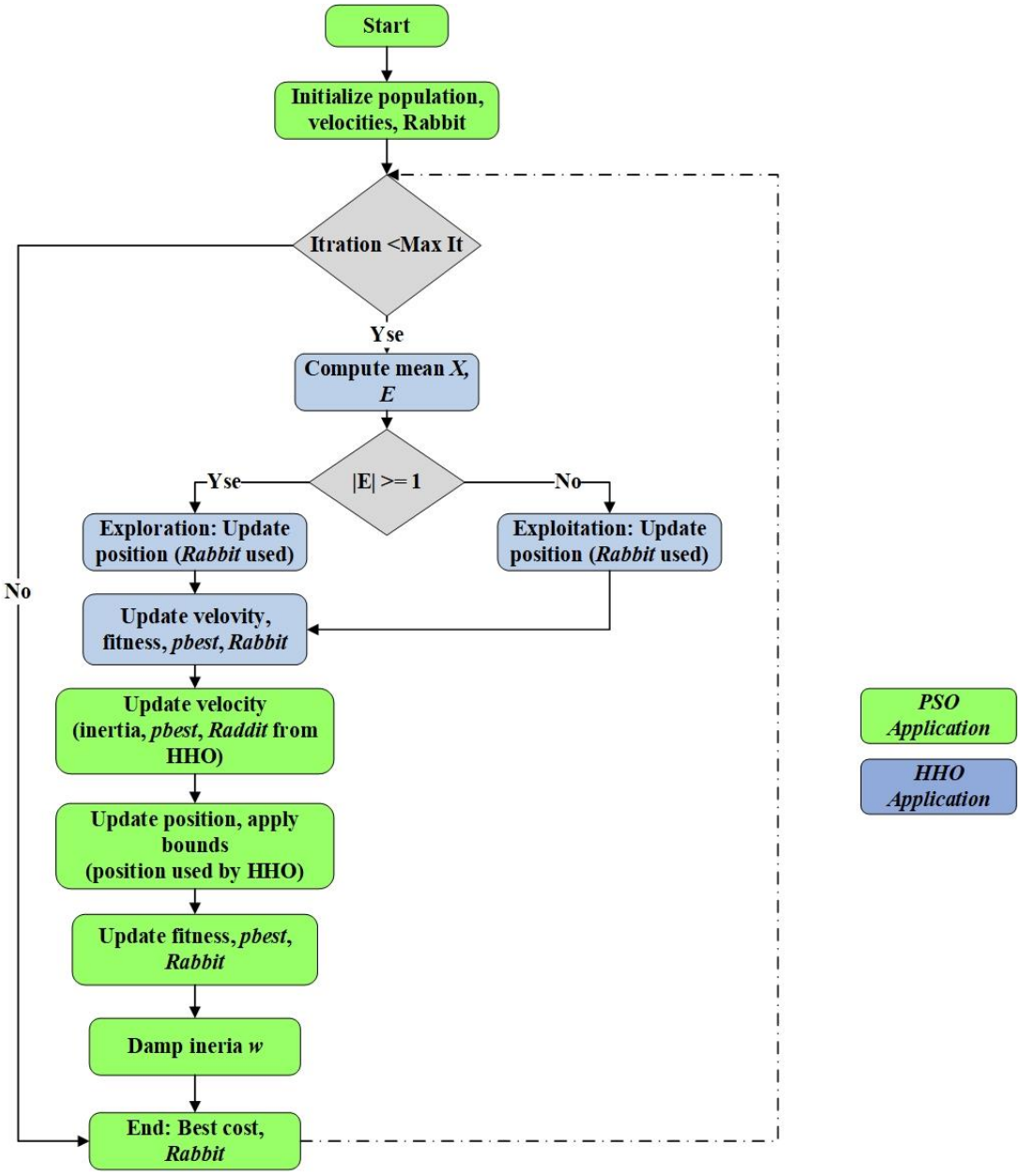

Fig. 2. Flowchart of the hybrid PSO-HHO algorithm.

5. Proposed framework for detecting structural damage

In this research, structural damage is identified and evaluated by leveraging principles related to the dynamic response of the system. Techniques based on vibration analysis rely on the premise that a structure's dynamic characteristics are inherently linked to its physical properties. Alterations in key structural matrices lead to observable variations in natural frequencies and mode shapes. This relationship forms the basis for damage detection, which can be approached by defining an optimization problem. As discussed in the preceding sections, the aim is to reduce the difference between the dynamic behavior represented by the damaged model and that observed in the experimental data, which forms the basis for defining the objective of the analysis.

The initial phase of the proposed approach involves modeling of a finite element model that reflects the intact state of the structure. The damaged structural model is simulated by reducing the stiffness in the basic structural members through the stiffness matrix. In this framework, for second phase, the optimization variables are defined as stiffness reduction coefficients assigned to individual structural elements, with the total number of variables corresponding to the number of elements within the model. The parameters selected for formulating the objective function should exhibit high sensitivity to structural damage. Accordingly, the objective function is formulated based on a combination of the structure's modal properties, namely natural frequencies and mode shapes. In the third phase, the dynamic parameters corresponding to the damaged condition must be obtained experimentally. Each

damage scenario is characterized by a set of affected elements and their associated levels of damage. Choosing and setting up the optimization algorithm is key for effective damage detection. In this study, a hybrid PSO-HHO algorithm is employed to leverage the complementary strengths of both algorithms. The initial population is generated using heuristic strategies to effectively explore the search space, focusing on potential damage scenarios with varying severity. The hybrid algorithm iteratively updates candidate solutions, ultimately selecting the best-performing solution as the damage identification result. The identified damage scenario includes all elements exhibiting damage levels exceeding a predefined threshold, while elements with lower damage values are treated as undamaged. The hybrid PSO-HHO algorithm is executed multiple times, and the solution corresponding to the lowest objective function value is selected as the most representative damage scenario. The step-by-step process of the proposed damage detection methodology presented in this study is illustrated in Fig. 3.

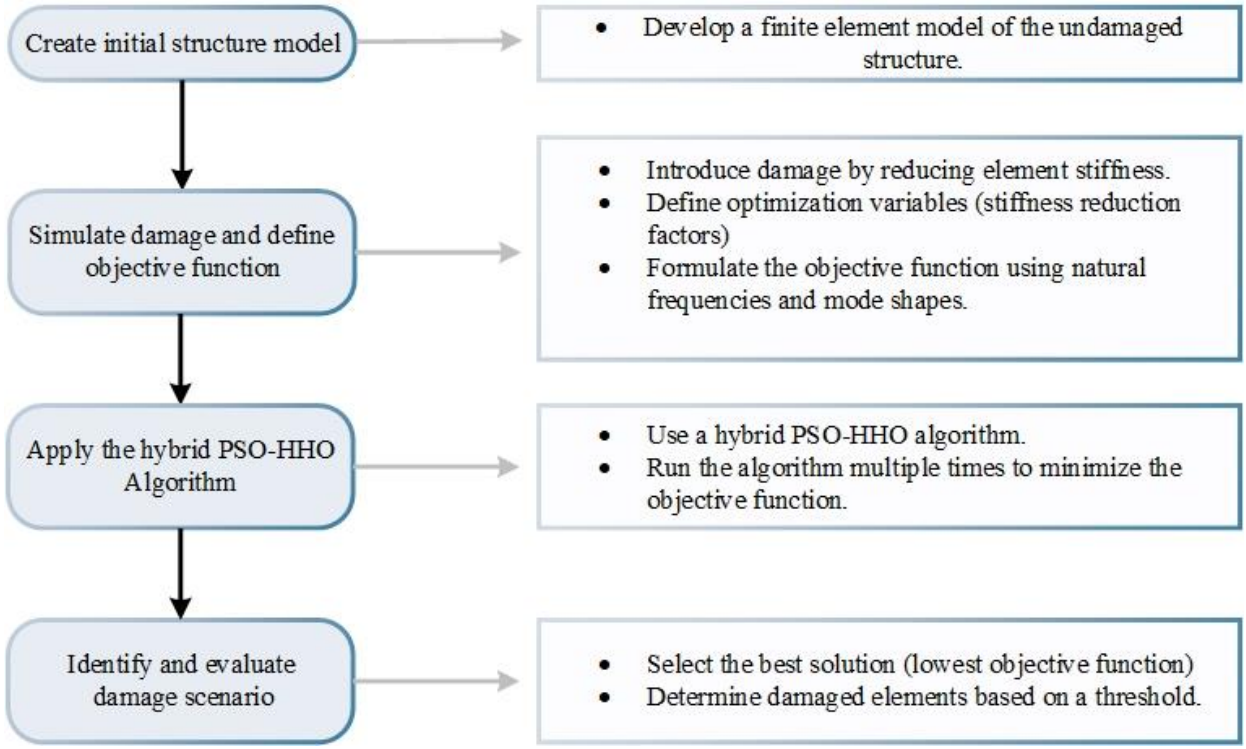

Fig. 3. Flowchart of the proposed damage detection method using a hybrid PSO-HHO algorithm.

6. Proposed examples

This section provides numerical simulations to evaluate the effectiveness of the proposed hybrid PSO-HHO algorithm in identifying structural damage within 2D truss systems. Since the damage identification algorithm is implemented based on the behavior of truss structures, two benchmark truss case studies are considered in this section. The first case involves a 15-element planar truss, as illustrated in Fig. 4, based on the model presented by Laier and Villalba [49]. In terms of degrees of freedom, all nodes except Node 1 and Node 5 have two translational degrees of freedom in the 2D plane. Node 1 is constrained in one direction and therefore retains only a single degree of freedom. In total, the truss system comprises 13 degrees of freedom. Both vertical and horizontal elements have a length of 1 meter.

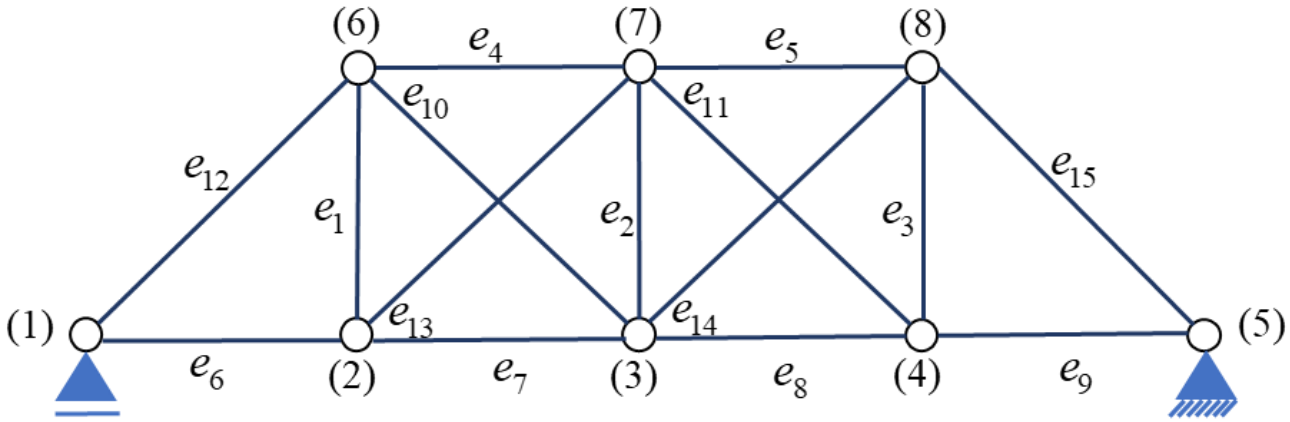

Fig. 4. Schematic of the first case study.

The second case study is an 11-member planar truss structure introduced by Russell Hibbeler, as shown in Fig. 5, with specific constraint [50].

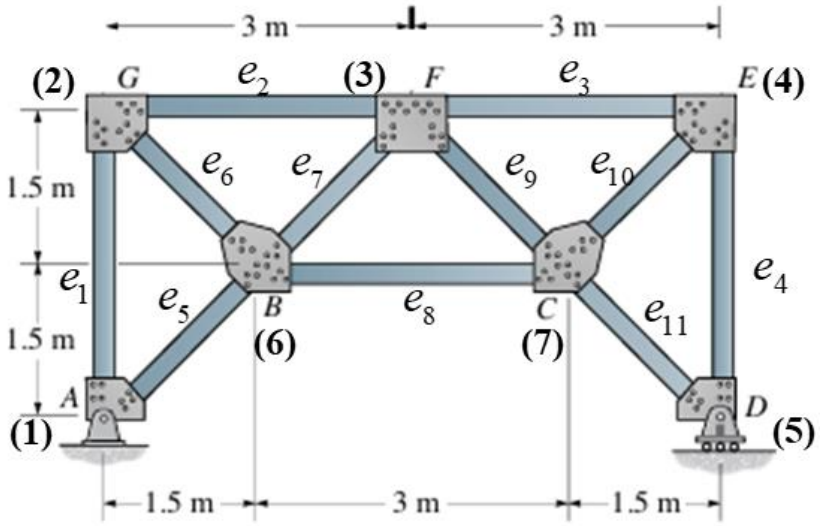

Fig. 5. Schematic of the second case study [50].

In two case study, the structural members are defined with a Young's modulus of E=200 GPa, material density of ρ=7800 kg/m³, and a uniform cross-sectional area of A=0.001 m². For this case study, various damage cases are considered, as summarized in Table 1.

Table 1. Various damage cases considered for the truss.

Case study	Damage scenario	Damaged structural element	damage intensity
First	Scenario 1	13	0.33
	Scenario 2	6, 11	0.2, 0.15
Second	Scenario 1	1	0.55
	Scenario 2	8	0.45
	Scenario 3	6, 11	0.25,0.15

7. Result

This section presents the observations and results related to truss damage identification under various damage scenarios in each truss case study. Generally, the truss structure in each case study is analyzed for 500 iterations with a population size of 300 for both single-element damage and multiple-element damage. The hybrid PSO–HHO algorithm combines the strengths of PSO and HHO to achieve a well-balanced trade-off between exploration and exploitation in complex search spaces. In the PSO component, key parameters such as inertia weight, cognitive coefficient, social coefficient, and velocity limits govern the dynamic behavior of particles. The inertia weight in this study starts at 0.9 and gradually decreases over the course of iterations. The cognitive and social learning coefficients typically range from 1.0 to 2.5, with standard values often set around 2.0. However, in this study, both the cognitive and social coefficients were set to 1.12, based on trials within the conventional range. Higher values led to decreased performance or failure to converge. On the other hand, the HHO component incorporates adaptive mechanisms for diversification through two key parameters: escaping energy and jump strength. The gradual decay of escaping energy across iterations facilitates the transition from global exploration in the early stages to local exploitation in the later stages. This adaptive behavior helps prevent premature convergence and encourages a more comprehensive exploration of the solution space. The escaping energy decreases linearly to enhance diversity and avoid entrapment in local optima. The jump strength, which determines the magnitude of random movement, is governed by randomly generated values. A summary of each parameter and its corresponding value is provided in Table 2. The following section presents the results related to the two case studies. In the first case study, in addition to the initial damage detection results, detailed statistical analyses and the individual performance of each algorithm are provided. Finally, in the second case study, the results of damage identification are presented and discussed.

Table 2. Parameters of the Hybrid PSO-HHO Algorithm.

Parameter	Description	Value or Range
w	Inertia weight controlling the influence of the previous velocity on the current one (*PSO*)	0.9
c_1	Cognitive acceleration coefficient; determines the impact of the particle's own best experience on its velocity (*PSO*)	1.12
c_2	Social acceleration coefficient; determines the influence of the global best position (rabbit) on the particle's movement (*PSO*)	1.12
Maximum velocity	Maximum velocity allowed for particles; used to limit how far a particle can move in a single iteration (*PSO*)	0.2*(upper bound-lower bound)
Minimum velocity	Minimum velocity allowed for particles; ensures that the movement doesn't become too small to be effective (*PSO)*	-upper bound

Escaping energy	Dynamic parameter in HHO controlling the transition between exploration and exploitation; decreases with each iteration (*HHO*)	$2*(1-\frac{it}{max\_it})$ * unifran (-1,1)
Jump strength	Controls the intensity of the Lévy flight-based jumps in HHO; adds randomness to enhance search diversification (*HHO*)	2*(1-rand ())

it: current iteration, *max_it:* maximum iteration
unifrand (-1,1): a random number from a uniform distribution in the range between -1 and 1.

7.1. First case study

The results of damage detection using the proposed hybrid PSO-HHO algorithm are presented in the next. Fig. 6 shows the convergence behavior of the hybrid algorithm across different runs for scenario 1. It is evident that from iteration 100 onwards, the algorithm achieves faster and more accurate convergence. The Table 3 summarizes three key performance indicators mean, initial rate of decrease, and stability for each of the four runs. The initial rate of decrease quantifies the early convergence behavior, measured by the drop in values between the first and second iterations. Stability is assessed by the standard deviation over the final 20% of the iterations, indicating the solution's consistency in the latter stages of the run; lower values correspond to higher stability.

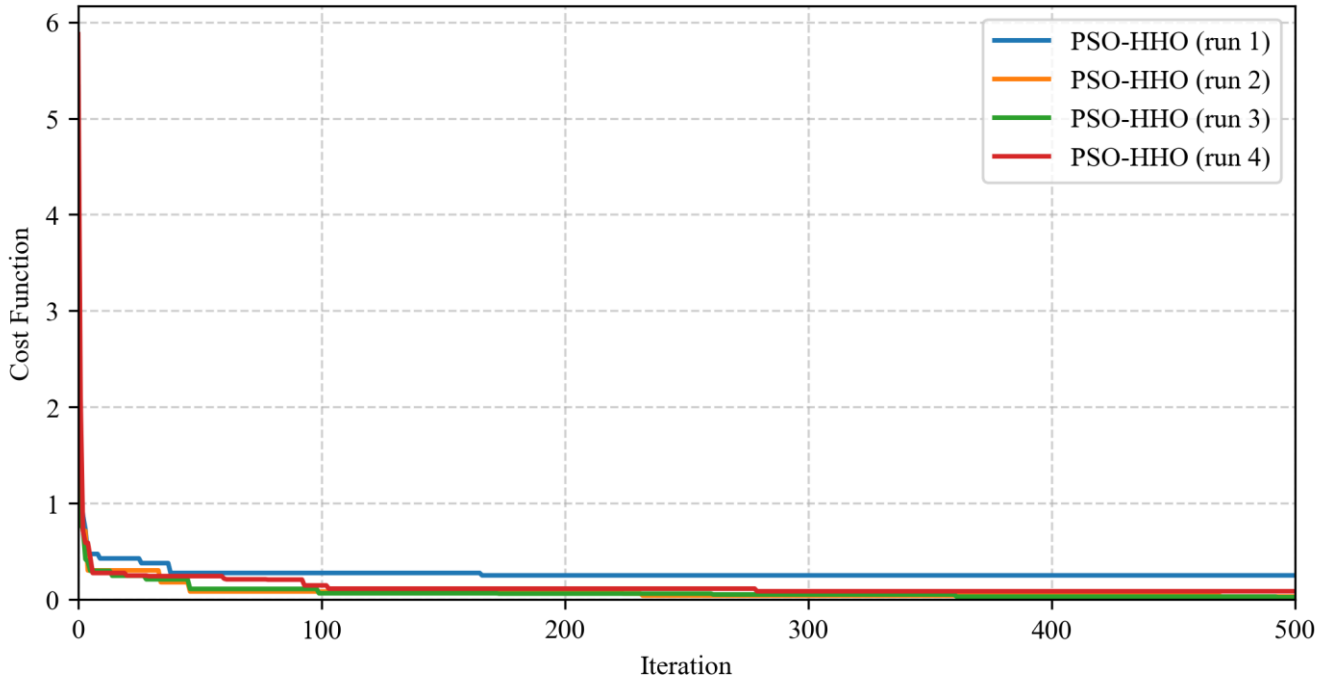

Fig. 6. The cost function of each hybrid PSO-HHO algorithm run for scenario 1.

Table 3. Comparison of performance metrics across four independent runs of the hybrid algorithm for scenario 1.

Run	1	2	3	4
Mean	0.282	0.089	0.083	0.14
Initial rate of decrease	4.25	3.36	2.91	3.78
stability	0.00	0.004	0.0015	0.00

Fig. 7 presents the predicted damage values for scenario 1 in each run of the hybrid algorithm, compared to the actual damage values.

For comparison and to assess the efficiency of the hybrid algorithm, the performance of the individual HHO and PSO algorithms is also described under identical population size and iteration settings. For each algorithm, four independent runs are performed, and the comparison is based on the average results obtained from these runs. Figs. 8 and 9 illustrate the comparison between the hybrid algorithm and the HHO and PSO algorithm, respectively. As shown, the hybrid algorithm significantly outperforms the HHO algorithm. While the performance of the HHO algorithm improves with increasing population size (from 600 to 1000) at a constant number of iterations, a substantial performance gap between the two algorithms remains. However, the population size appears to have had a negligible impact on the performance of the PSO algorithm in this case study, as similar trends were observed across different population settings.

Fig. 10 presents the distribution of the objective function values for the hybrid algorithm alongside the individual algorithms. Compared to Fig. 10a, Fig. 10b demonstrates a more consistent interquartile distribution across the algorithms, indicating a more stable performance of the HHO algorithm relative to PSO. The presence of numerous outliers in the PSO results also suggests a need for further tuning of the standalone PSO algorithm.

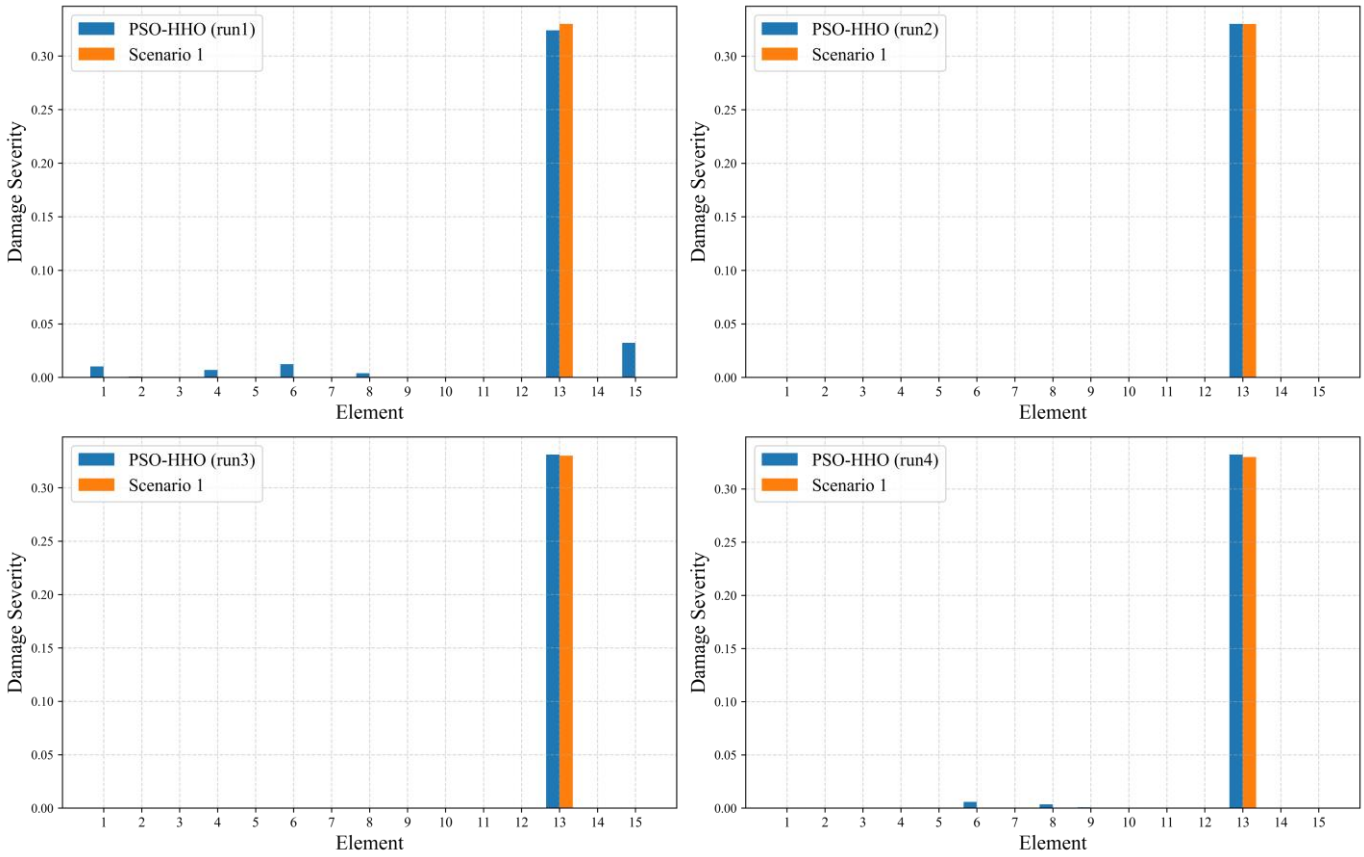

Fig. 7. The damage detection of each hybrid PSO-HHO algorithm run for scenario 1.

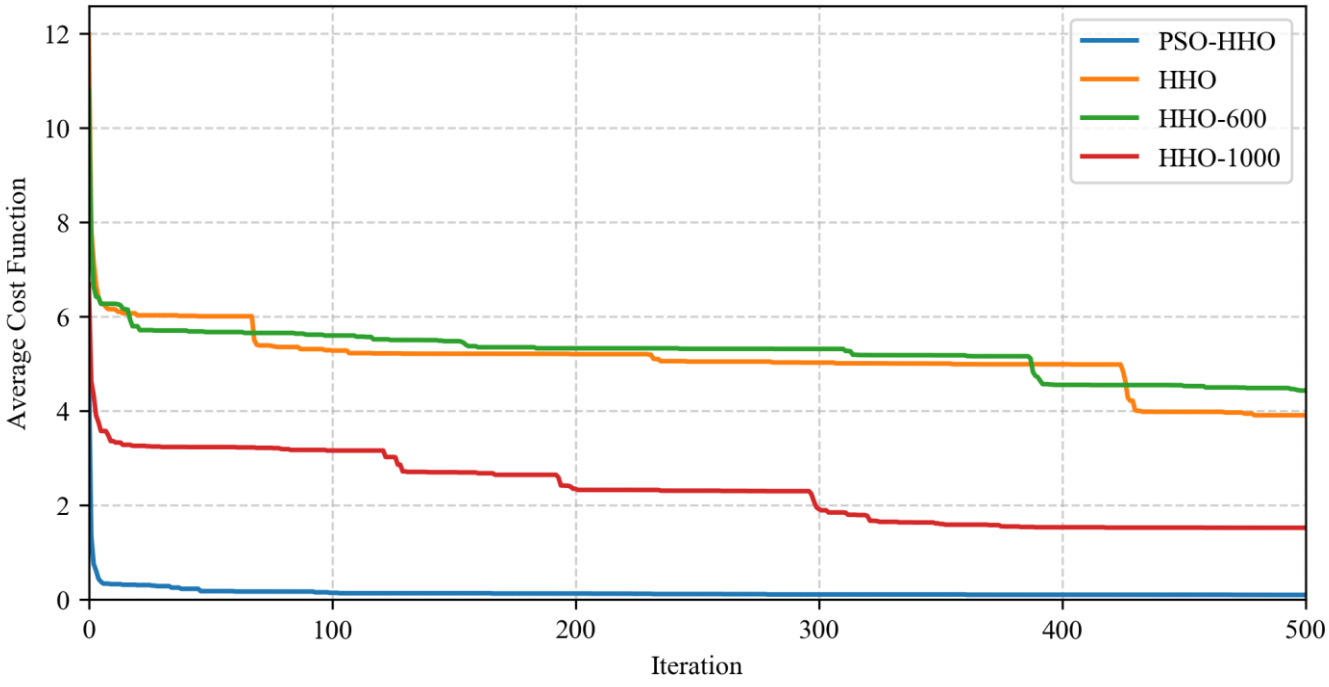

Fig. 8. The performance comparison of hybrid PSO-HHO and HHO for scenario 1.

In addition, statistical indicators provide valuable insight into the performance of each algorithm. Table 4 summarizes the statistical metrics computed for the objective function values obtained from the algorithms. It is worth noting that, for the hybrid algorithm, one of the four conducted analyses has been selected for representation. The PSO-600 algorithm shows the highest mean cost function, while PSO-HHO has the lowest, indicating much better optimization performance. PSO-HHO also exhibits the smallest standard deviation, indicating high consistency across runs. Among the standalone methods, PSO-1000 and HHO-1000 outperformed both their base versions and those with a population size of 600. Overall, the hybrid PSO-HHO approach clearly outperforms both individual PSO and HHO variants in both accuracy and stability.

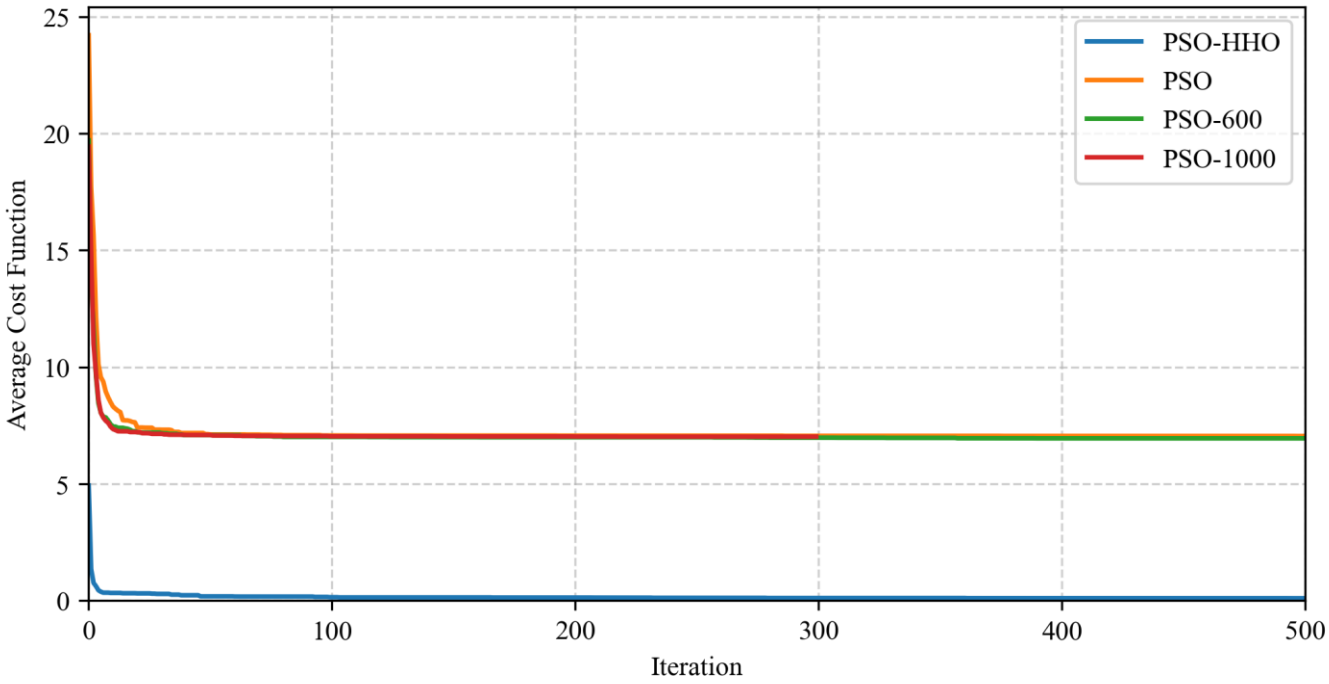

Fig. 9. The performance comparison of hybrid PSO-HHO and PSO for scenario 1.

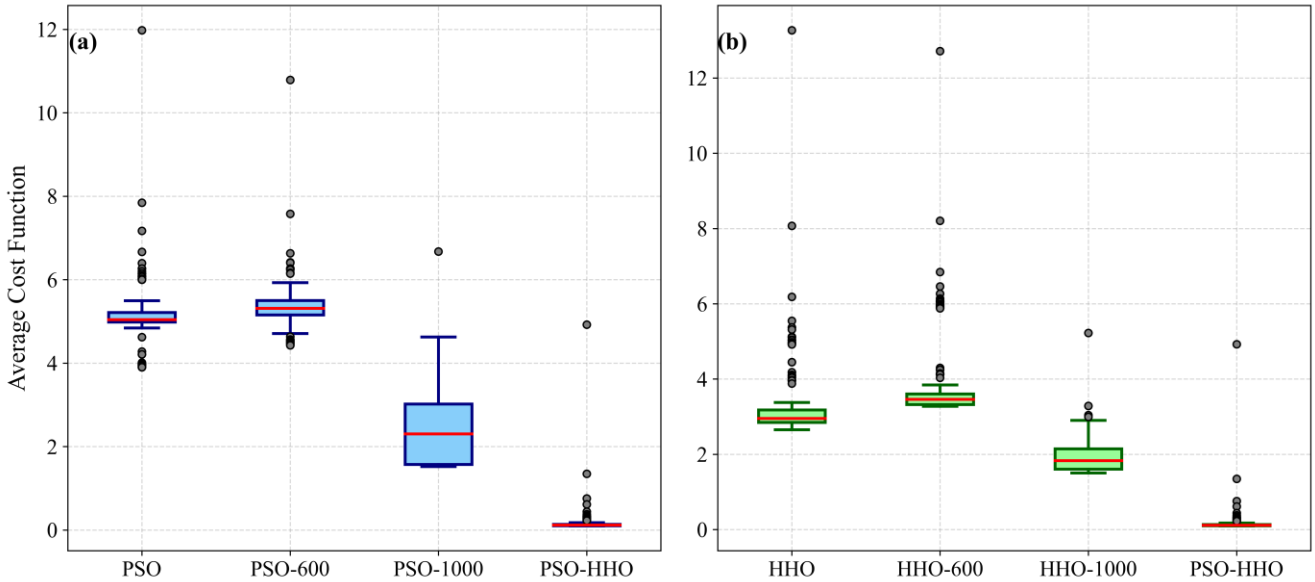

Fig. 10. Evaluation of cost function distributions for PSO, HHO, and hybrid algorithms in scenario 1. a) PSO comparison, b) HHO comparison.

Table 4. Statistical analysis of scenario 1 results for the hybrid algorithm and the individual PSO and HHO algorithms.

item	Mean	STD	Median	Min	Max
PSO	5.09	0.66	5.04	3.90	11.98
PSO-600	5.24	0.51	5.31	4.42	10.79
PSO-1000	2.31	0.70	2.30	1.52	6.68
HHO	3.20	0.78	2.95	2.65	13.27
HHO-600	3.82	0.96	3.46	3.27	12.72
HHO-1000	1.91	0.36	1.83	1.51	5.23
PSO-HHO	0.14	0.22	0.11	0.09	4.92

Fig. 11 shows the convergence behavior of the hybrid algorithm across different runs for scenario 2. Run 1 demonstrating the fastest initial descent and lowest final values, indicating superior performance. The Table 5 summarizes the key performance metrics for each of the four runs in scenario 2. The Run 2 demonstrates the greatest stability with a standard deviation of 0.002 in the last 20% of the data, whereas Run 1 shows the highest variability with a stability of 0.0135 in the same part.

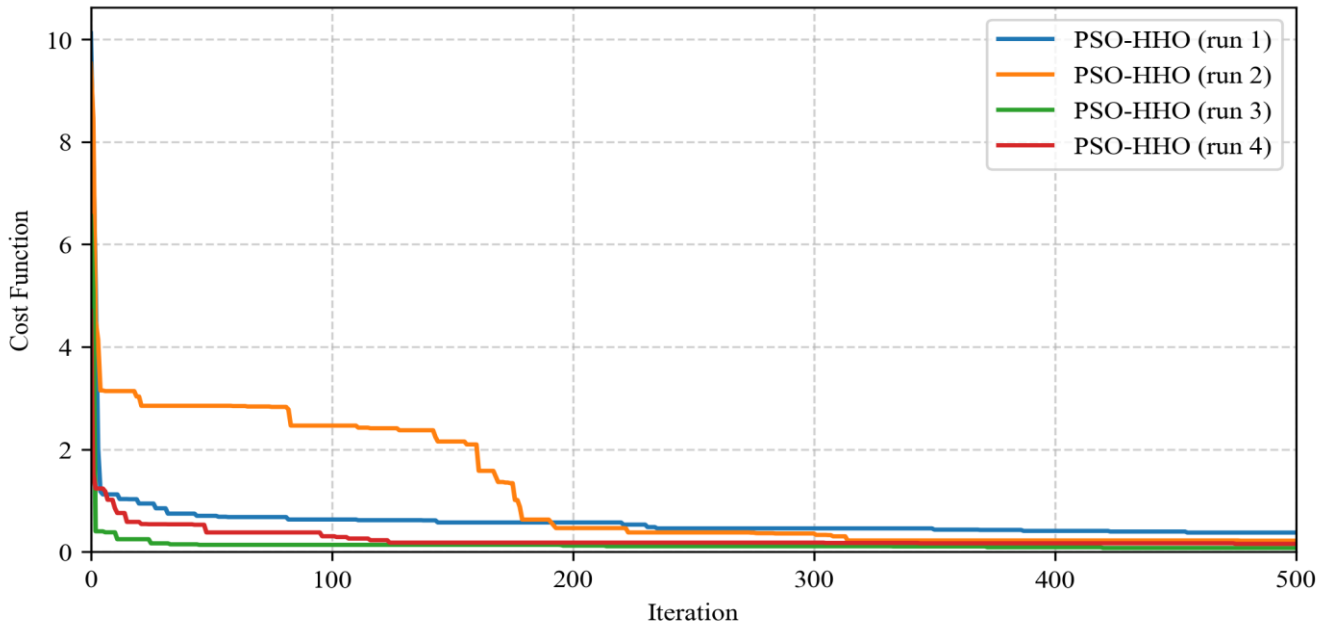

Fig. 11. The cost function of each hybrid PSO-HHO algorithm run for scenario 2.

Table 5. Comparison of performance metrics across four independent runs of the hybrid algorithm for scenario 2.

Run	1	2	3	4
Mean	0.58	1.1	0.14	0.25
Initial rate of decrease	2.37	1.063	1.47	3.17
stability	0.013	0.002	0.006	0.005

Fig. 12 presents the identified damage values for scenario 2 in each run of the hybrid algorithm, compared to the actual damage values. While the algorithm qualitatively demonstrates good performance in damage identification, quantitatively, the estimations occasionally overestimate or underestimate the actual damage values.

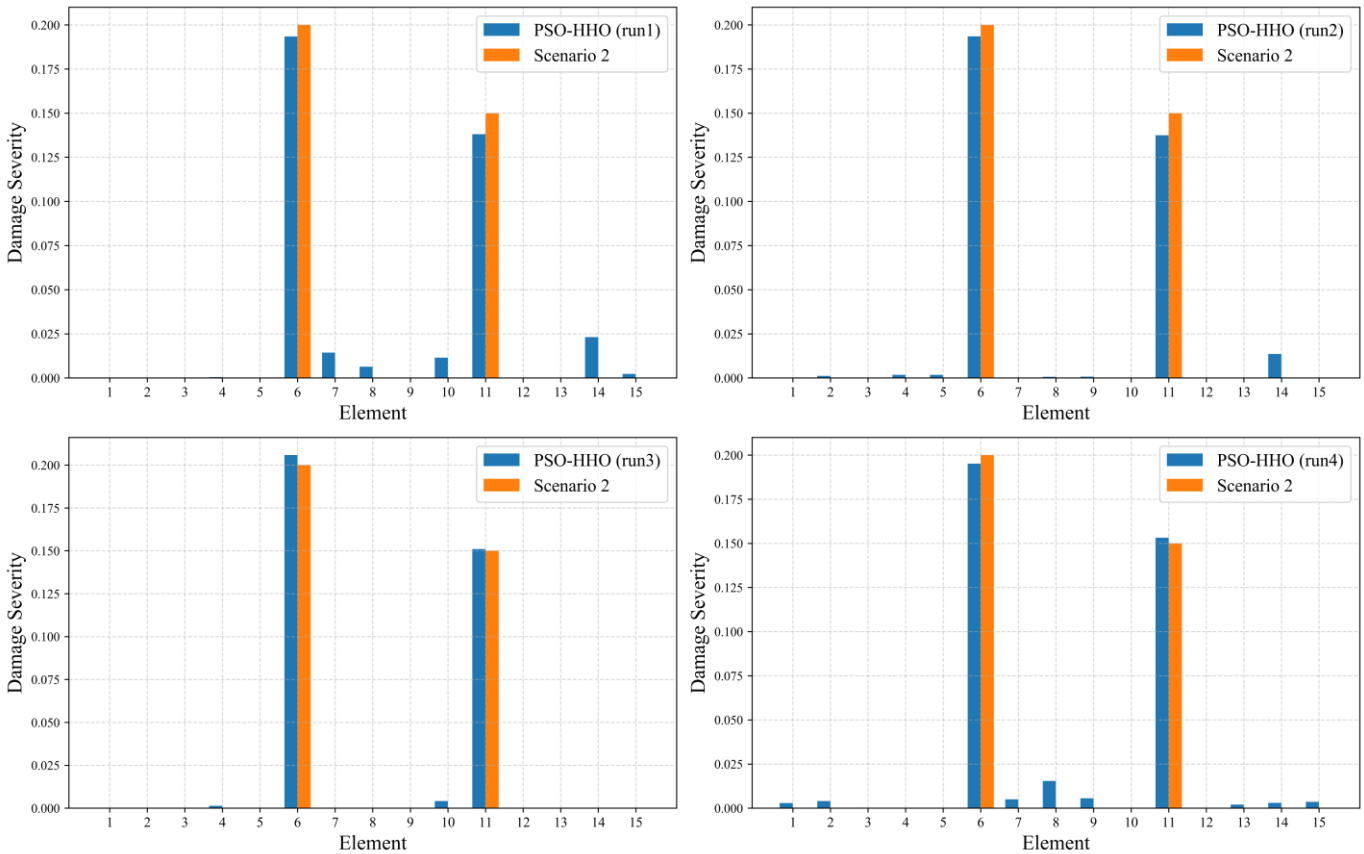

Fig. 12. The damage detection of each hybrid PSO-HHO algorithm run for scenario 2.

Figs.13 and 14 illustrate the comparison between the hybrid algorithm and the HHO and PSO algorithm, respectively. As

observed in scenario 1, the HHO algorithm once again demonstrates inferior performance when compared to the hybrid PSO-HHO algorithm under the same population size. Although HHO improves with larger populations, the hybrid algorithm consistently outperforms it across all settings. The cost function of the hybrid algorithm outperforms the HHO algorithm by approximately 30% to 65%, demonstrating a significantly improved performance. In contrast to scenario 1, increasing the population size has had a moderate impact on the performance of the PSO algorithm; nevertheless, a similar overall trend remains evident across different population sizes.

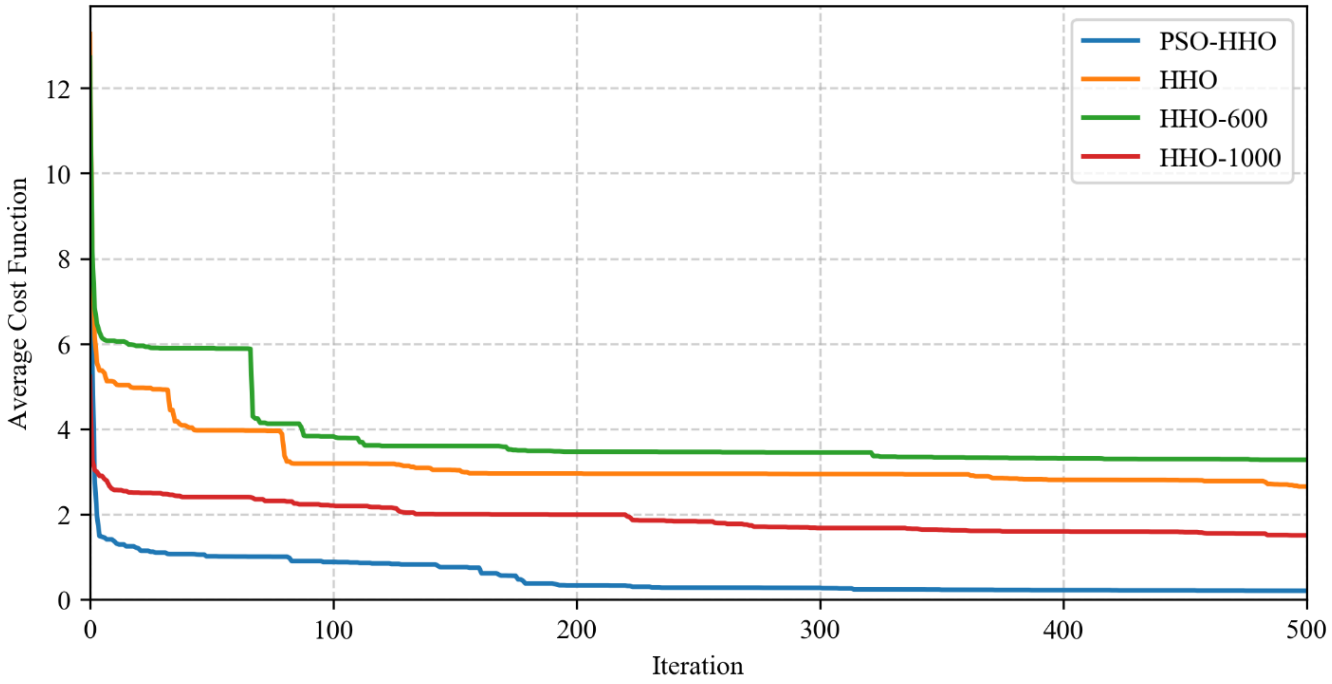

Fig. 13. The performance comparison of hybrid PSO-HHO and HHO for scenario 2.

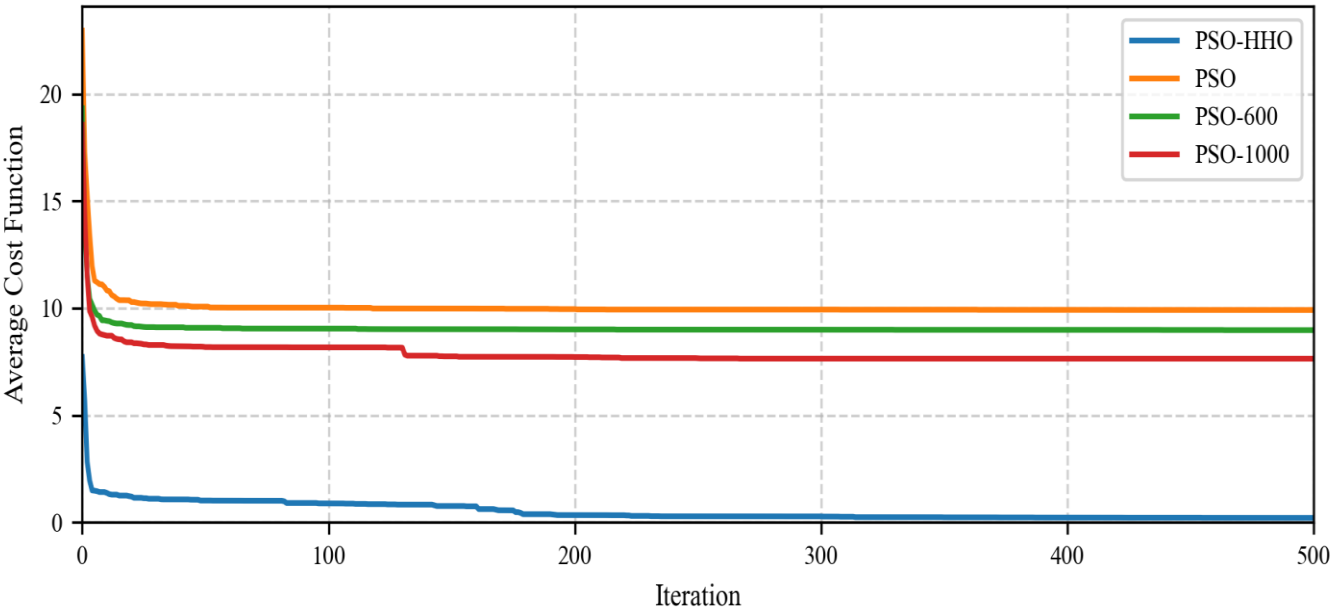

Fig. 14. The performance comparison of hybrid PSO-HHO and PSO for scenario 2.

The distribution and spread of the estimated objective function in this scenario for each algorithm are illustrated in the Fig. 15.

Table 6 presents the statistical parameters related to the objective function values obtained from each algorithm in scenario 2. A review and comparison of these parameters clearly indicate that the hybrid algorithm demonstrates relatively superior performance compared to the individual application of each algorithm in the given example.

7.2. Second case study

In this case study, three different damage scenarios are applied to the truss structure illustrated in Fig. 5. The following section presents the damage detection results obtained by the hybrid algorithm across four independent runs. It is worth noting that, due to the influence of various parameters affecting the performance of the hybrid algorithm, a larger number of analyses is required to reduce uncertainty and achieve stable and reliable results.

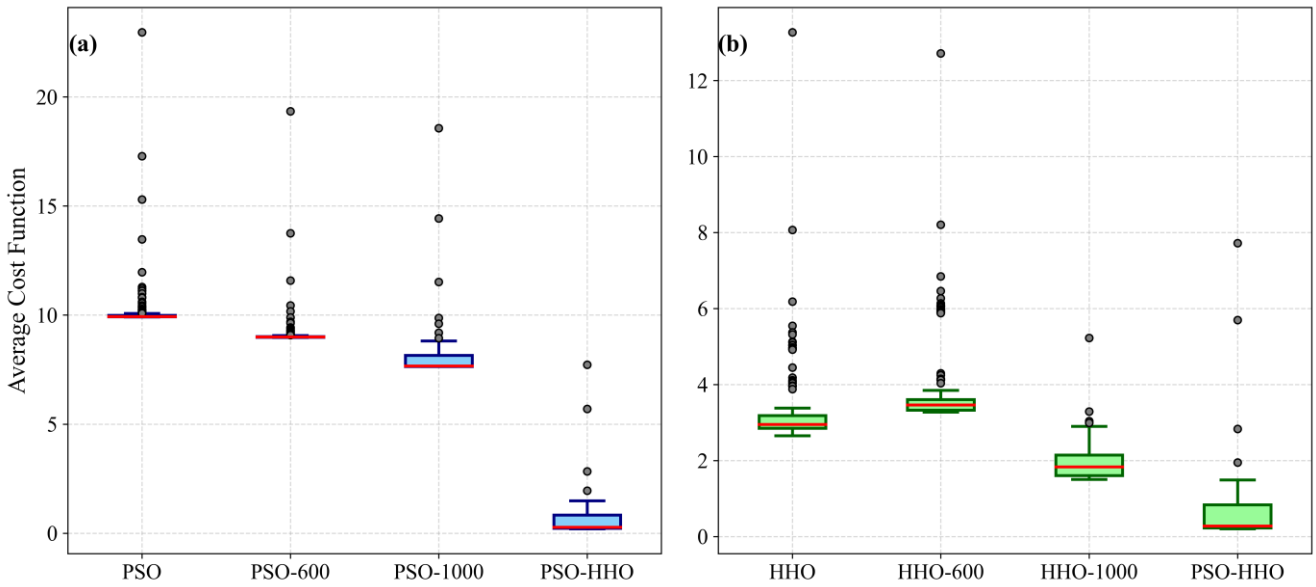

Fig. 15. Evaluation of cost function distributions for PSO, HHO, and hybrid algorithms in scenario 2. a) PSO comparison, b) HHO comparison.

Table 6. Statistical analysis of scenario 2 results for the hybrid algorithm and the individual PSO and HHO algorithms.

item	Mean	STD	Median	Min	Max
PSO	10.04	0.74	9.93	9.91	22.96
PSO-600	9.06	0.53	8.99	8.97	19.33
PSO-1000	7.86	0.65	7.66	7.63	18.56
HHO	3.2	0.78	2.95	2.65	13.26
HHO-600	3.82	0.96	3.46	3.27	12.71
HHO-1000	1.90	0.36	1.83	1.50	5.22
PSO-HHO	0.52	0.54	0.28	0.20	7.72

It is worth noting that, due to the influence of various parameters affecting the performance of the hybrid algorithm, a larger number of analyses is required to reduce uncertainty and achieve stable and reliable results. As illustrated in Fig. 16 the hybrid algorithm has successfully identified the damage located in a single member of the truss structure.

However, in the second scenario (see Fig. 17), although there is also damage in one member, due to its location near the center of the structure, the hybrid algorithm exhibited less stability in damage identification compared to the first scenario. While it successfully detected the damage in the affected member, it also incorrectly reported damage in other members.

Finally, in the third scenario, where two members are damaged, the hybrid algorithm performed qualitatively well by correctly identifying the damaged locations (see Fig. 18). However, from a quantitative perspective, it sometimes underestimates or overestimates the damage severity, which represents one of the algorithm's limitations at this stage. Additionally, the hybrid algorithm estimated minor damage in some other members, which, although small in magnitude, negatively affects the overall stability. The following section discusses some of the reasons behind these limitations.

8. Limitations of study

Although the proposed PSO-HHO algorithm demonstrates high accuracy in identifying damage scenarios under various conditions, it is important to acknowledge its potential limitations. One such limitation arises in cases involving multiple-damage locations that are close to each other or occur in structurally symmetric positions. In these situations, the algorithm may misinterpret the dynamic response, leading to overestimation or underestimation of the damage severity or even misidentification of the damage location. Furthermore, in cases where the modal information is incomplete, highly sensitive to noise, or affected by closely spaced modes, the performance of the hybrid optimization approach may degrade. This is particularly true when measurement errors or modeling inaccuracies are present, which can skew the objective function landscape and cause the algorithm to converge to suboptimal solutions. In addition, it has been observed that in complex scenarios especially those involving multiple damage scenarios the algorithm may require a larger number of iterations or independent runs to achieve consistent and accurate results. This is due to the increased complexity and multimodality of the search space in such cases, which can trap the algorithm in local optima if the search process is prematurely terminated. Therefore, increasing the population size, adjusting the convergence criteria, or applying ensemble or restart strategies may help to enhance performance in these challenging settings.

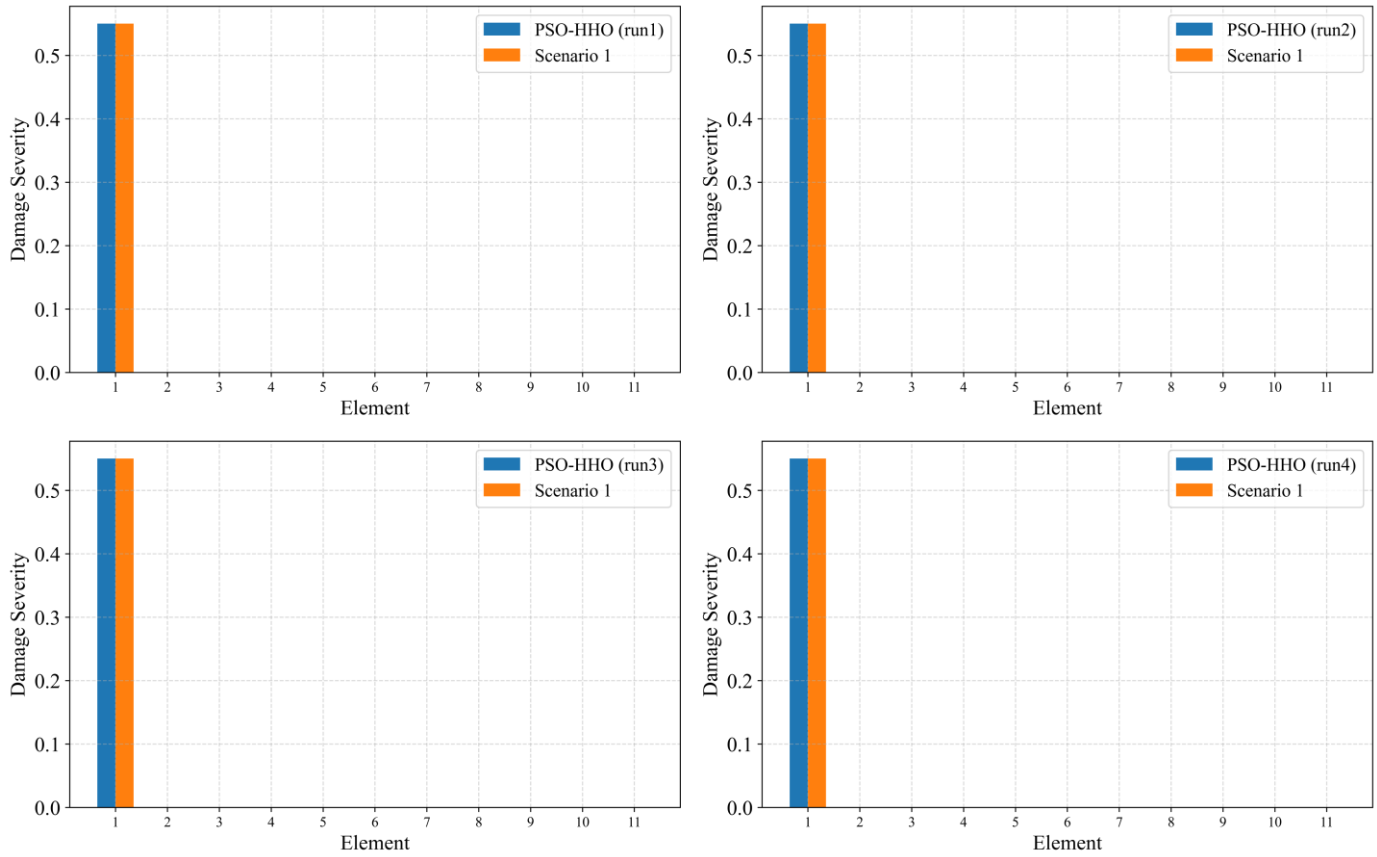

Fig. 16. The damage detection of each hybrid PSO-HHO algorithm run for scenario 1.

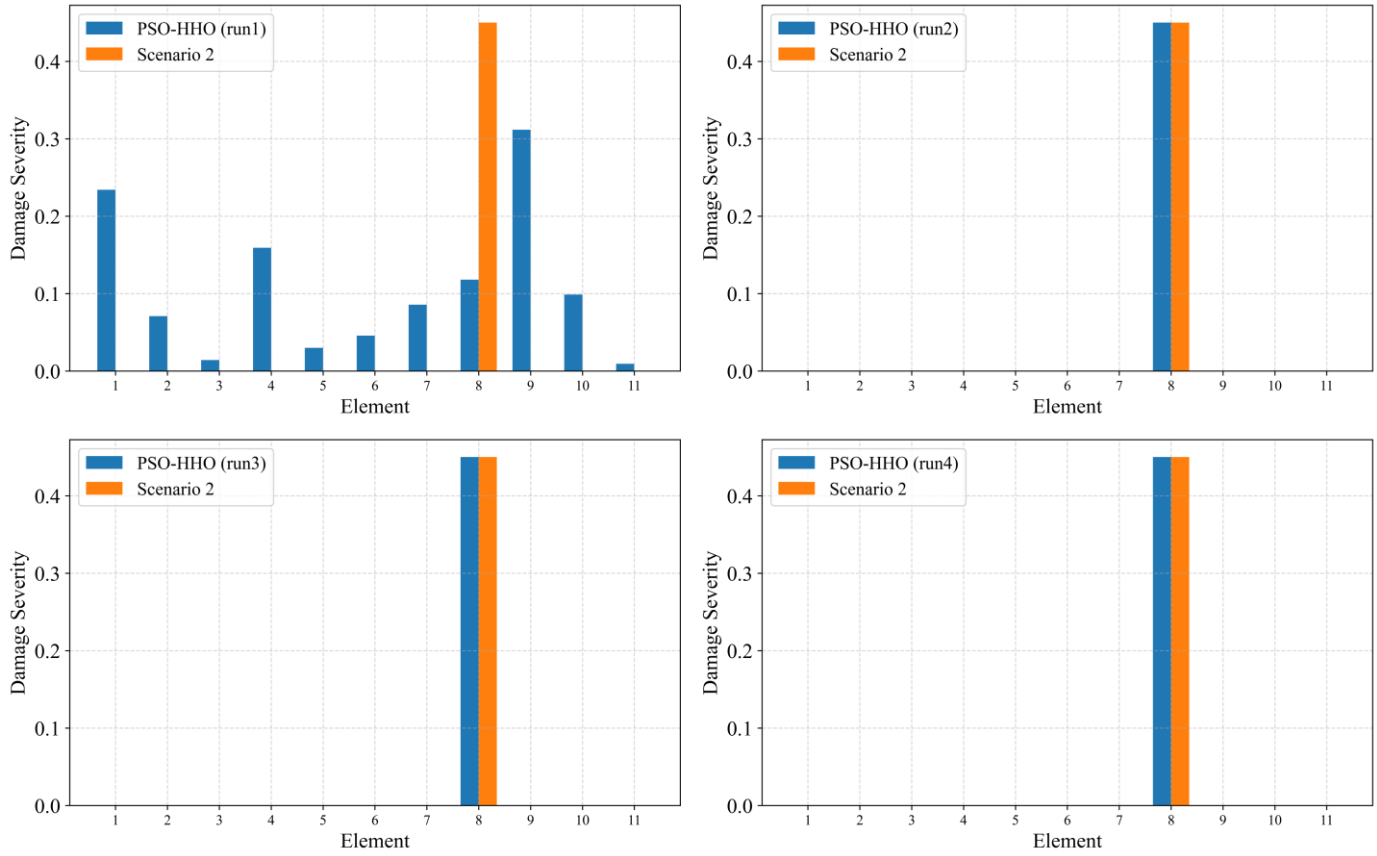

Fig. 17. The damage detection of each hybrid PSO-HHO algorithm run for scenario 2.

These challenges highlight the need for further studies to improve the robustness of the algorithm in complex scenarios. Possible future directions include incorporating noise-handling mechanisms, utilizing multi-objective optimization to simultaneously consider different damage indicators, and integrating prior knowledge or physical constraints into the search process to guide the algorithm away from false-positive or false-negative detections.

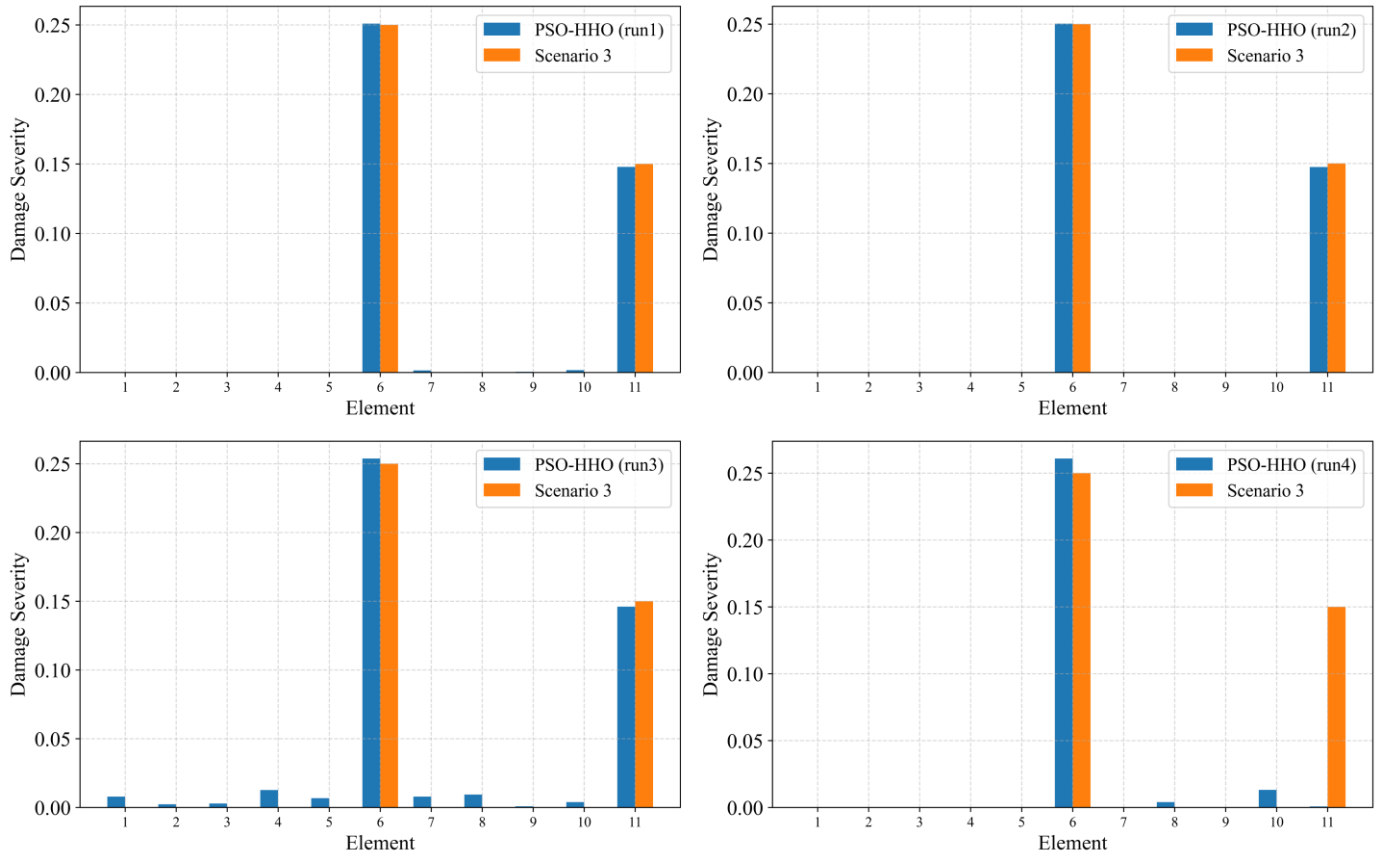

Fig. 18. The damage detection of each hybrid PSO-HHO algorithm run for scenario 3.

9. Conclusion

In this study, structural damage identification is performed by optimizing the objective function based on the modal parameters of the structure. To achieve this, a hybrid PSO-HHO algorithm is proposed and applied to detect damage under various scenarios. The results demonstrated the effectiveness of the hybrid approach in accurately identifying damage, outperforming individual algorithms and highlighting the value of integrating modal information for structural health monitoring. Based on the relevant findings of this research, the key observations can be categorized as follows:

1. The proposed hybrid PSO-HHO algorithm consistently outperforms the HHO and PSO algorithms in both damage scenarios. It achieves faster convergence, lower average cost function values, and greater stability in the final stages of optimization. This highlights the superior capability of the hybrid method, which identifies structural damage approximately 30% to 65% more accurately than the HHO algorithm.
2. The hybrid algorithm shows reliable performance in both single element and multiple element damage scenarios. Although deviations occur in the quantitative estimations, the method qualitatively identifies damage locations well. The algorithm demonstrates that in scenarios involving multiple simultaneous damages, careful tuning of its performance parameters is essential to ensure accurate results.

Statements & declarations

Author Contributions

Sayyed Hadi Alavi: Conceptualization, methodology, software, investigation, writing—original draft preparation, validation, writing—review and editing.

Amirhossein Pilehvaran: Conceptualization, methodology, software, investigation, validation, writing—review and editing.

Mohammadreza Mashayekhi: Conceptualization, methodology, software, investigation, writing—original draft preparation, validation, writing—review and editing, validation, supervision.

Acknowledgments

The authors thank their families for their constant support.

Funding

The author(s) received no financial support for the research, authorship, and publication of this article.

Declarations

The authors declare that they have no known competing financial interests or personal relationships that could have influenced the work reported in this paper.

Data availability

The data presented in this study are available on request from the corresponding author.

References

[1] Rincon, L. F., Moscoso, Y. M., Hamami, A. E. A., Matos, J. C., Bastidas-Arteaga, E. Degradation Models and Maintenance Strategies for Reinforced Concrete Structures in Coastal Environments under Climate Change: A Review. Buildings, 2024; 14 (3). doi:10.3390/buildings14030562.

[2] Feng, D., Feng, M. Q. Computer Vision for SHM of Civil Infrastructure: From Dynamic Response Measurement to Damage Detection – A Review. Engineering Structures, 2018; 156: 105–117. doi:10.1016/j.engstruct.2017.11.018.

[3] Asgari, A., Khabiri, A. Dynamic Analysis of Fatigue-Cracked Beams: The Nonlinear Response with the Analytical Method. Civil Engineering and Applied Solutions, 2025; 1(2): 43-54. doi: 10.22080/ceas.2025.29000.1002.

[4] Tibaduiza Burgos, D. A., Gomez Vargas, R. C., Pedraza, C., Agis, D., Pozo, F. Damage Identification in Structural Health Monitoring: A Brief Review from Its Implementation to the Use of Data-Driven Applications. Sensors (Switzerland), 2020; 20 (3). doi:10.3390/s20030733.

[5] Kong, K., Dyer, K., Payne, C., Hamerton, I., Weaver, P. M. Progress and Trends in Damage Detection Methods, Maintenance, and Data-Driven Monitoring of Wind Turbine Blades – A Review. Renewable Energy Focus , 2023; 44: 390–412. doi:10.1016/j.ref.2022.08.005.

[6] Doebling, S. W. S., Farrar, C. R. C., Prime, M. B. M., Shevitz, D. W. D. Damage Identification and Health Monitoring of Structural and Mechanical Systems from Changes in Their Vibration Characteristics: A Literature Review. Los Alamos National Laboratory, 1996; doi:10.2172/249299.

[7] Xiang, Z., Wang, L., Zhou, M. Suppressing Damage Identification Errors from Selected Natural Frequencies and Mode Shape Points. Inverse Problems in Science and Engineering, 2012; 20 (7): 871–890. doi:10.1080/17415977.2011.589902.

[8] Abe, M. Structural Damage Detection by Natural Frequencies. In 37th Structure, Structural Dynamics and Materials Conference. American Institute of Aeronautics and Astronautics: Reston, Virigina, 1996; pp 1064–1069. doi:10.2514/6.1996-1440.

[9] Kaveh, A., Zolghadr, A. An Improved CSS for Damage Detection of Truss Structures Using Changes in Natural Frequencies and Mode Shapes. Advances in Engineering Software, 2015; 80: 93–100. doi:10.1016/j.advengsoft.2014.09.010.

[10] Cawley, P., Adams, R. D. The Location of Defects in Structures from Measurements of Natural Frequencies. The Journal of Strain Analysis for Engineering Design, 1979; 14 (2): 49–57. doi:10.1243/03093247V142049.

[11] Adams, R. D., Cawley, P., Pye, C. J., Stone, B. J. Vibration Technique for Non-Destructively Assessing the Integrity of Structures. J Mech Eng Sci, 1978; 20 (2): 93–100. doi:10.1243/jmes_jour_1978_020_016_02.

[12] Ciambella, J., Pau, A., Vestroni, F. Modal Curvature-Based Damage Localization in Weakly Damaged Continuous Beams. Mechanical Systems and Signal Processing, 2019; 121: 171–182. doi:10.1016/j.ymssp.2018.11.012.

[13] Chu, S. Y., Wu, R. L. A Normalized-Relative-Displacement-Vibration-Shape (NRDVS)-Based Structural Damage Assessment Scheme. Journal of Structural Integrity and Maintenance, 2018; 3 (3): 150–159. doi:10.1080/24705314.2018.1492667.

[14] Liu, Y. Research on Bridge Damage Identification Method Based on Dynamic Characteristics. Journal of Engineering Research and Reports, 2023; 25 (8): 87–93. doi:10.9734/jerr/2023/v25i8961.

[15] Yoo, S.-H. Damage Detection of Shear Building Structures Using Dynamic Response. Journal of the Korea institute for structural maintenance and inspection, 2014; 18 (3): 101–107. doi:10.11112/jksmi.2014.18.3.101.

[16] Hsieh, K. H., Halling, M. W., Barr, P. J., Robinson, M. J. Structural Damage Detection Using Dynamic Properties Determined from Laboratory and Field Testing. Journal of Performance of Constructed Facilities, 2008; 22 (4): 238–244. doi:10.1061/(asce)0887-3828(2008)22:4(238).

[17] Sun, G., Liu, C., Zhang, S., Hao, E. Three-Step Damage Identification Method Based on Dynamic Characteristics. Transactions of Tianjin University, 2014; 20 (5): 379–384. doi:10.1007/s12209-014-2115-z.

[18] Feng, D., & Feng, M. Q. Computer vision for SHM of civil infrastructure: From dynamic response measurement to damage detection–A review. Engineering Structures, 2018; 156:105-117. Doi: 10.1016/j.engstruct.2017.11.018.

[19] Pothisiri, T., Hjelmstad, K. D. Structural Damage Detection and Assessment from Modal Response. Journal of Engineering Mechanics, 2003; 129 (2): 135–145. doi:10.1061/(asce)0733-9399(2003)129:2(135).

[20] Huynh, D., He, J., Tran, D. Damage Location Vector: A Non-Destructive Structural Damage Detection Technique. Computers and

Structures, 2005; 83 (28-30): 2353–2367. doi:10.1016/j.compstruc.2005.03.029.

[21] Escobar, J. A., Sosa, J. J., Gómez, R. Structural Damage Detection Using the Transformation Matrix. Computers and Structures, 2005; 83 (4–5): 357–368. doi:10.1016/j.compstruc.2004.08.013.

[22] Magacho, E. G., Jorge, A. B., Gomes, G. F. Inverse Problem Based Multiobjective Sunflower Optimization for Structural Health Monitoring of Three-Dimensional Trusses. Evolutionary Intelligence, 2023; 16 (1): 247–267. doi:10.1007/s12065-021-00652-4.

[23] Mashayekhi, M., Shirpour, A., Sadeghi, R. Finding Optimum Parameters of Passive Tuned Mass Damper by PSO, WOA, and Hybrid PSO-WOA (HPW) Algorithms. Journal of Soft Computing in Civil Engineering, 2023; 7 (4): 72–92. doi:10.22115/SCCE.2023.352340.1489.

[24] Ghaemifard, S., Ghannadiasl, A. Usages of Metaheuristic Algorithms in Investigating Civil Infrastructure Optimization Models; a Review. AI in Civil Engineering, 2024; 3 (1). doi:10.1007/s43503-024-00036-4.

[25] Sahoo, B., Maity, D. Damage Assessment of Structures Using Hybrid Neuro-Genetic Algorithm. Applied Soft Computing Journal, 2007; 7 (1): 89–104. doi:10.1016/j.asoc.2005.04.001.

[26] Aval, S. B. B., Mohebian, P. A Novel Optimization Algorithm Based on Modal Force Information for Structural Damage Identification. International Journal of Structural Stability and Dynamics, 2021; 21 (7). doi:10.1142/S0219455421501005.

[27] Abdolkhani, A., Raoufi, R. Structural Modal Identification and Damage Detection with Incomplete Data Utilized by Genetic Algorithm Optimization. Structures, 2023; 55: 16–27. doi:10.1016/j.istruc.2023.06.009.

[28] Gökdağ, H., Yildiz, A. R. Structural Damage Detection Using Modal Parameters and Particle Swarm Optimization. Materialpruefung/Materials Testing, 2012; 54 (6): 416–420. doi:10.3139/120.110346.

[29] Chandrupatla, T., Belegundu, A. Introduction to finite elements in engineering. London: Pearson; 2021. doi:10.1017/9781108882293.

[30] Kaveh, A., Dadras, A. Structural Damage Identification Using an Enhanced Thermal Exchange Optimization Algorithm. Engineering Optimization, 2018; 50 (3): 430–451. doi:10.1080/0305215X.2017.1318872.

[31] Zhu, J. J., Huang, M., Lu, Z. R. Bird Mating Optimizer for Structural Damage Detection Using a Hybrid Objective Function. Swarm and Evolutionary Computation, 2017; 35: 41–52. doi:10.1016/j.swevo.2017.02.006.

[32] Zamani, F., Alavi, S. H., Mashayekhi, M., Noroozinejad Farsangi, E., Sadeghi-Movahhed, A., Majdi, A. Optimum Design of Double Tuned Mass Dampers Using Multiple Metaheuristic Multi-Objective Optimization Algorithms under Seismic Excitation. Frontiers in Built Environment, 2025; 11. doi:10.3389/fbuil.2025.1559530.

[33] Minh, H. Le, Sang-To, T., Abdel Wahab, M., Cuong-Le, T. A New Metaheuristic Optimization Based on K-Means Clustering Algorithm and Its Application to Structural Damage Identification. Knowledge-Based Systems, 2022; 251 (109189). doi:10.1016/j.knosys.2022.109189.

[34] Tran-Ngoc, H., Khatir, S., Ho-Khac, H., De Roeck, G., Bui-Tien, T., Abdel Wahab, M. Efficient Artificial Neural Networks Based on a Hybrid Metaheuristic Optimization Algorithm for Damage Detection in Laminated Composite Structures. Composite Structures, 2021; 262 (113339). doi:10.1016/j.compstruct.2020.113339.

[35] Zacharakis, I., Giagopoulos, D. Vibration-Based Damage Detection Using Finite Element Modeling and the Metaheuristic Particle Swarm Optimization Algorithm. Sensors, 2022; 22 (14). doi:10.3390/s22145079.

[36] Kareem, S. W., Hama Ali, K. W., Askar, S., Xoshaba, F. S., Hawezi, R. Metaheuristic Algorithms in Optimization and Its Application: A Review. JAREE (Journal on Advanced Research in Electrical Engineering), 2022; 6 (1). doi:10.12962/jaree.v6i1.216.

[37] Abbasi, M. H., Moradi, H. Optimum Design of Tuned Mass Damper via PSO Algorithm for the Passive Control of Forced Oscillations in Power Transmission Lines. SN Applied Sciences, 2020; 2 (5). doi:10.1007/s42452-020-2677-4.

[38] Mashayekhi, M. R., Mosayyebi, S. A New Hybrid Harris Hawks Optimization (HHO) and Particle Swarm Optimization (PSO) Algorithm for the Design of Castellated Beams. Asian Journal of Civil Engineering, 2023; 24 (7): 2121–2139. doi:10.1007/s42107-023-00630-4.

[39] Coello Coello, C. A., Pulido, G. T., Lechuga, M. S. Handling Multiple Objectives with Particle Swarm Optimization. IEEE Transactions on Evolutionary Computation, 2004; 8 (3): 256–279. doi:10.1109/TEVC.2004.826067.

[40] Kennedy J, Eberhart R. Particle swarm optimization. In: Proceedings of ICNN'95 – International Conference on Neural Networks; 1995 Nov 27–Dec 1; Perth, Australia. Vol. 4. p. 1942–8.

[41] Mashayekhi, M., Harati, M., Estekanchi, H. E. Development of an Alternative PSO-Based Algorithm for Simulation of Endurance Time Excitation Functions. Engineering Reports, 2019; 1 (3). doi:10.1002/eng2.12048.

[42] lu, junhui, Zhang, L., Yue, Y. A Particle Swarm Optimization Algorithm with Dynamic Weights. In Second International Conference on Electronic Information Technology (EIT 2023), SPIE; Xiao, W., Leng, L., Eds.; 2023; p 142. doi:10.1117/12.2685758.

[43] Heidari, A. A., Mirjalili, S., Faris, H., Aljarah, I., Mafarja, M., Chen, H. Harris Hawks Optimization: Algorithm and Applications. Future Generation Computer Systems, 2019; 97: 849–872. doi:10.1016/j.future.2019.02.028.

[44] Alabool, H. M., Alarabiat, D., Abualigah, L., Heidari, A. A. Harris Hawks Optimization: a comprehensive review of recent variants and applications. Neural Computing and Applications. 2021; 33:8939–80. doi:10.1007/s00521-021-05720-5.

[45] Clerc, M., Kennedy, J. The Particle Swarm-Explosion, Stability, and Convergence in a Multidimensional Complex Space. IEEE Transactions on Evolutionary Computation, 2002; 6 (1): 58–73. doi:10.1109/4235.985692.

[46] Devarapalli, R., Kumar, V. Power System Oscillation Damping Controller Design: A Novel Approach of Integrated HHO-PSO Algorithm. Archives of Control Sciences, 2021; 31 (3): 553–591. doi:10.24425/acs.2021.138692.

[47] Ashfaq, R., Sajjad, I. A. Multiobjective optimal power flow (MO-OPF) using hybrid Harris Hawk–Particle Swarm Optimization algorithm (HHO–PSO). In: 2023 6th International Conference on Energy Conservation and Efficiency (ICECE); 2023 Mar 15–16; Lahore, Pakistan. p. 1–6. doi:10.1109/ICECE58062.2023.10092489.

[48] Murugesan, S., Suganyadevi, M. V. Performance Analysis of Simplified Seven-Level Inverter Using Hybrid HHO-PSO Algorithm for Renewable Energy Applications. Iranian Journal of Science and Technology - Transactions of Electrical Engineering, 2024; 48 (2): 781–801. doi:10.1007/s40998-023-00676-9.

[49] Laier, J. E., Villalba, J. D. Ensuring Reliable Damage Detection Based on the Computation of the Optimal Quantity of Required Modal Data. Computers and Structures, 2015; 147: 117–125. doi:10.1016/j.compstruc.2014.09.020.

[50] Hibbeler, R. C., Tan, K. H. Structural analysis. Harlow (UK): Pearson Prentice Hall; 2006.

Civil Engineering and Applied Solutions

Research Article

journal homepage: ceas.journals.umz.ac.ir

CEAS Civil Engineering and Applied Solutions

Multi-Parameter Assessment and Qualitative Zoning of Groundwater Resources to Identify Critical Quality Areas Using a GIS Approach

Milad Ghaderi Khorasgani [a], Hamed Reza Zarif Sanayei [a], Massoud Morsali [b*], Saeed Toghyani [a]

[a] *Department of Civil Engineering, University of Shahrkord, Shahrkord, Iran*
[b] *Department of Geology, Faculty of Science, University of Isfahan, Isfahan, Iran*

ARTICLE INFO

Keywords:
Groundwater quality index (GWQI)
Qualitative zoning
Groundwater resources
Chaharmahal and bakhtiari province
Principal component analysis (PCA)
Geographic information system (GIS)

Article history:
Received 08 July 2025
Accepted 13 July 2025
Available online 20 July 2025

ABSTRACT

This study conducts a multi-parameter assessment of groundwater quality in Chaharmahal and Bakhtiari province, Iran, to identify critical zones and support sustainable water resource management. Groundwater, vital for potable, irrigation, and industrial needs, was evaluated using the groundwater quality index (GWQI), Principal component analysis (PCA), and geographic information systems (GIS). Data from 2015–2016, collected from multiple sampling points, included parameters like pH, EC, TDS, TH, Na^+, Ca^{2+}, Mg^{2+}, Cl^-, SO_4^2, NO_3^-, and PO_4^{3-}. GWQI was calculated by weighting parameters against WHO standards, while GIS mapped seasonal and spatial quality variations. PCA identified key factors driving quality changes, with the first component (69.7–83.84% variance) linking salinity (EC, TDS, TH) and nutrient pollution (NO_3^-, PO_4^{3-}) to agricultural practices and evaporation, and the second (17.15–30.3% variance) reflecting K^+, SO_4^{2-}, Na^+, Mg^{2+}, and Cl^-, inversely related to TDS due to dilution. GWQI zonation showed good-to-excellent quality (0–50) in spring 2015, declining in autumn (50–75) due to evaporation and agricultural inputs, and improving in winter 2016 from rainfall infiltration. Eastern regions consistently exhibited poorer quality. The study highlights natural (evaporation, mineral dissolution) and anthropogenic (agriculture, contamination) influences on groundwater quality, with relative stability between 2015 and 2016 but notable seasonal variability. The integrated PCA, GWQI, and GIS approach, applied for the first time in this region, offers a robust framework for identifying critical zones and guiding localized management strategies. Biannual data and high-resolution mapping enhance methodological rigor, providing new insights into hydrogeochemical challenges and a dynamic tool for sustainable groundwater management.

1. Introduction

Groundwater provides approximately one-third of the world's freshwater supply and plays a pivotal role in sustaining domestic, industrial, and agricultural water demands, especially in arid and semi-arid regions where surface water resources are limited and unevenly distributed [1]. In countries such as Iran, which face both water scarcity and unequal spatial distribution of water resources, the management of groundwater quality is critically important. However, despite its strategic importance, rapid population growth, widespread industrialization, and intensive agricultural practices have led to the degradation and pollution of groundwater in many parts of the world. The consumption of contaminated groundwater poses serious threats to public health and can increase the prevalence of water-related diseases [2-4]. Accordingly, groundwater quality deterioration has become one of the principal global challenges to achieving sustainable development. In this context, multi-parameter evaluation and qualitative zoning through Geographic Information Systems (GIS) have emerged as effective tools for identifying critical quality zones and supporting

* Corresponding author.
E-mail addresses: m.morsali@sci.ui.ac.ir (M. Morsali).

https://doi.org/10.22080/ceas.2025.29622.1026
ISSN: 3092-7749/© 2025 The Author(s). Published by University of Mazandaran.
This article is an open access article distributed under the terms and conditions of the Creative Commons Attribution (CC-BY) license (https://creativecommons.org/licenses/by/4.0/deed.en)
How to cite this article: Ghaderi Khorasgani, M., Zarif Sanayei, H., Morsali, M., Toghyani, S. Multi-parameter assessment and qualitative zoning of groundwater resources to identify critical quality areas using a GIS approach. Civil Engineering and Applied Solutions. 2025; 1(2): 74–87. doi:10.22080/ceas.2025.29622.1026.

evidence-based water resource management. GIS facilitates spatial analysis and the visualization of complex hydrogeochemical datasets, enabling decision-makers to detect vulnerable areas with greater precision. The following section reviews relevant national and international studies related to this research focus.

2. Literature review

In Iran, due to the country's heavy reliance on groundwater resources, numerous studies have been conducted to assess groundwater quality and delineate spatial patterns using GIS. Li et al. [5], utilizing data from 27 wells in Abadeh County and applying the Schuler diagram alongside various interpolation techniques, demonstrated that kriging with exponential and circular variograms yielded the most accurate results for drinking water quality zoning. Similarly, Maghami et al. [6] evaluated groundwater quality in the Malayer Plain using the Water Quality Index (WQI) and GIS-based interpolation methods such as kriging and Inverse Distance Weighting (IDW). Their findings indicated that IDW was more suitable for interpolating parameters like electrical conductivity (EC) and total dissolved solids (TDS) in areas with uniformly distributed data, emphasizing the importance of selecting appropriate interpolation methods to enhance the accuracy of quality maps. Sadeghi et al. [7] analyzed groundwater chemistry data from the Amol–Babol Plain (1986–2009) using FAO standards and GIS-based zoning. Their results revealed that pollution was more critical near industrial zones and densely populated cities, with contamination levels increasing during low-discharge years. The use of sampled water quality data for delineating pollution zones has also been explored in several studies [8-16].

At the international level, recent advancements in remote sensing, machine learning, and GIS have significantly enhanced groundwater quality assessment and zoning. Tabrizi et al. [17], in a study conducted in southern India, employed WQI and GIS to evaluate groundwater quality in a semi-arid region. By analyzing physicochemical parameters such as TDS, nitrate, and heavy metals, they identified critical zones and demonstrated the effectiveness of GIS in visualizing and managing water quality data. In another study, Adimalla et al. [3] used GIS and geostatistical methods to map groundwater quality in Dhaka, Bangladesh. By analyzing 15 quality parameters and applying statistical techniques such as the Mann-Kendall trend test and Sen's Slope estimator, they assessed spatiotemporal variations and highlighted GIS as a powerful tool for detecting pollution trends. Karim et al. [18] investigated groundwater quality in the Achhnera region of Agra, India, by collecting and analyzing 50 samples. Their study employed WQI and Principal Component Analysis (PCA) to identify pollution sources. Results indicated that most samples were alkaline and unsuitable for drinking, underscoring the necessity of water treatment prior to consumption.

A comprehensive review of previous studies on groundwater quality degradation and pollutant sources reveals an escalating global challenge, particularly in arid and semi-arid regions such as Iran. While multiple factors contribute to this trend, anthropogenic activities, including overexploitation, agricultural runoff, urban wastewater discharge, and industrial effluents, play a central role in groundwater contamination. Given the rising demand for water across agricultural and industrial sectors, and in the absence of integrated quantitative and qualitative management strategies, the downward trend in groundwater quality is expected to accelerate. This issue is especially critical in Chaharmahal and Bakhtiari province, where declining precipitation, population growth, and the province's strategic role in supplying water to central and southwestern Iran amplify the urgency. Increased dependence on groundwater for agriculture, drinking, and industry, coupled with the widespread use of chemical fertilizers and rising volumes of municipal, industrial, and livestock wastewater, has intensified groundwater pollution in the region.

In summary, population growth, agricultural expansion, and increased wastewater generation are the primary drivers of groundwater contamination in Chaharmahal and Bakhtiari. Therefore, a precise and up-to-date assessment of groundwater quality in this province is essential. This study aims to identify critical and polluted zones by evaluating groundwater quality using a comprehensive set of physicochemical indicators. Its innovative approach integrates multiple indices with GIS-based zoning techniques to provide a holistic and accurate depiction of groundwater status. This integrated methodology enables the identification of spatial pollution patterns and prioritization of management actions, thereby contributing to the development of effective strategies for groundwater protection and restoration.

The following points highlight the innovative contributions of this study:

- Integrates multiple physicochemical indices with GIS-based zoning for a comprehensive groundwater quality assessment.
- Provides a novel spatial analysis of pollution patterns to identify critical and polluted zones accurately.
- Enhances groundwater management by prioritizing targeted protection and restoration strategies.

3. Methodology

3.1. Study area

Chaharmahal and Bakhtiari Province, covering an area of 16,533 km² in western Iran (Fig. 1), is situated within the Zagros Mountain range. The province's highest elevation is Zardkuh Peak at 4,536 m above sea level, while its lowest point lies at the confluence of the Bazoft and Armand rivers in the Margak region, at 800 m. Geologically, most of the province belongs to the Zagros structural zone, with its northern part extending into the Sanandaj–Sirjan metamorphic belt. This mountainous region, located between the internal foothills of the Zagros and Isfahan Province, is part of Iran's central plateau. Due to the region's young orogenic activity and the presence of active fault systems, it is prone to natural hazards such as floods, earthquakes, and landslides. Fig. 1 also presents the province's digital elevation model (DEM) and land use classification.

Thanks to its high-altitude terrain and exposure to moisture-laden Mediterranean air masses, the province receives relatively

high precipitation. Despite comprising only 1% of Iran's land area, it contributes approximately 10% of the country's total water resources. Snowfall and rainfall in the province's highlands feed two of Iran's most significant perennial rivers: the Karun and the Zayandeh-Rud, with respective catchment areas of 13,800 km² and 2,720 km². The Zayandeh-Rud is the only permanent river in Iran's central plateau, while the Karun is the country's largest river. However, both rivers face serious threats due to extensive dam construction and unsustainable inter-basin water transfers to provinces such as Yazd, Isfahan, and Kerman. With an average elevation of 2,153 m, the province features a rugged topography of hills and intermontane plains separated by mountain ridges. It includes 16 peaks exceeding 3,500 m in elevation (Fig. 1). These mountains extend from the northwest to the southeast of the province, gradually decreasing in height toward the east and into Isfahan Province. This transition leads to the formation of relatively broad plains such as Shahrekord, Farsan, Sefiddasht, Borujen–Faradonbeh, Kiar, Shalamzar, Gandoman–Boldaji, and Lordegan. Collectively, these plains account for approximately 24% of the province's area and are composed of alluvial deposits that provide favorable conditions for agriculture. However, the aquifers beneath these plains are limited in capacity and have been severely overexploited. As a result, all plains in the province are currently classified as either critical, restricted, or restricted zones for groundwater extraction. Of the ten major plains, four-Borujen-Faradonbeh, Javanmardi, Sefiddasht, and Shahr-e Kord are in a critical restricted state, while the remaining four Kiar, Lordegan, Gandoman–Boldaji, and Falard are designated as restricted.

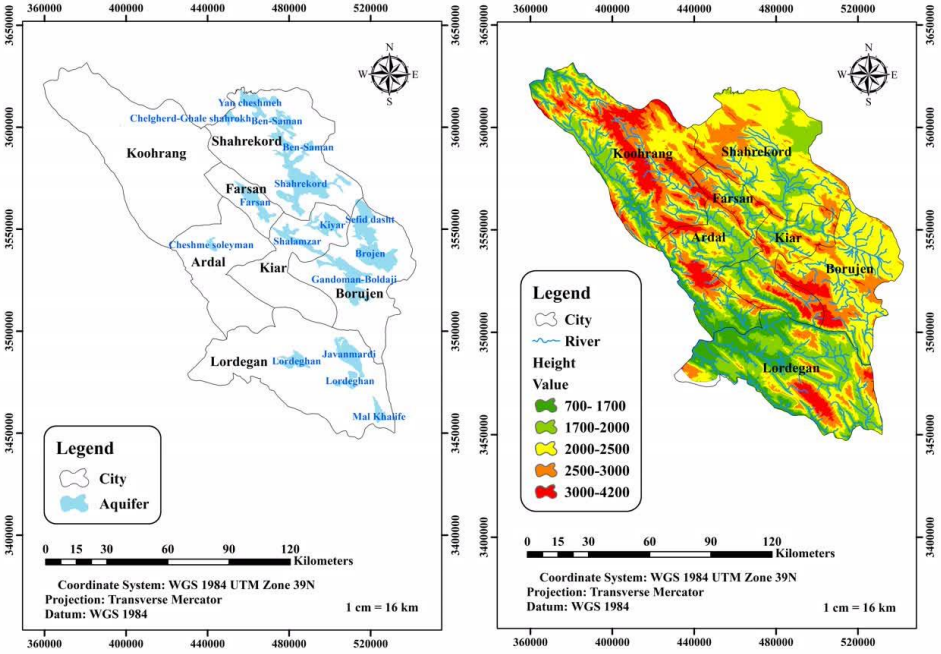

Fig. 1. Location of the study area with topographic variation.

3.2. Data collection and compilation

The sustainable development of water resources in any country is highly dependent on the availability of comprehensive databases encompassing both baseline data and accurate quantitative and qualitative analyses. These databases play a pivotal role in infrastructure planning, water use optimization, and the effective management of this vital resource. Only through rigorous analysis of the multiple components of the hydrological cycle, including hydrological, climatic, and environmental characteristics, can the actual capacity of water resources be assessed to meet the demands of sustainable economic and social development, thereby enabling the successful implementation of national infrastructure projects. Chaharmahal and Bakhtiari Province, owing to its unique hydroclimatological features, hosts a network of high-discharge rivers and valuable watershed systems. However, existing investigations reveal that the available data on the quantity and quality of water resources in this region suffer from significant limitations and deficiencies. A large portion of the data has been recorded over short time intervals, and the lack of continuous monitoring at measurement stations has compromised the accuracy and reliability of the information. To evaluate groundwater quality in the study area, the measurement and analysis of key water quality parameters were deemed essential. In this study, data about the physical and chemical characteristics of groundwater including EC, pH, total hardness (TH), TDS, sodium adsorption ratio (SAR), sulfate (SO_4^{2-}), chloride (Cl^-), sodium percentage (Na%), potassium (K^+), magnesium (Mg^{2+}), and calcium (Ca^{2+}) were examined for the years 2015 and 2016 (Table 1). These data were obtained in coordination with the Chaharmahal and Bakhtiari Regional Water Authority and collected using standard laboratory instruments such as portable EC and pH meters, as well as titration methods for hardness and ionic concentrations. Sampling and analytical protocols were conducted per the standards of the World Health Organization (WHO) and the Food and Agriculture Organization (FAO) to ensure data accuracy. Although the data used in this study were sourced from reputable institutions, limitations such as the absence of continuous monitoring at certain stations and the potential inclusion of reconstructed datasets may have affected the precision of the results. To mitigate these limitations, incomplete records were excluded, and only validated data were used in the analyses. Nevertheless, it should be noted that reconstructed datasets, even when developed using rigorous scientific methodologies, cannot fully match the quality of real-time

measurements, and thus, their reliability remains inherently constrained.

Table 1. Number of sampling points in the study area.

Year	Spring	Summer	Autumn	Winter	Total
1394	110	22	64	0	196
1395		37	77	62	180

3.3. Study approach

To assess the groundwater quality across the plains of Chaharmahal and Bakhtiari Province, a total of 196 samples in 2015 and 180 samples in 2016 were collected from various water sources, including operational wells, springs, and qanats. Sampling locations were purposefully selected to ensure adequate spatial coverage across the province's diverse plains. The geographic coordinates of each sampling point were recorded using a GPS device and mapped in ArcGIS 10.8 (Fig. 2). Sampling was conducted during both wet and dry seasons of the study years to capture potential seasonal variations in water quality. The collected data were statistically analyzed using SPSS version 24. Initially, the Kolmogorov–Smirnov test was applied to assess the normality of data distribution. Descriptive statistics, including mean, median, standard deviation, minimum, and maximum, were calculated for each parameter. To evaluate interannual differences between 2015 and 2016, a paired t-test was employed.

Additionally, Pearson correlation analysis was conducted to identify relationships between key water quality parameters, such as the correlation between EC and TDS. For spatial distribution mapping of groundwater quality parameters, ArcGIS 10.8 was used. The Kriging interpolation method was selected due to its high accuracy in modeling spatially heterogeneous data. This method was applied to generate zoning maps for key parameters such as EC, TDS, SAR, and pH, delineating areas with suitable and unsuitable water quality for drinking and agricultural purposes. To evaluate groundwater suitability for drinking, the results were compared with WHO standards, and for agricultural use, with FAO guidelines. The key water quality indicators assessed in this study include:

- EC: Indicates water salinity and its impact on agricultural use.
- SAR: Assesses irrigation suitability based on sodium's effect on soil permeability.
- TH: Reflects concentrations of calcium and magnesium, relevant to drinking and industrial use.
- TDS: A general indicator of water quality for both drinking and irrigation consumption.
- pH and Major Ions (SO_4^{2-}, Cl^-, Na^+, K^+, Mg^{2+}, Ca^{2+}): Used to evaluate chemical equilibrium and environmental implications.

These indicators were assessed per international standards and local hydrogeological conditions to support informed decision-making for optimal groundwater resource management.

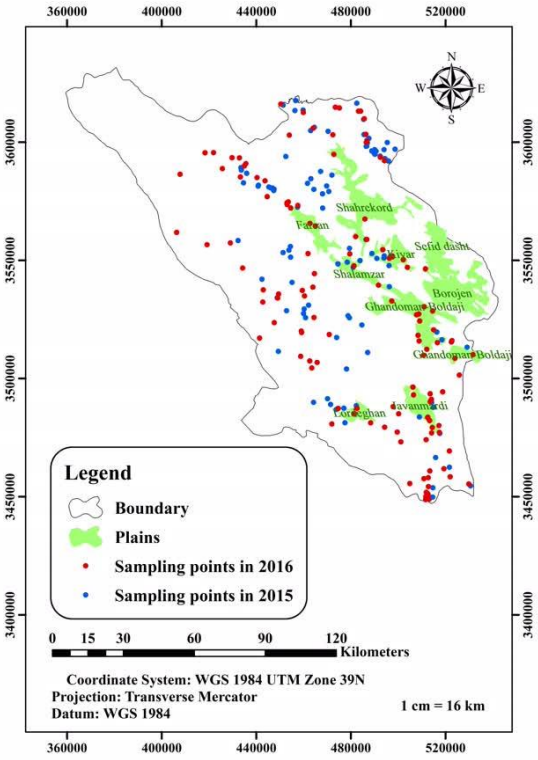

Fig. 2. Spatial distribution of sampling points in the study area during 2015 and 2016.

3.4. Groundwater quality index (GWQI)

The Groundwater Quality Index (GWQI) is one of the most widely used indices for qualitative zoning of water resources. Compared to other existing models, it presents fewer limitations and is frequently adopted by researchers due to its simplicity and the accessibility of required quality parameters. This index is calculated based on values of key indicators such as pH, TDS, Cl^-, Ca^{2+}, Mg^{2+}, SO_4^{2-}, HCO_3^-, and Na^+. GWQI is a reverse-scale index, meaning that as the level of contamination increases, the index value decreases. The method integrates the cumulative effect of multiple water quality parameters into a single numerical value that reflects the overall groundwater quality. The number and type of parameters used in the calculation are flexible and adaptable depending on the study objectives and data availability. Typically, WHO drinking water standards are employed as reference thresholds in GWQI computation, making the index a reliable indicator of potability. A critical aspect of GWQI calculation is the identification of parameters with the highest and lowest sensitivity to the index outcome. To address this, a sensitivity analysis is applied to determine the influence of each parameter on the final GWQI score [19].

$$GWQI = \sum SI_i = \sum (W_i \times q_i) = \sum ((\frac{w_i}{\sum_{i=1}^{n} w_i}) \times (\frac{C_i}{S_i} \times 100)) \quad (1)$$

where the variables are defined as follows:

- W_i: Weight of parameter i
- q_i: Quality rating of parameter i, calculated by normalizing the measured concentration
- C_i: Measured concentration of parameter i
- S_i: Standard or guideline value for parameter i, based on international benchmarks such as the WHO for drinking water or the FAO for agricultural use

Two main approaches are employed for the evaluation of the GWQI:

a) GIS-based method

In this approach, groundwater quality data such as EC, pH, TDS, TH, SAR, and concentrations of major ions are collected from sampling points. These data are processed using ArcGIS 10.8, and spatial distribution maps for each parameter are generated through geostatistical interpolation techniques, such as Kriging. The individual parameter maps are then integrated using assigned relative weights, reflecting the significance of each parameter for the intended use (drinking or irrigation). The final GWQI map is created based on this weighted overlay. GWQI values are normalized within a 0–100 range, where values near 0 indicate excellent water quality and those near 100 represent poor quality. In addition, sensitivity analysis is conducted to evaluate the impact of excluding individual parameter maps on the accuracy of the GWQI. This method enables the spatial identification of groundwater quality patterns and critical zones, making it highly effective for regional-scale water resource management.

b) Data-driven method

The data-driven approach relies on the analysis of point-based field data for assessing groundwater quality. It computes the GWQI as a unitless score ranging from 1 to 100 based on observed concentrations. Due to its relative simplicity and minimal dependency on advanced geospatial tools, this method is suitable for studies with limited computational resources or a focus on non-spatial analysis. In this approach, lower GWQI values correspond to better groundwater quality, while higher values indicate deterioration. The classification of groundwater based on GWQI is presented in Table 2.

Table 2. Classification of groundwater quality based on GWQI.

Water Quality Classification	Index Value
Excellent (Suitable for all uses)	0-25
Good (Suitable for drinking and irrigation with minor limitations)	25-50
Moderate (Use with caution for specific purposes)	50-75
Poor (Requires treatment for drinking or has agricultural limitations)	75-100
Very Poor	100-125
Unsuitable (Unusable without extensive treatment)	More than 125

3.5. Graphical methods for groundwater quality assessment

Most approaches employed in groundwater quality studies are graphical, where the results of water sample analyses are presented using diagrams such as Piper, Chadha, Stiff, Wilcox, and Schoeller plots. One limitation of graphical methods lies in the number of samples and variables they can effectively handle. Moreover, graphical techniques cannot distinguish between sample groups or test for similarity among them. In contrast, statistical methods do not suffer from these constraints and are increasingly applied in groundwater quality investigations. However, a drawback of statistical methods is that they do not directly convey the chemical composition of the samples, and their results are not as readily interpretable in the context of hydrochemical processes and trends. Therefore, combining graphical and statistical approaches can retain the strengths of each while minimizing their limitations. In this study, the Piper trilinear diagram was utilized to classify groundwater types and hydrochemical facies. The use of triangular diagrams for hydrochemical data representation was first introduced by Hill and later developed by Piper, whose diagram became widely adopted globally. In Piper diagrams, ions are plotted as percentages of milliequivalents per liter in two separate triangles

representing cations and anions. These values are then projected into a central diamond field for comparative analysis. The Piper diagram enables the simultaneous comparison of a large number of analyzed samples. The size of plotted circles on the diagram may also represent TDS content. Overall, the Piper diagram presents the chemical characteristics of water based on the relative concentrations of its constituents [20].

Following the collection and preprocessing of statistical data, groundwater quality zoning maps were developed using ArcGIS 10.8. The GIS is an advanced computational platform for acquiring, storing, analyzing, and visualizing spatial data. It offers a unique capability to integrate, organize, and interpret spatial relationships among various parameters. In GIS, all data possess geographic attributes and can be effectively visualized. One of its numerous applications lies in the field of public health [21], where the spatial linkage of environmental and health data facilitates informed decision-making [22]. Identifying geographic areas at risk is considered a fundamental step in implementing preventive and therapeutic measures to mitigate risk factors and their societal consequences. Based on previous research and the outcomes of related studies, the strengths and limitations of each method can be assessed to provide actionable insights for future investigations. Owing to the versatility and effectiveness of GIS in various domains, it is also employed in the qualitative zoning of groundwater resources.

3.6. Determination of spatial distribution patterns of indicators

Understanding and comparing environmental phenomena inherently require their quantification or measurement. In principle, point-based data derived from sampling sites are insufficient on their own, and it is essential to spatially extend and generalize such information. To spatially interpolate point data considering both the spatial and temporal variability of each parameter, models are needed that can simulate the behavior of the studied variable at unsampled locations. Among these, geostatistical methods, such as Kriging, Co-Kriging, Thin Plate Spline Smoothing (TPSS), and Weighted Moving Average (WMA), are of considerable importance due to their incorporation of spatial correlation and the underlying spatial structure of the data. In geostatistics, not only the value of a measured variable but also the spatial coordinates of the sampling point are taken into account. Thus, it becomes possible to jointly analyze the spatial location and the corresponding quantitative attribute of each observation.

Spatial visualization of raw environmental data using maps within a GIS facilitates more efficient and comprehensive communication of information compared to numerical indices alone. Moreover, due to the irregular nature of spatial variation, describing all changes solely through numerical indices is often unfeasible. Therefore, to describe and represent the spatial variability of a given parameter, it is necessary to estimate its values at unsampled points using the known data from sampled locations [23]. In this study, spatial autocorrelation analysis, interpolation of unsampled locations, and the generation of prediction maps and zoning layers were conducted using ArcGIS 10.8. The process of estimating the values of a continuous variable in areas where direct measurements are unavailable is referred to as interpolation. In essence, interpolation visualizes continuous spatial variation as a well-defined surface. It plays a fundamental role in the mapping, analysis, and interpretation of two-dimensional environmental data. Various interpolation techniques exist for estimating spatially and temporally variable parameters. These methods differ primarily in how they assign weights to known surrounding observations to estimate values at unknown locations. Based on prior studies and to extend point-based data into spatially continuous representations while ensuring computational efficiency and avoiding unnecessary complexity, the Kriging geostatistical method was selected for use in this study.

3.7. Factor analysis

One of the statistical methods used for analyzing data sets is Factor Analysis (FA). This method is similar to regression analysis; however, in FA, the observed variables are regressed on latent (unobservable) factors. The primary objective of factor analysis is to explain the covariance structure among variables through a limited number of random, unobserved quantities known as factors. In this approach, variables grouped within the same factor exhibit high intercorrelation, while those in separate groups show relatively low correlation. Several techniques exist for extracting factors within the framework of factor analysis, which are discussed further below. Among multivariate statistical techniques, Principal Component Analysis (PCA) is commonly used to identify the key parameters influencing groundwater quality, and in this study, it was applied to determine the most influential parameters in assessing groundwater quality in the plains of Chaharmahal and Bakhtiari Province.

Among the spatial analysis methods, PCA is frequently employed for dimensionality reduction of input datasets. PCA aims to extract a smaller number of components that can capture the majority of the variance present in a large dataset, a process known as data reduction. This approach is particularly useful when the researcher does not wish to involve all original variables in the analysis but still requires the information they contain. PCA is a general technique for factor extraction that seeks to identify linear combinations of the variables that explain the maximum possible variance. Once the first principal component is extracted, its associated variance is removed, and the next principal component that explains the largest remaining variance is identified. This iterative process continues until the optimal number of components is determined. This method is also known as the principal axes method, which results in the creation of orthogonal (uncorrelated) axes [24].

PCA is considered one of the most powerful multivariate statistical tools and is particularly effective when dealing with large volumes of data, as it reduces the number of input variables without significant information loss. Initially, the input data were standardized using the appropriate formula in SPSS software. In the next step, the suitability of the dataset for PCA was assessed using the Kaiser-Meyer-Olkin (KMO) measure and Bartlett's test of sphericity. To enhance the interpretability of the relationships between input variables and extracted components and to better distinguish their groupings, Varimax rotation was applied.

4. Results and discussions

4.1. Comparative analysis of groundwater quality parameters

To evaluate the groundwater quality status over a two-year period based on measured quality parameters, the statistical characteristics of the data were first presented for the summer season of 2015 and 2016 in Tables 3 and 4. The analysis of groundwater quality data during the summer of 2015 and 2016 across the Chaharmahal and Bakhtiari plains revealed that the average pH declined from 7.65 in 2015 to 7.22 in 2016, approaching a more neutral condition. This reduction in average pH in 2016 may be associated with increased inputs of organic or inorganic pollutants, such as wastewater infiltration or agricultural fertilizers. However, the pH levels in both years remained within the WHO recommended range for drinking water (6.5–8.5), indicating suitability for this purpose.

EC and TDS increased from 448.64 µS/cm and 299.05 mg/L in 2015 to 466.46 µS/cm and 310.35 mg/L in 2016, respectively, indicating rising salinity levels in some areas. The increase in EC in 2016 suggests a higher concentration of dissolved ions or possible intrusion of saline water (e.g., from agricultural runoff or industrial wastewater). The broader EC range observed in 2016 reflects localized zones with elevated salinity, which may impose constraints on agricultural use (FAO standard: EC < 700 µS/cm for salt-sensitive crops). The rise in TDS aligns with the EC trend, indicating an increase in overall dissolved solids. Despite this, TDS concentrations in both years remained below the WHO threshold for drinking water (< 1000 mg/L), though values nearing 663 mg/L in some areas could pose limitations for sensitive crops.

TH exhibited a significant increase from 176.98 to 274.97 mg/L, mainly due to a marked rise in magnesium concentration (from 4.43 to 19.59 mg/L), while calcium and sodium levels decreased. The substantial rise in hardness in 2016 is likely related to increased concentrations of calcium and magnesium ions. In some locations, TH values approached the upper limit of the "hard" classification range (200–500 mg/L), which may affect drinking water palatability and lead to sedimentation issues in industrial applications.

The decrease in mean sodium concentration in 2016 may indicate reduced saline water intrusion or changes in agricultural practices. However, the wider concentration range suggests the presence of localized high-sodium zones, which should be evaluated for their potential to cause soil sodicity in agricultural lands.

A decline in potassium levels and reduced variability in 2016 (standard deviation of 0.015) could imply lower agricultural fertilizer inputs. The sharp rise in magnesium alongside a reduction in calcium may reflect underlying geological variations or differences in the sampled water sources, which could affect total hardness and warrant further hydrochemical investigation. The increase in sulfate concentration in 2016 may stem from agricultural activities (e.g., use of sulfate-based fertilizers) or wastewater infiltration, though values remained within the WHO guideline for drinking water (< 250 mg/L). The observed decrease in chloride concentration in 2016 may be indicative of reduced salinity or diminished saline water intrusion, with values in both years remaining acceptable for potable use.

NO_3^- concentration showed a significant increase from an average of 1.61 to 15.16 mg/L, emerging as a potential concern for drinking water in some areas. The marked rise in nitrate levels in 2016 suggests possible contamination from nitrogenous fertilizers or sewage. Concentrations exceeding 39.1 mg/L in certain locations approach the WHO limit (50 mg/L), highlighting the need for stricter monitoring and management.

Table 3. Descriptive statistics of groundwater quality parameters in the summer season of 2015.

Parameters	Minimum	Maximum	Mean	SD	Variance
PH	7.51	7.88	7.66	0.1	0.01
EC(µs/cm)	228	556	448.64	120.3	14475.19
TDS(mg/l)	153	369	299.04	79.01	6242.9
TH	160.2	280.8	176.98	34	1158.1
K	0.1	1.3	0.51	0.292	0.086
Na	1	26	18.77	7.98	63.71
Mg	1	10.5	4.43	3.57	12.7
Ca	47.4	97.4	63.57	12.6	159.13
Sio_3	0.23	0.93	0.46	0.23	0.054
Br	0.2	0.4	0.33	0.055	0.003
PO_4	0.1	0.7	0.32	0.28	0.076
NO_2	1	8.2	6.21	0.24	5.03
NO_3	1.2	4.5	1.61	0.66	0.44
SO_4	1	50	14.23	14.11	199.32
Cl	21.8	49.7	34.67	6.78	46
F	0.03	0.1	0.059	0.016	0

Table 4. Statistical characteristics of groundwater quality parameters in summer 2016.

Parameters	Minimum	Maximum	Mean	SD	Variance
PH	6.5	7.5	7.22	0.62	0.069
EC(µs/cm)	193	1004	466.46	190.28	36208.42
TDS(mg/l)	128	663	310.35	126.42	15982.4
TH	180	524.8	274.96	83.2	6923
K	0.38	0.41	0.387	0.015	0
Na	1.69	41.39	12.3	8.53	72.75
Mg	12.6	27.56	19.59	7.53	56.67
Ca	6.73	38	21.87	12.88	165.9
NO_2	0	0.14	0.051	0.033	0.001
NO_3	0	39.1	15.16	10.81	116.84
SO_4	5.6	30	17.8	17.25	297.68
Cl	10	43	31	18.25	333

4.2. Hydrochemical analysis of groundwater using the Piper diagram

Based on the chemical composition of groundwater samples collected during autumn and winter of 2016, the hydrogeochemical facies and groundwater types were interpreted using the Piper diagram (Figs. 3 and 4). In autumn 2016, the dominant hydrochemical facies was Ca–HCO_3 (calcium–bicarbonate), indicating fresh groundwater typically associated with karstic origins or interaction with carbonate formations. The prevailing water type was calcium–bicarbonate, although some samples exhibited a tendency toward mixed facies such as Ca–Na–HCO_3–Cl, likely due to elevated sodium and chloride concentrations. The formation of this facies during autumn can be attributed to the following factors:

- The presence of carbonate formations (e.g., limestone and dolomite) in the region enhances calcium and bicarbonate concentrations through mineral dissolution.
- Relatively high concentrations of chloride and sodium in certain locations, potentially linked to agricultural return flows (e.g., chloride- or sodium-based fertilizers) or wastewater infiltration.
- Carbonate mineral dissolution and ion exchange processes within the aquifer system, contributing to the development of the Ca–HCO_3 facies.

In winter 2016, the dominant hydrochemical facies shifted to Mg–HCO_3 or Ca–Mg–HCO_3, reflecting increased magnesium concentrations alongside bicarbonate. In some areas with elevated nitrate and sodium, mixed facies such as Mg–Na–HCO_3–Cl were also observed. The prevailing water types were magnesium–bicarbonate or calcium–magnesium–bicarbonate, with certain samples trending toward Mg–HCO_3–SO_4 facies due to increased nitrate and sulfate levels. The formation of these facies in winter can be explained by:

- Elevated magnesium concentrations, likely resulting from the dissolution of dolomitic minerals ($CaMg(CO_3)_2$) within the aquifer.
- Increased nitrate levels, probably due to the infiltration of nitrogen-based fertilizers or agricultural/urban wastewater. Elevated sulfate may also be linked to the use of sulfate-containing fertilizers.
- Changes in groundwater flow patterns or reduced aquifer recharge, potentially leading to higher ion concentrations during the winter season.

4.3. Factors influencing groundwater quality variation based on PCA

To identify and interpret the key factors controlling groundwater quality variation, PCA was performed on the dataset of water quality parameters. This multivariate statistical method reduces the dimensionality of the dataset by extracting a set of uncorrelated components (principal components), each representing a group of interrelated parameters that together explain a significant portion of the total variance. The factor loadings for each parameter on each component indicate the strength and direction of its contribution to the formation of that component. Based on the average water quality data collected over the two-year study period, the factor loadings and the percentage of variance explained by each principal component were extracted for the years 2015 and 2016, as shown in Tables 5 and 6. The PCA results for the year 2015 are interpreted as follows:

Principal Component 1 (PC1) in Table 5 accounts for the largest share of variance (84.83%) and is dominated by strong negative loadings for pH, PO_4, NO_3, Cl, and F, and strong positive loadings for EC, TDS, TH, Na, Ca, SiO_3, Br, and Mg. Based on this component, the hydrogeochemical variations observed in the aquifer can be attributed to the following:

- **Salinity and Hardness Effects**: The strong positive loadings for EC, TDS, TH, Na, Ca, and Mg indicate the critical role of evaporative concentration, mineral dissolution (e.g., carbonates and sulfates), and the intrusion of saline water or mineralized surface water in governing groundwater hydrogeochemistry. These may be linked to agricultural activities, irrigation, or seawater intrusion in coastal areas.

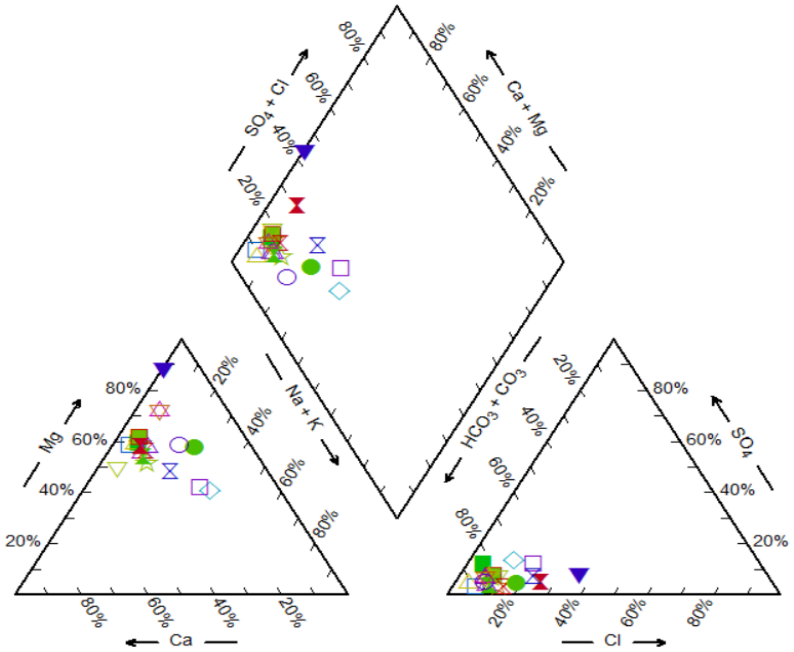

Fig. 3. Piper diagram of water samples in autumn 2016.

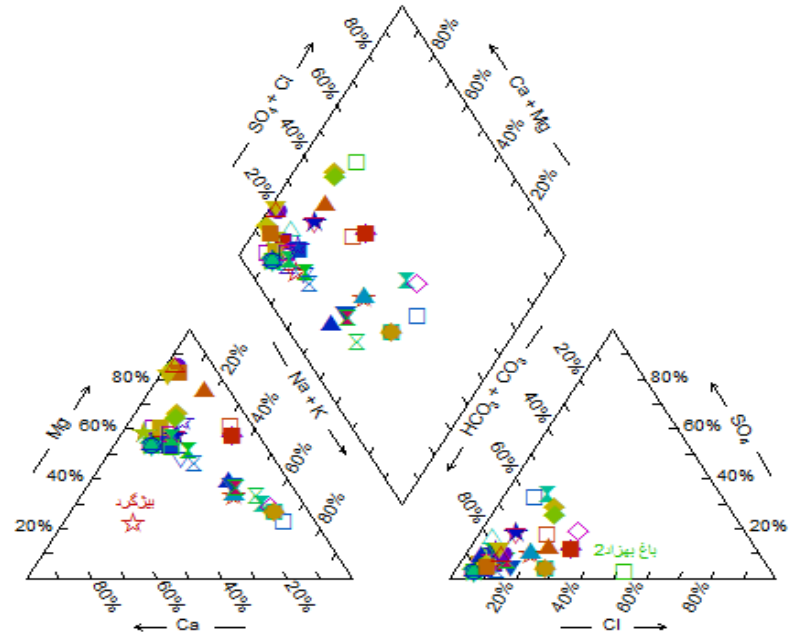

Fig. 4. Piper diagram of water samples in winter 2016.

- **Influence of Specific Ions and Pollution Sources**: The positive loadings for SiO_3 and Br may reflect natural geogenic sources such as silicate minerals or deeper groundwater inputs, while the strong negative loadings for Cl and F suggest potential anthropogenic contamination (e.g., wastewater discharge or agricultural fertilizers) or localized geochemical conditions.
- **pH and Nutrient Interactions**: The strong negative loading for pH suggests an inverse relationship between acidity and salinity/hardness parameters, which could be attributed to buffering effects from dissolved minerals or biological activities such as organic matter degradation.
- The negative loadings for PO_4 and NO_3 may indicate agricultural contamination sources (e.g., nitrogen and phosphorus-based fertilizers) that inversely correlate with salinity, possibly due to dilution effects or adsorption in soil matrices.

Overall, PC1 represents a dominant hydrogeochemical gradient characterized by increased salinity/hardness (positive loadings) versus reduced pH and nutrient levels (negative loadings). This pattern likely results from the interaction between mineral dissolution, evaporation, saline water intrusion, and anthropogenic pollution. For example, elevated EC and TDS may result from surface water infiltration or evaporation in arid zones, whereas reduced pH and elevated nutrient indicators may reflect domestic

wastewater or agricultural runoff. In essence, PC1 illustrates a prevailing hydrogeochemical process involving increased groundwater salinity and hardness due to mineral dissolution and saline intrusion, counteracted by nutrient pollution (phosphate and nitrate) and associated pH variations. To interpret this component more precisely, local variables such as soil type, climate, and land use must also be considered.

Principal Component 2 (PC2) explains a smaller share of the variance (15.17%) and is primarily characterized by high positive loadings for potassium (K: 0.960) and sulfate (SO_4: 0.976). The origin of groundwater quality variations represented by this component can be explained as follows:

- The strong loading for potassium indicates its significant influence within PC2, which could be linked to the weathering of potassium-bearing minerals (e.g., K-feldspar, mica) in the aquifer matrix or the leaching of potassium-rich water (e.g., from agricultural fertilizers). Elevated potassium levels may thus be associated with agricultural practices or selective weathering processes.
- The very high loading for sulfate highlights its importance in this component, which may originate from the dissolution of sulfate minerals (e.g., gypsum or anhydrite) or the oxidation of sulfide minerals (e.g., pyrite) in the subsurface. Elevated SO_4 concentrations may also reflect anthropogenic inputs such as industrial or agricultural runoff containing sulfate compounds.

Generally, this component appears to represent a secondary hydrogeochemical gradient governed by potassium and sulfate concentrations, in contrast to the dominant salinity and hardness parameters in PC1. PC2 may reflect localized processes such as selective mineral weathering, infiltration of sulfate-rich water, or point-source pollution. Moreover, the strong correlation between K and SO_4 may indicate a common source (e.g., potassium-sulfate fertilizers) or specific geochemical interactions within the groundwater system. Thus, PC2 represents a secondary hydrogeochemical process influenced by potassium and sulfate sources either geogenic (e.g., mineral weathering) or anthropogenic (e.g., fertilizer use or industrial discharge).

Table 5. Varimax-rotated principal component matrix of groundwater physicochemical parameters for the year 2015.

Component	PH	EC	TDS	TH	K	Na	Mg	Ca
1	-0.997	0.998	0.994	0.984	-0.28	0.918	0.989	0.997
2	0.08	0.06	-0.107	0.176	0.96	-0.396	0.15	0.079
Component	**Sio3**	**Br**	**PO4**	**NO2**	**NO3**	**SO4**	**Cl**	**F**
1	0.965	0.961	-0.96	-0.995	0.999	0.218	-0.951	0.958
2	-0.263	-0.277	-0.276	0.102	0.036	0.976	0.309	-0.285

In 2016, the status of the dominant components is as follows:

As shown in Table 6, PC1 accounts for 69.7% of the total variance. This component is characterized by strong negative loadings for EC, TDS, TH, Ca, and Cl, and strong positive loadings for pH, K, Na, PO_4, HCO_3, SO_4, Cl, and NO_3. The strong negative loadings suggest that carbonate and sulfate mineral dissolution (e.g., calcite) and saline water intrusion play a significant role in degrading groundwater quality. These processes may be associated with evaporation, surface water infiltration, or irrigation practices. Meanwhile, the strong positive loadings for pH, PO_4, and NO_3 indicate the influence of acid–base buffering conditions and nutrient-related pollution. The rise in pH may result from natural buffering mechanisms or biological activity, such as the decomposition of organic matter. The presence of PO_4 and NO_3 may reflect contamination from agricultural fertilizers or domestic wastewater. Positive loadings for Na, K, HCO_3, and SO_4 highlight diverse geochemical sources, including mineral dissolution (e.g., sodium carbonate or sulfate minerals) and the infiltration of bicarbonate-enriched water. The appearance of Cl with both negative and positive loadings in this component may suggest multiple pollution sources.

The similarity of the PC1 loading pattern to that of 2015 with comparable contributing parameters suggests relative consistency in the dominant hydrogeochemical processes. However, the change in loading direction for parameters such as Cl (from negative to positive) may indicate shifts in water sources, intensified anthropogenic activities (e.g., agriculture or industry), or climatic variations (e.g., rainfall or drought) during 2016.

In summary, PC1 in 2016 reflects the combined influence of salinity, hardness, and mineral dissolution, along with nutrient pollution (phosphate and nitrate) and pH fluctuations. This pattern likely stems from agricultural practices, saline water intrusion, and environmental interactions. A comparison with 2015 indicates the persistence of these processes, with minor changes in the source and dominance of specific ions.

PC2 explains 30.3% of the total variance in 2016 and shows strong positive loadings for Na, Mg, SO_4, and Cl, along with a strong negative loading for TDS. The high positive loadings for Na and Mg point to the influence of mineral dissolution processes, such as the weathering of halite, dolomite, or chlorite, or the infiltration of ion-rich waters. This may be related to the weathering of evaporite rocks or the percolation of surface water.

The strong positive loadings for SO_4 and Cl suggest dissolution of sulfate-bearing minerals (e.g., gypsum) or chloride-rich sources (e.g., halite), as well as possible contamination from saline water intrusion or anthropogenic sources, such as wastewater discharge or agricultural runoff. This pattern may reflect the influence of evaporation or human activity on groundwater chemistry. The strong negative loading for TDS suggests an inverse relationship between TDS and the positively loaded ions, possibly indicating selective enrichment of Na, Mg, SO_4, and Cl under conditions of localized dilution (e.g., rainfall events or infiltration of

lower-TDS water). Thus, PC2 appears to represent a secondary geochemical gradient, primarily associated with the selective dissolution of Na, Mg, SO_4, and Cl-bearing minerals and an opposing trend in total salinity. This may result from the interplay of weathering, localized evaporation, and the mixing of groundwater with chemically distinct waters. The negative loading of TDS could reflect dilution events during the 2016 period.

Table 6. Rotated component matrix for physicochemical parameters in 2016.

Component	PH	EC	TDS	TH	K	Na	Mg
1	0.999	-0.976	-0.975	-0.983	0.9	0.419	-0.352
2	-0.053	0.217	0.224	-0.184	0.436	0.908	0.936
Component	**Ca**	**PO4**	**NO2**	**NO3**	**HCO3**	**SO4**	**Cl**
1	-0.973	0.984	0.34	0.959	0.971	0.694	-0.47
2	0.233	-0.175	-0.941	-0.285	-0.239	0.72	0.883

4.4. Aquifer quality assessment based on GWQI

By applying weighted values to the collected groundwater quality variables, GWQI was calculated and seasonally zoned across Chaharmahal and Bakhtiari Province, enabling both spatial and temporal evaluation of groundwater quality. As outlined in Section 3.4, Part a, this study utilized point data collected from water resources within the aquifer to calculate the Groundwater Quality Index (GWQI) and map its distribution across the aquifer. The GWQI was computed using the parameters pH, EC, TDS, Cl^-, Ca^{2+}, Mg^{2+}, SO_4^{2-}, TH, NO_3, K, and Na^+, each assigned different weights based on their respective impacts and sensitivity to aquifer quality degradation. The weights assigned to the parameters, along with their respective standard values, have been incorporated into the manuscript as Table 7. The arrangement of weights and their relative importance were determined based on recommendations from previous studies, and no sensitivity analysis was conducted for individual parameters.

Table 7. Standard values (WHO (2017)) of quality parameters used in GWQI calculation and their assigned weights.

Parameter*	pH	EC	TDS	TH	K	Na	Mg	Ca	SO4	Cl	NO3
Standard Value	8.5	750	500	200	12	0.419	50	75	250	250	50
Assigned Weight	4	4	4	2	2	4	2	2	4	3	5

* The units of all parameters, except for pH (dimensionless) and EC (µs/cm), are in mg/L.

The analysis of GWQI variations in spring 2015 indicates that large portions of the study area, particularly in the central and eastern regions, fall within the "good to excellent" quality range. This favorable condition is likely attributed to spring rainfall infiltration. As illustrated in Fig. 5, groundwater quality during this season predominantly lies within the 0–50 range, reflecting a relatively favorable aquifer status. In contrast, the GWQI map for autumn 2015 reveals a relative decline in groundwater quality compared to spring, especially in areas where GWQI values range between 50 and 75. This seasonal degradation may be linked to increased evaporation, reduced precipitation, and intensified agricultural activities. The latter, particularly the use of fertilizers, could have contributed to elevated concentrations of nitrate (NO_3^-) and phosphate (PO_4^{3-}), a trend consistent with the positive loadings for these parameters observed in the earlier PCA results.

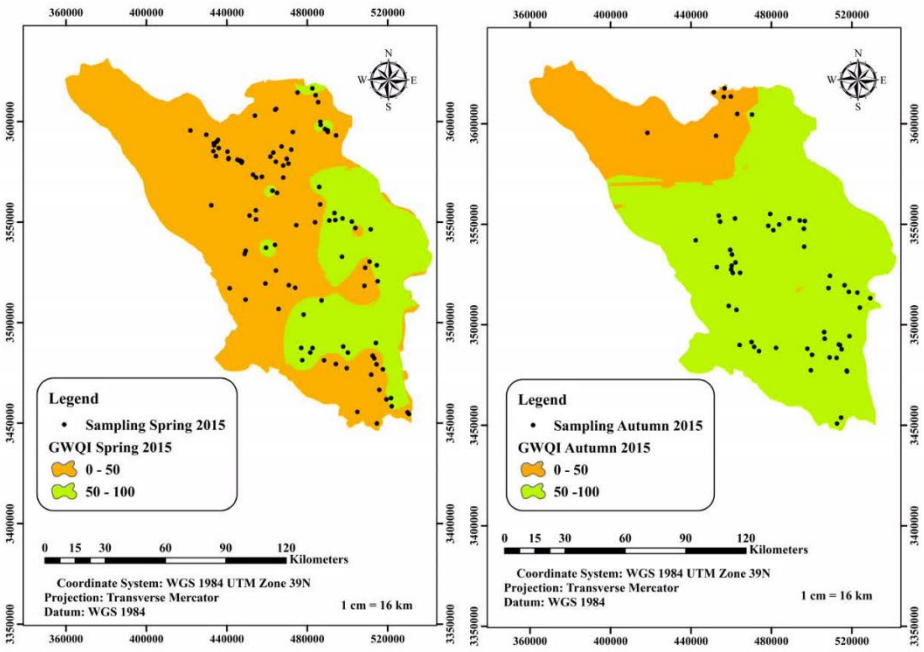

Fig. 5. Seasonal zoning map of GWQI in spring and autumn 2015.

The analysis of groundwater quality variations in 2016 reveals that during the winter season, due to limited rainfall infiltration and the presence of anthropogenic pollution in urban areas, low-quality patches emerged in the eastern parts of the aquifer (Fig. 6). Overall, however, a relative stabilization and improvement in groundwater quality compared to the previous year was observed, based on the GWQI.

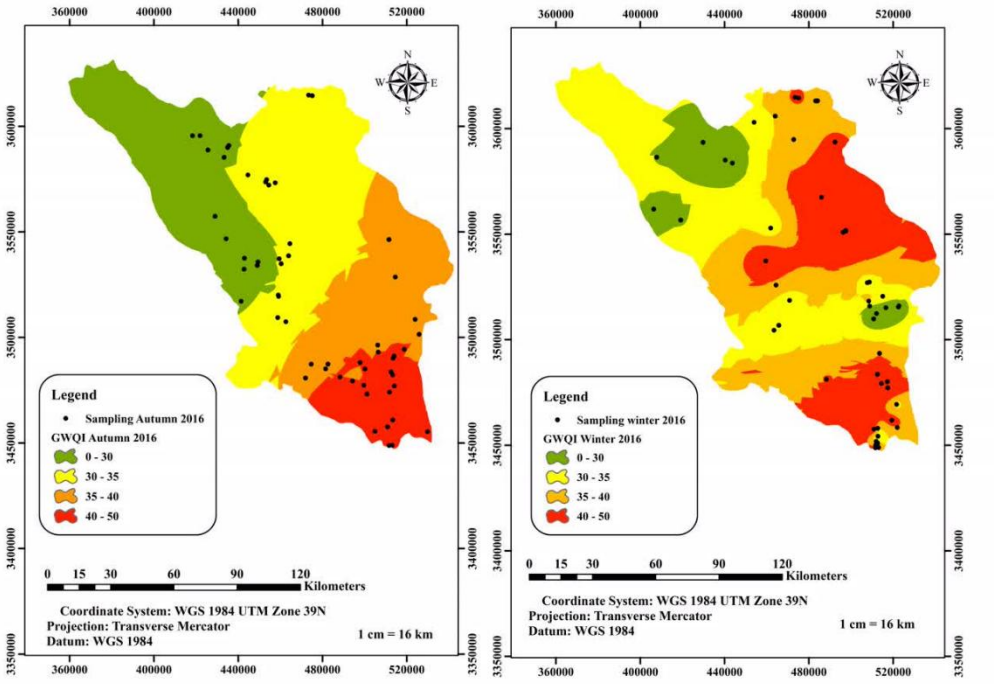

Fig. 6. Seasonal zoning map of GWQI in autumn and winter 2016.

5. Conclusions

Based on qualitative data collected over two years (2015–2016), the groundwater quality status across the aquifers of Chaharmahal and Bakhtiari Province was assessed, and the potential sources of quality variation were identified. The key findings are summarized as follows:

- The increase in TDS in 2016 correlates with elevated EC levels, indicating a rise in dissolved salts. Although the values remain within acceptable limits for drinking, they may pose challenges for salt-sensitive agricultural activities.
- A notable increase in water hardness, primarily attributed to elevated magnesium concentrations, may adversely affect domestic usage (taste) and industrial applications (scaling issues).
- The decline in mean sodium concentration suggests a potential reduction in saline water intrusion or changes in agricultural irrigation practices. However, the wider range of sodium values in 2016 highlights localized hotspots of high sodium concentration, raising concerns over sodicity hazards in agricultural soils.
- The observed reduction and homogenization of potassium levels in 2016 may indicate a decrease in agricultural fertilizer input.
- The increase in magnesium and concurrent decrease in calcium concentrations could be attributed to geological variations or differences in water source lithology at the sampling locations.
- The elevated sulfate levels may stem from agricultural activities, such as the application of sulfate-based fertilizers or wastewater infiltration. Nevertheless, the concentrations remain within safe limits for drinking water.
- The decline in chloride concentrations may reflect a reduction in salinity levels or a diminished influx of saline water, with values deemed suitable for drinking in both years.
- A significant increase in nitrate was identified in some locations, representing a potential health risk for drinking water and indicating the necessity for enhanced nitrate monitoring.
- Hydrogeochemical analysis of groundwater during the autumn and winter seasons of 2016 revealed seasonal variability in dominant hydrochemical facies: Ca-HCO_3 type in autumn and Mg-HCO_3 or Ca-Mg-HCO_3 types in winter. This shift may result from interactions between groundwater and carbonate/dolomitic formations, surface pollutant infiltration (especially in winter), and changes in groundwater flow dynamics, contributing to facies heterogeneity in the aquifer.
- PCA of groundwater quality data indicated that the first principal component (explaining up to 83.84% of variance in 2015 and 69.7% in 2016) is associated with salinity, hardness, and nutrient-related contamination (nitrate and phosphate), inversely influenced by pH and mineral dissolution, and predominantly linked to agricultural activities and evaporation.

The second component (17.15% in 2015 and 30.3% in 2016) reflects the presence of specific ions (K, SO_4, Na, Mg, Cl) and TDS dilution effects, pointing to mineral weathering and saline water intrusion. The persistence of these patterns across both years, despite minor shifts in ion sources, emphasizes the need for local-scale groundwater management and monitoring.

6. Recommendations for future research

- Enhanced nitrate monitoring: Given the significant increase in nitrate concentrations, reaching values near the WHO permissible limit, it is essential to conduct frequent and seasonally distributed monitoring across all sampling sites.
- Detailed hydrogeochemical analysis: To better understand the drivers of ion concentration changes, particularly for Mg, Ca, and Na, more comprehensive hydrogeochemical evaluations are required. These should include ion ratio analysis, saturation index calculations, and hydrochemical modeling.
- Pollution source identification: To determine the origins of nitrate and sulfate, detailed investigations into agricultural practices (types and application rates of fertilizers) and the presence of wastewater sources are crucial. This includes assessment of sewage systems, septic tanks, and agricultural drainage systems.
- Agricultural impact assessment: Given the increased TDS and localized high sodium levels, it is necessary to assess the implications for regional crop production. This could involve soil testing, monitoring of plant toxicity or deficiency symptoms, and consultation with agronomic experts.
- Soil sodicity risk evaluation: Due to the wide range of sodium values, it is recommended to compute the SAR in different areas and assess the sodicity hazard. If risk is confirmed, mitigation strategies such as soil amendments and improved drainage systems should be implemented.
- Human health risk assessment: Considering the increase in hardness and nitrate, evaluating the potential public health impacts is imperative. This could involve reviewing health records for waterborne diseases, conducting epidemiological studies, and issuing health advisories for the local population.
- Comparison with historical datasets: To gain a more comprehensive understanding of groundwater quality trends, it is essential to compare the two-year dataset with long-term historical records. This comparison can reveal temporal patterns and assist in identifying underlying causes of quality changes.

Statements & Declarations

Author contributions

Milad Ghaderi Khorasgani: Conceptualization, Methodology, Formal analysis, Resources, Writing - Original Draft.

Hamed Reza Zarif Sanayei: Resources, Writing - Original Draft.

Masoud Morsali: Conceptualization, Formal analysis, Resources, Writing - Original Draft.

Saeed Toghyani: Conceptualization, Writing - Original Draft.

Funding

The authors received no financial support for the research, authorship, and/or publication of this article.

Data availability

The data presented in this study will be available on interested request from the corresponding author.

Declarations

The authors declare no conflict of interes.

References

[1] Shaikh, H., Gaikwad, H., Kadam, A., Umrikar, B. Hydrogeochemical characterization of groundwater from semiarid region of western India for drinking and agricultural purposes with special reference to water quality index and potential health risks assessment. Applied Water Science, 2020; 10: 204. doi:10.1007/s13201-020-01287-z.

[2] Zhang, Y., Wu, J., Xu, B. Human health risk assessment of groundwater nitrogen pollution in Jinghui canal irrigation area of the loess region, northwest China. Environmental Earth Sciences, 2018; 77: 1-12. doi:10.1007/s12665-018-7456-9.

[3] Adimalla, N., Dhakate, R., Kasarla, A., Taloor, A. K. Appraisal of groundwater quality for drinking and irrigation purposes in Central Telangana, India. Groundwater for Sustainable Development, 2020; 10: 100334. doi:10.1016/j.gsd.2020.100334.

[4] Diédhiou, M., Ndoye, S., Celle, H., Faye, S., Wohnlich, S., Le Coustumer, P. Hydrogeochemical appraisal of groundwater quality and its suitability for drinking and irrigation purposes in the west central Senegal. Water, 2023; 15: 1772. doi:10.3390/w15091772.

[5] Li, P., He, X., Guo, W. Spatial groundwater quality and potential health risks due to nitrate ingestion through drinking water: a case study in Yan'an City on the Loess Plateau of northwest China. Human and ecological risk assessment: an international journal, 2019; 25: 11-31. doi:10.1080/10807039.2018.1553612.

[6] Maghami, Y., Ghazavi, R., Vali, A. A., Sharafi, S. Evaluation of spatial interpolation methods for water quality zoning using GIS Case study, Abadeh Township. Geography and Environmental Planning, 2011; 22: 171-182. doi:20.1001.1.20085362.1390.22.2.10.3.

[7] Sadeghi, S. H., Ghasemieh, H., Moemeni Damaneh, Javad, Mosavi, S. H. Irrigation and municipal water quality zoning by GIS. Irrigation and Water Engineering, 2016; 6: 128-137.

[8] Heidarzadeh, N., Moezzi, M. Groundwater quality analysis in Amol-Babol plain and zoning of sodium using GIS. Journal of Environmental Science and Technology, 2018; 4: 81-93. doi:10.22034/jest.2019.13703.

[9] Alimoradi, H., Rouhimoghaddam, E., Khaleghi, M., Bameri, A. Predicting and zoning of groundwater quality using geographical information system (GIS) models and machine learning methods (case study: Zahedan plain). Hydrogeology, 2023; 7: 43-60. doi:10.22034/hydro.2022.48571.1250.

[10] Jaafarzadeh, M. S., Moghaddamnia, A., Joodavi, A., Ahmadi, A. Assessment of the quality of Salmas aquifer and mapping of areas with pollution potential. Journal Of Iranian Water Engineering Research, 2023; 2: 35-56. doi:10.22034/ijwer.2024.482845.1056.

[11] Chitsazan, M., Tabari, M. M. R., Eilbeigi, M. Analysis of temporal and spatial variations in groundwater nitrate and development of its pollution plume: a case study in Karaj aquifer. Environmental Earth Sciences, 2017; 76: doi:10.1007/s12665-017-6677-7.

[12] Nemati, M., Tabari, M., Hosseini, S. A., Javadi, s. Identification of Factors Affecting Nitrate Contamination in Ardabil Plain Aquifer Using Statistical Methods. Water and Irrigation Management, 2023; 13: 527-550. doi:10.22059/jwim.2022.343545.995.

[13] Nemati, M., Tabari, M. M. R., Hosseini, S. A., Javadi, S. A Novel Approach Using Hybrid Fuzzy Vertex Method-MATLAB Framework Based on GMS Model for Quantifying Predictive Uncertainty Associated with Groundwater Flow and Transport Models. Water Resources Management, 2021; 35: 4189-4215. doi:10.1007/s11269-021-02940-1.

[14] Chitsazan, M., Eilbeigy, M., Mohammad Rezapour Tabari, M. Evaluation of Groundwater Nitrate Pollution Based on Main Components and Factor Analysis (Case Study: Karaj Plain Aquifer). Journal of Ecohydrology, 2018; 5: 1119-1133. doi:10.22059/ije.2018.256758.870.

[15] Tabari, M. M. R., Kabiri, S. M. Groundwater quality assessment using entropy weighted osculating value and set pair analysis methods (case study, SARAYAN plain). 2019; 21: 99-112.

[16] Tabari, M. M. R., Salehi, D. P. Groundwater Contaminantion Analysis Using Fuzzy-Topsis, Case Study: ZANJAN Plain. Journal of Environmental Science and Technology, 2020; 22: 101-116.

[17] Tabrizi, F., Movahed, E., Ojaqlou, H. Quality zonation of nitrate concentration for underground sources of drinking water in Lavasan City using Geographic Information System (GIS). Environmental Studies, Natural Resources and Sustainable Development Journal, 2020; 14: 45-52.

[18] Karim, M. R., Arham, M. A., Shorif, M. J. U., Ahsan, A., Al-Ansari, N. GIS based geostatistical modelling and trends analysis of groundwater quality for suitable uses in Dhaka division. Scientific Reports, 2024; 14: 17449. doi:10.1038/s41598-024-66567-z.

[19] Ali, S., Verma, S., Agarwal, M. B., Islam, R., Mehrotra, M., Deolia, R. K., Kumar, J., Singh, S., Mohammadi, A. A., Raj, D. Groundwater quality assessment using water quality index and principal component analysis in the Achnera block, Agra district, Uttar Pradesh, Northern India. Scientific Reports, 2024; 14: 5381. doi:10.1038/s41598-024-56056-8.

[20] Eftekhari, M., Eslaminezhad, S. A., Haji Elyasi, A., Akbari, M. Geostatistical Evaluation with Drinking Groundwater Quality Index (DGWQI) in Birjand Plain Aquifer. Environment and Water Engineering, 2021; 7: 267-278. doi:10.22034/jewe.2021.256731.1464.

[21] Azari, T., Tabari, M. M. R. An integrated approach based on HFE-D, GIS techniques, GQI SWI, and statistical analysis for the assessment of potential seawater intrusion: coastal multilayered aquifer of Ghaemshahr-Juybar (Mazandaran, Iran). Environmental Science and Pollution Research, 2024; 31: 13335-13371. doi:10.1007/s11356-024-31967-1.

[22] Stewart, O. T., Carlos, H. A., Lee, C., Berke, E. M., Hurvitz, P. M., Li, L., Moudon, A. V., Doescher, M. P. Secondary GIS built environment data for health research: Guidance for data development. Journal of transport & health, 2016; 3: 529-539. doi:10.1016/j.jth.2015.12.003.

[23] James, P., Jankowska, M., Marx, C., Hart, J. E., Berrigan, D., Kerr, J., Hurvitz, P. M., Hipp, J. A., Laden, F. "Spatial energetics": integrating data from GPS, accelerometry, and GIS to address obesity and inactivity. American journal of preventive medicine, 2016; 51: 792-800. doi:10.1016/j.amepre.2016.06.006.

[24] Mohammadyari, F., Aghdar, H., Basiri, R. Zoning groundwater quality for drinking using geo-statistical methods Case Study: Arid Regions in Mehran and Dehloran. "Sepehr" Quarterly Scientific-Research Journal of Geographic Information, 2017; 26: 199-208. doi:10.22131/sepehr.2017.25737.